Vector Meson Production in the Forward and Backward Region of the H1 Experiment at HERA

Diploma Thesis by
Peter Steinbach

submitted to
the Faculty of Physics and Earth Sciences
University of Leipzig

Referees: Prof. Dr. Tilman Butz (University of Leipzig)
Prof. Dr. Thomas Naumann (Deutsches Elektronen Synchrotron DESY, University of Leipzig)

Abstract

In this thesis, the Forward and Backward Silicon Detectors of the H1 experiment are used for the first time to identify a hadron from an invariant mass distribution of two decay particles. The purpose of this investigation is to observe elastic photoproduction of J/ψ particles in electron proton collisions with data taken by the H1 detector during 2006 and 2007. The main physics motivation is to extend the measurement of elastic J/ψ photoproduction to high and low total hadronic energies.
A study of the detector components necessary to identify the J/ψ mesons from their decays into two muons is performed. After the signal reconstruction from the invariant mass distribution, the cross section of the production mechanism is extracted and compared with previously published measurements and model predictions.

Kurzfassung

In dieser Arbeit werden die Vorwärts- und Rückwärts-Siliziumdetektoren des H1-Experimentes benutzt, um zum ersten Mal ein Hadron aus der invarianten Massenverteilung von zwei Zerfallsteilchen zu bestimmen. Das Ziel dieser Untersuchung ist die Beobachtung elastischer J/ψ Photoproduktion in Elektron-Proton-Streuprozessen mit Daten des H1-Experimentes der Jahre 2006 und 2007. Die zentrale physikalische Motivation ist die Erweiterung der Messung elastischer J/ψ Photoproduktion zu hohen und niedrigen Werten der hadronischen Gesamtenergie.
Es werden Studien der Detektorkomponenten vorgenommen, welche der Messung des J/ψ-Zerfalls in zwei Muonen dienen. Nach der anschließenden Signalrekonstruktion aus der invarianten Massenverteilung wird der Wirkungsquerschnitt bestimmt und mit publizierten Meßwerten und theoretischen Vorhersagen verglichen.

Contents

1. Preface **1**

2. Introduction **2**

3. Vector meson production **4**
3.1. Kinematics . . . 4
3.2. Diffractive J/ψ Production . . . 6
3.2.1. Diffraction . . . 6
3.2.2. The J/ψ vector meson . . . 6
3.3. Regge Theory . . . 7
3.3.1. The Optical Theorem . . . 7
3.3.2. Regge's ansatz . . . 9
3.3.3. Hadron-Hadron Scattering in Regge Theory . . . 12
3.3.4. Application to Photoproduction at HERA . . . 13
3.4. QCD based Models . . . 15
3.5. Monte Carlo Simulations . . . 19

4. The H1 Experiment at HERA **20**
4.1. The HERA Accelerator . . . 20
4.2. The H1 Experiment . . . 21
4.3. The Central Tracking Detectors . . . 25
4.3.1. The Central Jet Chambers (CJC) . . . 25
4.3.2. The Central Z-Chambers (COZ) . . . 27
4.3.3. The Central Proportional Chambers (CIP, COP) . . . 28
4.3.4. The Central Silicon Tracker (CST) . . . 28
4.3.5. The Liquid Argon Calorimeter (LAr) . . . 28
4.4. The Central Muon Detectors . . . 29
4.4.1. The Central Muon Detector (CMD) . . . 29
4.4.2. The Forward Muon Detector (FMD) . . . 30
4.4.3. The Central Muon Identification . . . 31
4.5. The Backward and Forward Silicon Tracker . . . 36
4.5.1. Silicon Detectors . . . 36
4.5.2. The Forward Silicon Tracker (FST) . . . 37
4.5.3. The Backward Silicon Tracker (BST) . . . 38
4.6. The electromagnetic Spaghetti Calorimeter (SpaCal) . . . 39
4.7. The H1 Trigger Scheme . . . 41
4.8. Track Reconstruction and Data Taking . . . 42

5. Event Selection and Cuts **45**
5.1. Run Selection and Trigger . . . 45
5.2. Event classification . . . 45
5.3. Track Cuts . . . 47
5.4. Decay Muon Identification . . . 49
5.4.1. Central Muon ID . . . 49
5.4.2. Forward Muon ID . . . 49
5.4.3. Backward Muon ID . . . 49
5.5. Background Treatment . . . 51
5.5.1. Resonant Background . . . 51
5.5.2. Non-Resonant Background . . . 51
5.6. Event Reconstruction . . . 52
5.7. J/ψ Event Cuts . . . 54

6. Acceptances, Resolutions and Efficiencies **57**
6.1. Detector resolutions with MC . . . 57
6.2. Geometric Acceptances and Reconstruction efficiency . . . 60
6.3. Muon matching precision . . . 63
6.4. Muon ID efficiency . . . 66
6.5. J/ψ reconstruction . . . 68
6.6. Trigger efficiency . . . 72

7. Signal and Cross Section Determination **77**
7.1. Cross Section Determination . . . 77
7.1.1. The Cross Section . . . 77
7.1.2. Photon Flux Determination . . . 77
7.2. Signal Extraction . . . 79
7.2.1. The J/ψ Signal from H1 Data in 2006 and 2007 . . . 79
7.2.2. Correction Factors . . . 81
7.3. Statistical and Systematic Uncertainties . . . 82
7.4. Results . . . 84

8. Summary **92**

A. Appendix - Mass Distribution Fits **94**

Acknowledgements **109**

Statement of authorship **110**

1. Preface

Early in the history of science, mankind began to reflect on the origin and nature of matter. "What are we made of?" is and has been the central question.
More than 2000 years ago, a Greek philosopher, Democritus of Abdera, and his teacher, Leucippus, concluded that the world as presented to our senses was made from indivisible particles constructing all elements, matter and soul hovering in void space. They called these particles atoms, from Greek *'atomos'* for 'indivisible', which in Latin transcription means 'individuum'. This concept offered a scientific explanation for the survival of our soul long after a personality had ceased its physical existence and hence gave way to an 'atomist' apprehension of morality: "atoms" kept their flavor from good or bad deeds done in the course of one's life. Confronted with the observation that their ill flavored soul particles would be handed down to their offspring by atomic conservation, this was meant to motivate people to live a morally integral life.

2. Introduction

Since 1991, the HERA electron[1] proton collider at DESY Hamburg and its four experiments, H1, Hera-B, Hermes and Zeus, offered a unique opportunity to probe and improve our understanding of the interactions in lepton nucleon scattering processes and to resolve the structure of the proton, i.e. of matter itself.

The scattering reactions belong to very different processes. One type was recorded that showed many characteristics of optical diffraction and is therefore referred to as diffraction. Before HERA was commissioned, this process was also observed in hadron-hadron collisions and subsequently described by Regge theory - a phenomenological ansatz. Diffractive interactions at fixed target experiments with an incoming real or virtual photon produce vector mesons carrying the same quantum numbers as the photon. The observed phenomenology relates to hadron-hadron interactions via the Vector-Meson-Dominance-Model which attributes hadronic properties to the interacting photon.
However, at energies compared to those available at HERA, these models show some discrepancies in the description of heavy vector mesons. Recent models describe such diffractive reactions in the framework of Quantum Chromodynamics (QCD), where - in the simplest case - the process is modeled by an exchange of two gluons, the exchange bosons of QCD. Due to the kinematic setting of diffractive processes perturbative calculations are not always applicable.

This study will analyze the diffractive production of J/ψ mesons using H1 data collected in the years 2006 and 2007. The focus is on photoproduction where quasi-real photons at low virtualities are emitted from the electron to interact with the proton. The produced J/ψ is reconstructed from its leptonic decay into two muons which shows a clean experimental signature in the detector, whereas the electron and the proton continue through the beam pipe outside the H1 acceptance. Deep inelastic scattering (DIS) reactions, where a deeply virtual photon interacts with the substructure of the proton, will not be subject of this investigation. The main physics motivation is to extend the measurement of elastic J/ψ photoproduction to high and low total hadronic energies. In parallel, this investigation will concentrate on reducing systematic errors caused by the identification of the decay muons.

This thesis starts with an overview on phenomenological descriptions of diffractive J/ψ production processes. The event kinematics and its parameters are described first, followed by an introduction to different theoretical models concerning the kinematic range studied.
Chapter three describes the basic detector design of the H1 Experiment and the HERA collider. There will be a description of all H1 components used for this analysis as well as a brief report on the data taking at H1.

[1] HERA has run with electrons and positrons in the chosen data set. However the beam lepton will be referred to as the 'electron' throughout this study.

After that, chapter four progresses to note the used data sample and discuss the chosen cuts on tracks and events. Along this, lepton decay identification strategies as well as used background suppression methods are illustrated.
An important part of this study is the determination of detector efficiencies and resolutions concerning reconstruction, lepton identification or matching precisions, event triggering capabilites and description in MC simulation. This will be covered by chapter five.
Chapter six gives the details of signal extraction as well as cross-section determination. The main results of this investigation are presented here.
Finally, chapter seven concludes with a summary on the results of this study and an outlook on further investigations.

3. Vector meson production

In this chapter, an overview of the theory and phenomenology of diffractive J/ψ production in collisions is given. After introducing the variables relevant to this analysis, the diffractive J/ψ production process is described. At the end of the chapter, a description of the Monte Carlo event generators used to model the theoretical predictions is given.

3.1. Kinematics

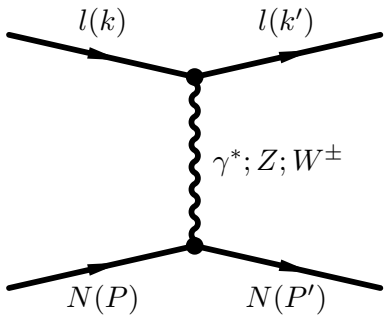

Figure 3.1.: Feynman diagrams for neutral (γ^*; Z) and charged current ($W^\pm$) lepton nucleon scattering.

Electron proton scattering processes can be subdivided into two main categories:

(NC)	e + p $\rightarrow$ e + hadrons
(CC)	e + p $\rightarrow$ ν_e + hadrons

The neutral current (NC) process is mediated by the exchange of a virtual photon γ^* or a Z^0 gauge boson, both carrying zero electrical charge. The charged current (CC) process is mediated by the exchange of a $W^\pm$ gauge boson, depending on the charge of the incoming lepton beam. Figure 3.1 shows the first order Feynman diagrams for both processes.
In the kinematic region relevant for the present analysis an exchange of a Z^0 or $W^\pm$ is suppressed due to the high mass of the latter. Therefore, only neutral current electron proton processes via the exchange of a zero mass photon are discussed.

As one important parameter of the reaction, the center-of-mass energy squared s of the collision results directly from the four-momentum of the incoming electron $\mathbf{k} = (E_e, \vec{k})$[1]

[1]Throughout this study, all parameters and constants will be given in natural units common in high energy physics, i.e. $c = \hbar = 1$.

with mass m_e and the incoming proton $\mathbf{P} = (E_p, \vec{p})$ with mass m_p in the ultra-relativistic case as indicated

$$s = (\mathbf{k} + \mathbf{P})^2 \overset{m_e = m_p = 0}{=} 4E_e E_p. \tag{3.1}$$

E_e and E_p hereby refer to the beam energies and $\vec{k}$ as well as $\vec{p}$ to the three-momenta of the incoming electron and proton respectively, giving $\sqrt{s} = 318$ GeV for HERA. As indicated above, the approximation neglects the masses $m_e = 511$ keV and $m_p = 938$ MeV.
The four-momentum transferred by the virtual photon at the electron vertex Q^2 is defined as

$$Q^2 := -\mathbf{q}^2 = -(\mathbf{k} - \mathbf{k}')^2 \tag{3.2}$$

Figure 3.1 shows how $\mathbf{k}'$ denotes the four-momentum of the scattered electron and $\mathbf{q}$ the four-momentum of the exchanged virtual photon. Q^2 is therefore often referred to as *photon virtuality*. Note that Q as such is always complex. It can also be described by the Björken scaling variable x and the inelasticity y:

$$x = \frac{-\mathbf{q}^2}{2\,\mathbf{q} \cdot \mathbf{P}} \tag{3.3}$$

$$y = \frac{\mathbf{q} \cdot \mathbf{P}}{\mathbf{k} \cdot \mathbf{P}} \tag{3.4}$$

$$Q^2 = xys \tag{3.5}$$

In the Quark Parton Model ([1]), the Björken scaling variable x is the momentum fraction of the struck parton in the proton participating in the scattering. The variable y describes the fraction of the scattered electron energy which is transferred to the proton in its rest frame. Both parameters are limited to values between 0 and 1.

At HERA, two kinematic regions in Q^2 can be defined. Considering the limit $Q^2 \to 0$, the exchanged photon is observed as quasi-real. As already mentioned, this limit is called photoproduction which is the focus of this investigation. For larger $Q^2 > 1$ GeV^2, virtual photons γ^* are radiated off the lepton. This regime is called Deep Inelastic Scattering (DIS). Experimentally, the limit between the two kinematic regions is $Q^2 \approx 1 - 2$ GeV^2 because the scattered electron can only be detected in the main detector for values of $Q^2 \gtrsim 1$ GeV^2 corresponding to an electron scattering angle $\theta_{e'} > 175$ °. The $\gamma^* p$ hadronic system can be characterized by its center-of-mass energy $W_{\gamma p}$ by

$$W_{\gamma p}^2 = (\mathbf{q} + \mathbf{P})^2 = Q^2 \cdot \frac{1 - x}{x} + m_p^2. \tag{3.6}$$

$W_{\gamma p}$ can also be derived directly:

$$\begin{aligned} W^2 &= (\mathbf{q} + \mathbf{P})^2 \\ &= m_p^2 - Q^2 + 2\mathbf{q} \cdot \mathbf{P} \\ &= m_p^2 - Q^2 + y(s - m_p^2) \\ &= ys - Q^2 + m_p^2(1 - y). \end{aligned}$$

For $m_p^2 \ll W^2$ this gives

$$W_{\gamma p}^2 = ys - Q^2. \tag{3.7}$$

3.2. Diffractive J/ψ Production

3.2.1. Diffraction

The neutral current process $e + p \rightarrow e + X$, where X denotes any hadronic final state, can be divided further - there are inelastic and diffractive processes.

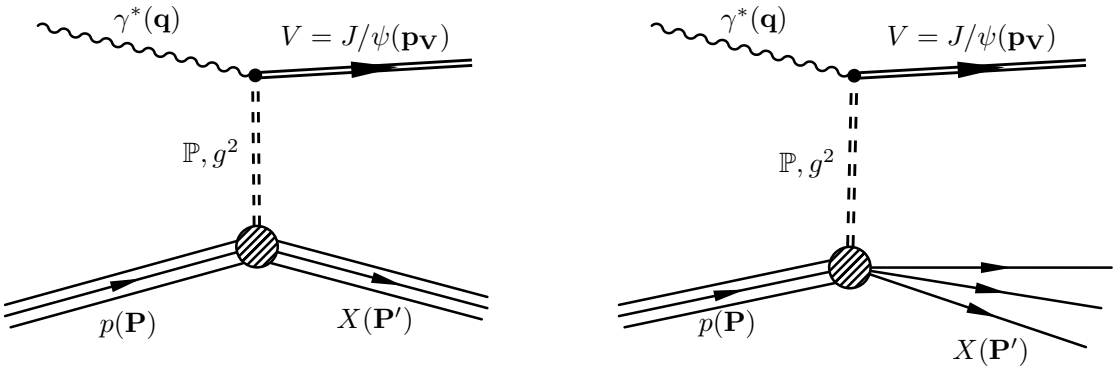

Figure 3.2.: Diagram of diffractive *ep*-scattering: elastic scattering (left) and proton dissociative diffraction (right). The production mechanism is illustrated for the Regge ($\mathbb{P}$) and the QCD (g^2) description as a double dashed line producing a vector meson V.

Figure 3.2 shows the generic graphs of scattering, where only a) is the subject of this analysis and b) represents a background interaction. Diffractive events show a characteristic *rapidity gap* between the final states from the photon and the proton, respectively. Examples of diffractive final states at HERA are vector mesons of different flavors and jets originating from quark fragmentation. In diffractive processes, the incoming proton may remain intact (*elastic* scattering) and is scattered at a small angle, or the proton dissociates develops into an excited state of low mass with the same quantum numbers as the proton (*proton dissociative* scattering). To distinguish between the two, the Lorentz-invariant four-momentum transfer at the proton vertex t can be used. It is defined by

$$t := (\mathbf{P} - \mathbf{P'})^2 = (q - p_V)^2 \tag{3.8}$$

$$\approx -(p_{t,V})^2 \qquad \text{for } q^2 \approx 0 \tag{3.9}$$

where $\mathbf{P'}$ denotes the four-momentum of the scattered proton and $p_{(t)V}$ the (transverse) momentum of the produced vector meson.

3.2.2. The J/ψ vector meson

The J/ψ was discovered in 1974 by Burton Richter ([2], SLAC) and Sam Ting ([3], FNAL) simultaneously, see also [4]. Since both scientists could not agree on a name, the particle inherited the unusual two-compound name.

Its constituents are a charm and anti-charm quark, which is a combination often referred to as *Charmonium*. The invariant mass measures to $m_{J/\psi} = 3096.912 \pm 0.011$ MeV [5]. Its total angular momentum J, the parity eigenvalue P and the charge conjugation eigenvalue C are $J^{PC} = 1^{--}$. It is a vector meson with exactly the quantum numbers of the photon. The J/ψ decays predominantly into hadrons and leptonically into e^+e^- or $\mu^+\mu^-$. The latter decay mode is used in this analysis for its clean experimental signature for detection in H1. Different J/ψ properties as well as the branching ratios are listed in table 3.1.

mass m	3096.916 ± 0.011 MeV
Full Width Γ	93.4 ± 2.1 keV
Dominant decay channels	
Hadronic	(87.7 ± 0.5) %
e^+e^-	(5.94 ± 0.06) %
$\mu^+\mu^-$	(5.93 ± 0.06) %

Table 3.1.: Parameters of the J/ψ Vector Meson, as in [5]

Elastic J/ψ photoproduction can be described by two approaches. There is the effective ansatz by Regge theory, where the scattering between the J/ψ and the proton is described via the exchange of Regge trajectories. More recent models interprete this process based on perturbative QCD as an exchange of (at least) two gluons. The key ideas and motivations of these competing interpretations shall be outlined in the next section.

3.3. Regge Theory

Regge theory is described in hadron-hadron interactions and key ideas of the theoretical motivation are briefly noted. The theoretical ansatz is then applied to photoproduction at HERA. The complete model of Regge theory and Pomeron physics is described in full detail in [6].

3.3.1. The Optical Theorem

For the general two-body scattering process $ab \to cd$ as in fig. 3.3, the Mandelstam variables can be defined as

$$s := (p_a + p_b)^2 \tag{3.10}$$

$$t := (p_a - p_c)^2 = (p_b - p_d)^2 \tag{3.11}$$

$$u := (p_a - p_d)^2 \tag{3.12}$$

$$s + u + t = m_a^2 + m_b^2 + m_c^2 + m_d^2 \tag{3.13}$$

where p_i and m_i on $i \in (a, b, c, d)$ are the four-momenta and masses of the interacting particles. As already introduced in section 3.1, s is the square of the center-of-mass energy and t notes the square of the four-momentum transfer from one initial to one final state particle. Because of equ. 3.13, only two of three Mandelstam variables - s,t or u - are independent. Usually, s and t are taken.

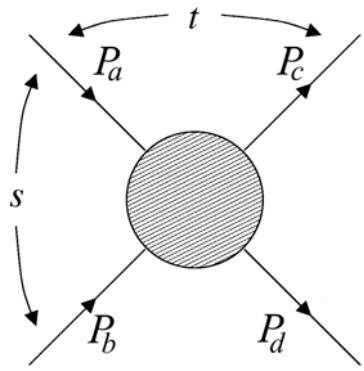

Figure 3.3.: $ab \to cd$ scattering process

By *crossing* and the assumption of CPT invariance against charge conjugation C, parity inversion P and time reversal T (CPT).[2], the scattering process $ab \to cd$ can be affiliated to the process $b\bar{d} \to \bar{a}c$. Here, the squared center-of-mass energy is given by $t = (p_b - p_d)^2$. The processes where s or t give the square of the relevant reaction energy are called s-channel or t-channel processes respectively. Both types occupy varying regions in s and t. In the case of equal mass scattering, where $m_0 = m_i|_{i=(a,b,c,d)}$, the physical region for the s-channel as in shown in [1] is given by

$$s \geq (m_1 + m_2)^2 = 4m_0^2, \quad t \leq 0, \quad u \leq 0. \tag{3.14}$$

We now have to recall the fundamentals of scattering theory.
In a system of orthonormal quantum mechanical states, the transition probability P_{fi} for a process with $|f\rangle$ as final state and $|i\rangle$ as initial state is connected to the scattering matrix S by

$$P_{fi} = |\langle f|S|i\rangle|^2 \tag{3.15}$$

Further, the S matrix elements are connected to the transition matrix T when advancing to a continuum of states. When limiting the ansatz to a two-body initial state, the matrix elements of T are

$$\langle f|S|i\rangle = \langle P'_a P'_b \dots P'_n|S|P_a P_b\rangle = \delta_{fi} + i(2\pi)^4 \delta^4(P^f - P^i)\langle f|T|i\rangle \tag{3.16}$$

where P^i is the sum over all initial states and P^f over all final state four-momenta. $|f\rangle = |P'_a P'_b \dots P'_n\rangle$ gives an arbitrary final state wave function. The total cross section for the reaction $ab \to n$, where n describes a particle final state as above, is

$$\sigma_{ab\to n} = \frac{1}{4|\mathbf{p}_a|\sqrt{s}} \Sigma_n (2\pi)^4 \delta^4(P^f - P^i)|\langle f_n|T|i\rangle|^2 \tag{3.17}$$

Here, p_a is the initial momentum in the s-channel center-of mass frame. Without further derivation, it is given by

$$|\mathbf{p}_a|^2 s = (p_a \cdot p_b)^2 - m_a^2 m_b^2 = \frac{1}{4}[s - (m_a + m_b)^2][s - (m_a - m_b)^2] \tag{3.18}$$

[2]Implying that anti-particles have the same mass as their CPT partners, but opposite charge and moving backward in time.

This then gives the Lorentz invariant cross section, over which momentum integrations may be performed in any frame.
By means of unitarity in S, $SS^\dagger = 1$, and the completeness of the set of orthonormal states besides the final and initial one in eqn. 3.16,

$$\langle j|T|i\rangle - \langle f|T^\dagger|i\rangle = (2\pi)^4 i\Sigma_f \delta^4(P^f - P^i)\langle j|T^\dagger|f\rangle\langle f|T|i\rangle \tag{3.19}$$

Setting $j = i$ here, this goes to

$$2\,\mathrm{Im}\langle i|T|i\rangle = \Sigma_f (2\pi)^4 \delta^4(P^f - P^i)|\langle f|T|i\rangle|^2 \tag{3.20}$$

When summed over f, the right hand side of the above gives the total transition rate and thus leads to the total cross section when summed over all final-state particles n:

$$\sigma_{ab}^{Tot} = \frac{1}{4|\mathbf{p}_a|\sqrt{s}}\mathrm{Im}\langle i|T|i\rangle = \frac{1}{4|\mathbf{p}_a|\sqrt{s}}A(s, t = 0) \tag{3.21}$$

Where $A(s, t = 0)$ is the elastic scattering amplitude for the reaction $ab \to ab$. Equation 3.21 is commonly known as the Optical Theorem.

3.3.2. Regge's ansatz

Taking this knowledge to an arbitrary scattering process $a + b \to c + d$, the s-channel process corresponds to the physical limit $t, u < 0$. Thus the analytical function $A_{a+b\to c+d}(s, t, u)$ can be continued to t- or u-channel regions, giving the connections of the amplitudes by a crossing symmetry

$$A_{a+b\to c+d}(s, t, u) = A_{a+\bar{c}\to\bar{b}+d}(t, s, u) = A_{a+\bar{d}\to\bar{b}+c}(u, t, s) \tag{3.22}$$

In addition, at fixed s the momentum transfer t varies linearly with the variable $z_s = \cos\theta_s$, where θ_s describes the s-channel scattering angle in the center-of-mass frame. So, z_S and s can be used as independent variables. Now $t = t(s, z_s)$ and $u = u(s, z_s)$, $A(s, t)$ can be expanded into partial waves

$$A(s, t(s, z_s)) = 16\pi\ \Sigma_{l=0}^{\infty}(2l + 1)A_l(s)P_l(z_s) \qquad \text{with } l \in \mathbb{N} \tag{3.23}$$

where $P_l(z_s)$ are the Legendre Polynomials of the 1st kind, of orders in l. In analogy to the s-channel exchange, the equivalent amplitude can be expressed in a partial-wave series for the t-channel scattering as

$$A(s, t) = 16\pi\Sigma_{l=0}^{\infty}(2l + 1)A_l(t)P_l(z_t) \tag{3.24}$$

where

$$z_t = \cos\theta_t = 1 + \frac{2s}{t - 4m^2} \qquad \text{and } l \in \mathbb{N} \tag{3.25}$$

for the equal-mass case. This series goes as $z_l \to s$ for $s \to \infty$ to give $P_l(z) \propto z^l$ which diverges with rising z. To resolve this contradiction, the series over l is continued to an integral over l. Even this sophisticated form describes the data only up to a threshold of 2 GeV. The model of one exchanged particle in the t-channel contradicts observation as

in fig. 3.4 and thus has to be abandoned. All the resonance contributions in t must act collectively to give the observed energy dependence.

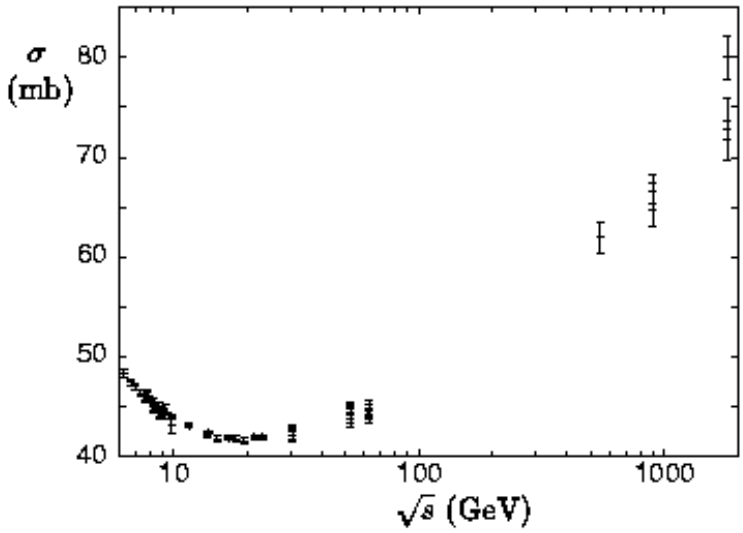

Figure 3.4.: $\bar{p}p$ total cross sections as in [6].

The mathematical framework for adding the resonances is based on a formalism by Regge ([7],[8],[9]), initially developed for non-realivistic potential scattering. Arguing that the angular momentum l, having by definition only non-negative integer values, can be continued into a continuous complex variable, he showed the Schrödinger equation to be solvable with a spherically-symmetric potential for complex l. Hence, the partial wave amplitude $A_l(t)$ can be considered as functions $A(l,t)$ of complex l. He discovered, that if the potential is a superposition of Yukawa potentials, the singularities of $A(l,t)$ in the complex l-plane are poles whose locations vary with t according to functions $\alpha(t)$ called Regge trajectories

$$l = \alpha(t). \tag{3.26}$$

These poles are known as Regge poles, or reggeons, and as t varies they trace out paths defined by equ. 3.26 in the complex l-plane. In relativistic scattering theory, they are identified with the exchanges of families of particles as illustrated in fig. 3.5. Note, that values of l such that $\alpha(t)$ is a non-negative integer correspond to the squared mass of a bound state or resonance having spin l.

Introducing this into equ. 3.24 and taking the sum into a path integral over a curve in the complex l-plane by means of the Sommerfeld-Watson transform [6], one receives in leading order approximation

$$A^{\pm}(s,t) \propto \Sigma_i \beta_i^{\pm}(t)\Gamma(-\alpha_i^{\pm}(t))(1 \pm e^{-i\pi\alpha_i^{\pm}(t)})(\frac{s}{s_0})^{\alpha_i^{\pm}(t)} \tag{3.27}$$

which gives the large s and small t relativistic limit of equation 3.24, ignoring the background integrals that need to be added afterwards. Here $A^{\pm}(s,t)$ gives the amplitude for

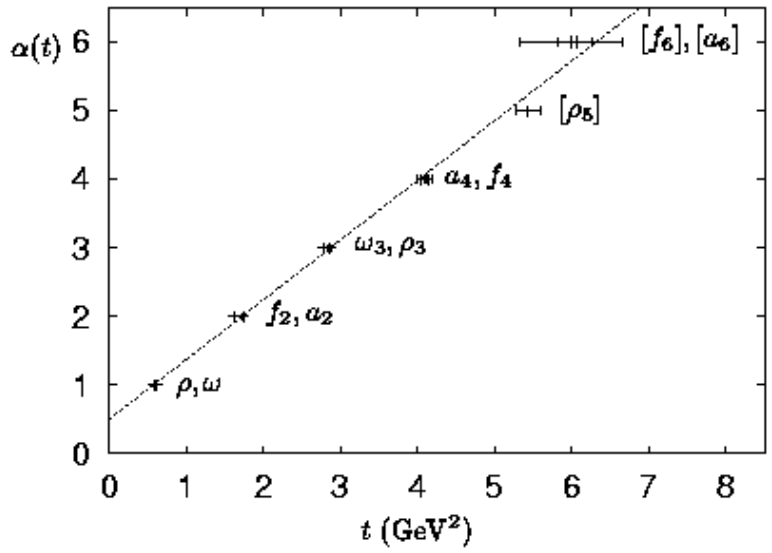

Figure 3.5.: Chew-Frautschi plot: The total angular spin $l = \alpha(t)$ plotted against the particle mass squared $t = m^2$ as in [6]. Each point corresponds to a particle family that interacts when a reggeon trajectory is exchanged. The fit follows $\alpha(t) = 0.44 + 0.93\,t$.

odd and even integer values of l. Meanwhile, the subdivision $A(s,t) = A^+(s,t) + A^-(s,t)$ is caused by the relativistic transcription of the Regge formalism.
Variables $\alpha_i^\pm(t)$ describe the poles in the l-plane and $\beta_i^\pm(t)$ note their residues, as Γ resembles the well-known Γ-function. Most important, the factor $(s/s_0)^{\alpha_i^\pm(t)}$ arises from the $s \to +\infty$ behavior of the Legendre Polynomials as defined above. On the introduction of s_0, the authors of [6] quote:

> "It is inelegant to raise to a power a quantity such as s that has dimensions of squared mass, so often we introduce a fixed scale s_0, with dimensions of squared mass, ..."

The $\Gamma(-\alpha_i^\pm(t))$ factors have poles for values of t such that $\alpha_i^\pm(t)$ takes a non-negative integer values $\sigma^\pm$. Now, one identifies these poles with the exchange of particles of spin $\sigma^\pm$, whose squared mass is the corresponding value of t. Assuming that $A^+(s,t)$ shows a pole in the complex l-plane, it would coincide with the t-channel partial wave amplitude $A_l(t)$ when $l = \sigma$ and a non-negative integer. This implies that for values t_0 close to t such that Re $\alpha(t) = \sigma$, one receives

$$A_\sigma(l) = \frac{G(t)}{\sigma - \alpha(t)}. \tag{3.28}$$

This includes the arbitrary coupling constant $G(t)$. Plugging in a Taylor expansion up to 1st order of Re $\alpha(t) = \sigma + \alpha'(t - t_0) + \ldots$ about t_0, one receives

$$A_\sigma(l) \approx -\frac{G(t)/\alpha'}{t - t_0 + i\text{Im }\alpha(t_0)/\alpha'}. \tag{3.29}$$

which finally gives the Breit-Wigner form for a resonance of mass m_R such that $m_R^2 = t_0$, requiring Im $\alpha(m_R^2) > 0$, whereas Im $\alpha(m_R^2) = 0$ gives equ. 3.29 the form of a bound state.

The linear ansatz for $\alpha(t)$ is often referred to as

$$\alpha(t) = \underbrace{1+\epsilon}_{=\alpha_0} + \alpha' t, \tag{3.30}$$

where α_0 is the intercept and α' the *slope* of the trajectory. Thus, $\epsilon = \alpha_0 - 1$ is a conventional abbreviation. The s-channel process can be described when extrapolating the trajectory to $t < 0$. The scattering amplitude is calculated by integration over all poles of the trajectory. For simplicity, the partial wave expansion is approximated by the scattering amplitude of just one Regge trajectory

$$A(s,t) \approx \beta(t) e^{\alpha(t)} \tag{3.31}$$

in the kinematic region where $t < 0$ and $s \to \infty$. The differential cross section of one trajectory then computes to

$$\frac{d\sigma}{dt} = \frac{1}{16\pi s^2} |A(s,t)|^2 \propto s^{2(\alpha(t)-1)} \tag{3.32}$$

3.3.3. Hadron-Hadron Scattering in Regge Theory

In hadron-hadron interactions, the total cross section σ_{tot}^{AB} for the scattering of two hadrons A and B can be given by the sum of Regge trajectories

$$\sigma_{tot}^{AB}(s) = \sum_i \beta_{Ai}(0)\beta_{Bi}(0)\left(\frac{s}{s_0}\right)^{\alpha_i(0)-1} \tag{3.33}$$

where β is interpreted as a form factor describing the coupling of a trajectory i to the hadron A or B and s_0 is a hadronic scale as introduced in equ. 3.27. Further, $\alpha_i(t)$ are Regge trajectories as in equ. 3.29.

Here, two trajectories contribute to the total cross section.

$$\sigma_{tot}^{AB}(s) = \beta_{A\mathbb{P}}(0)\beta_{B\mathbb{P}}(0)\left(\frac{s}{s_0}\right)^{\epsilon} + \beta_{A\mathbb{R}}(0)\beta_{B\mathbb{R}}(0)\left(\frac{s}{s_0}\right)^{-\eta} \tag{3.34}$$

where $\epsilon = 1 - \alpha_{\mathbb{P}}(0)$ and $\eta = 1 - \alpha_{\mathbb{R}}(0)$. The contribution $\mathbb{R}$ delivered by the Reggeon trajectory $\alpha_{\mathbb{R}}$ adds mostly at low energies. At higher energies, the *Pomeron* trajectory $\alpha_{\mathbb{P}}$ dominates. A Reggeon trajectory can be related to observed particles (i.e. ρ, ω, f_2, a_2), while there are no observed particles which correspond to the Pomeron trajectory. A fit to experimental hadron-hadron data [7],[10] led to values in $\epsilon = 0.0808$ and $\eta = 0.4525$. It is thus the contribution of the Pomeron trajectory that leads to an increase of the hadron-hadron cross section with rising s. This trajectory is often referred to as the *soft Pomeron* trajectory.

Since the proton consists of different quarks than the charm quarks in the J/ψ meson (OZI rule [11],[12]), only the Pomeron trajectory contributes to the diffractive J/ψ production. Thus, $\alpha_{\mathbb{P}}(0)$ is called the *Pomeron intercept* and $\alpha'_{\mathbb{P}}$ the Pomeron slope. As described in section 3.3.1, the slope parameter $\alpha'_{\mathbb{P}}$ is universal in Regge theory. At high s and low t, the elastic differential cross section can be written as

$$\frac{d\sigma_{el}^{AB}(s)}{dt} = \frac{1}{16\pi}\beta_{A\mathbb{P}}(t)^2\beta_{B\mathbb{P}}(t)^2\left(\frac{s}{s_0}\right)^{2\alpha_{\mathbb{P}}(t)-2} \tag{3.35}$$

This exactly mirrors the implications from equ. 3.32. With an exponential ansatz for the form factors $\beta_{i\mathbb{P}}(t)$

$$\beta_{i\mathbb{P}}(t) = \beta_{i\mathbb{P}}(0) \cdot e^{b_i t} \tag{3.36}$$

one obtains

$$\frac{d\sigma_{el}^{AB}(s)}{dt} = \frac{1}{16\pi}\beta_{A\mathbb{P}}(0)^2\beta_{B\mathbb{P}}(0)^2 e^{b_{el}t}(\frac{s}{s_0})^{2\alpha_{\mathbb{P}}(0)-2} \tag{3.37}$$

with

$$b_{el}(s) = 2\,b_A^0 + 2\,b_B^0 + 2\,\alpha'_{\mathbb{P}}\,ln\frac{s}{s_0} \tag{3.38}$$

where b_A^0 and b_B^0 are energy independent terms originating from the form factors. When integrating equ. 3.37 over t leads to the total elastic cross section

$$\sigma_{el}^{AB}(s) = \frac{1}{16\pi}\beta_{A\mathbb{P}}(0)^2\beta_{B\mathbb{P}}(0)^2\frac{s^{2\epsilon}}{b_{el}(s)} \propto \frac{s^{2\epsilon}}{b_{el}(s)} \tag{3.39}$$

A fit to experimental proton-proton scattering results gave $b_p^0 \approx 2-3$ GeV^{-2}. An increase of $b(s)$ with rising s has been observed. This effect is called *shrinkage*.
In a geometrical interpretation, the slope parameter $b(s)$ ([13, 14, 15]) is related to the mean-square of the interaction radius $r^2 = 2\,b(s)$. At proton-proton experiments $b(s)$ varies between $b \approx 8$ GeV^{-2} at small energies (corresponding to the proton radius of $r \approx 4$ GeV^{-1}) and $b \approx 12$ GeV^{-2} at $s \approx 5000$ GeV^2. In this geometrical view, the scattering constituents are regarded as discs transversely oriented to the direction of flight of the beams. According to equ. 3.38, the radius of the interaction region consists of two parts: two energy independent terms related to the projectiles A and B and a term with $\alpha'_{\mathbb{P}}$ and an energy dependence increasing logarithmically with s – the soft Pomeron. A review of data from hadron-hadron scattering experiments [11],[12] yields a value of $\alpha'_{\mathbb{P}} \approx 0.25$ GeV^{-2}.

3.3.4. Application to Photoproduction at HERA

Combined with the Vector Meson Dominance model (VMD), Regge theory can be applied to diffractive photon-proton scattering processes (see Fig. 3.2). The VMD Model describes the photon as a superposition of an electromagnetic wave function $|\gamma_{QED}\rangle$ and a hadronic one $|\gamma_{had}\rangle$

$$|\gamma\rangle = N_1|\gamma_{QED}\rangle + N_2|\gamma_{had}\rangle \tag{3.40}$$

Thus, the hadronic state is required to have the same quantum numbers as the photon. This is the case for the neutral vector mesons ρ, ω, Φ, J/ψ, Υ and their radial excitations. Therefore, equ. 3.40 can be written as

$$|\gamma\rangle = N_1|\gamma_{QED}\rangle + \sum_V \frac{e}{f_V}|V\rangle \tag{3.41}$$

where f_V corresponds to the coupling of the vector meson V to the photon and denotes the probability that the photon fluctuates into a virtual vector meson V^*. The total cross section for photoproduction of a vector meson V then is:

$$\sigma(\gamma^* p \to Vp) = \frac{4\pi\alpha_{QED}}{f_V^2}\sigma(Vp \to V^* p) \tag{3.42}$$

This approximation neglects processes as $\gamma^* p \to V^* p \to V' p$, where V' denotes a different type of vector meson as V. The center of mass energy for the latter process $V^* p \to V' p$ is $W_{\gamma p}$. Replacing s with $W_{\gamma p}$ in equ. 3.37 and 3.39, one obtains

$$\frac{d\sigma_{\gamma p}}{dt} = \frac{d\sigma_{\gamma p}}{dt}|_{t=0,W=W_0} \cdot e^{b(W)t}(\frac{W}{W_0})^{4(\alpha_{\mathbb{P}}(0)-1)} \propto e^{b(W)t} W_{\gamma p}^{4\epsilon} \tag{3.43}$$

$$\sigma_{el}^{AB}(s) = \propto \frac{W_{\gamma p}^{4\epsilon}}{b_{el}(W_{\gamma p})} \tag{3.44}$$

$$b(W) = b_0 + 4\alpha'_{\mathbb{P}} ln \frac{W_{\gamma p}}{W_{\gamma p,0}} \tag{3.45}$$

where W_0 denotes a normalization parameter. At low t, the W dependence approximates to

$$\sigma_{\gamma p} \propto (\frac{W}{W_0})^{\delta} \tag{3.46}$$

The ep cross section is to first order related to the γp cross section via

$$\sigma(\gamma p \to J/\psi Y) = \frac{\sigma(ep \to eJ/\psi Y)}{\Phi_\gamma} \tag{3.47}$$

where Φ_γ is the photon flux integrated over Q^2 and y (for more see section 7.1.2). This approximation is valid, since the photon flux decreases rapidly with Q^2 and y. In addition, the helicity of the virtual vector meson and the photon are assumed to be equal and conserved during the interaction with the proton.

Figure 3.6 depicts the elastic cross sections for the production of the vector mesons ρ, ω, Φ, J/ψ, Υ and Υ' together with the total photoproduction cross section measured at HERA as a function of $W_{\gamma p}$ [16, 17, 18, 19, 20, 21, 22].Elastic cross sections of light vector mesons show a slow rise which can be described by a polynomial fit in W^{δ}, see equ. 3.46, with $\delta = 0.22$. The photoproduction cross section of the heavier J/ψ meson on the other hand gives a value of $\delta = 0.7$. The measurement of this energy dependence at high and low values of $W_{\gamma p}$ is the main physics aim of the present thesis.

In order to describe the steeper rise with energy, new models have been developed. In [23] an additional hard Pomeron is proposed with a trajectory $\alpha_{\mathbb{P}_h}$

$$\alpha_{\mathbb{P}_h}(t) \approx 1.4 + 0.1 \cdot t \tag{3.48}$$

.

The combination of a soft and hard Pomeron is able to describe J/ψ photoproduction qualitatively [17]. The calculations in [24] are based on a dipole Pomeron model assuming a trajectory with a non-linear t-dependence.

For the proton dissociative process at fixed masses M_Y of the hadronic final state, the same W dependence as for the elastic process is predicted, while the t-dependence is different. The cross section for the diffractive process $AB \to YB$, where hadron A dissociates into the system Y is given by ([15],[25],[26])

$$\frac{d^2\sigma_{pd}^{AB}(s)}{dtdM_Y^2} \propto \frac{\beta_A(0)\beta_B(t)^2}{s^2} s^{2\epsilon} (\frac{s}{M_Y^2})^{2\alpha_{\mathbb{P}}(t)} (M_Y^2)^{2\alpha_{\mathbb{P}}(0)} = x\beta_A(0)\beta_B(0)^2 s^{2\epsilon} \frac{e^{b_{pd}t}}{M_Y^{2(1+\epsilon)}} \tag{3.49}$$

ϵ is defined in equ. 3.34 and b_{pd} is the slope parameter

$$b_{pd} = b_{0;B} + 2\alpha'_{\mathbb{P}} ln(\frac{s}{M_Y^2}) \tag{3.50}$$

Measurements at HERA [16] yield b_{pd} to be of the order of 1 GeV^{-2}, while the W dependence of the cross section remains equivalent to elastic process.

3.4. QCD based Models

Quantum Chromodynamics (QCD), the theory of the strong interaction, proved to be a valid description of many experimental results. It models the interactions between quarks and gluons in a comparable way as quantum electrodynamics (QED) does for interactions between electrons and photons.
Due to the varying coupling constant $\alpha_S(Q^2)$ in QCD, perturbative calculations can only be applied at distances smaller than the proton radius. At larger scales, the perturbative expansion breaks down due to the large running coupling of $\alpha_S(Q^2)$ making this approach obsolete. However, scattering processes are subject to effects on large and small distance scales which compares to small and large momentum scales.

HERA data can not only test QCD at small distances, but also extend into the transition region towards interactions where perturbative calculations is not applicable. As already noted, electron proton collisions can be treated as photon-proton scattering processes. At high momentum transfers, the uncertainty principle forces the extensions of the exchanged virtual photon to small scales. This enables the experiment to probe the proton at small distances. On the other hand, at low photon virtualities Q^2 the photon possesses a larger extension.

In QCD, the factorization ([27], [28], [29]) of the J/ψ production into 3 steps plays an important role. The photon fluctuates into a quark-anti-quark pair before the interaction. In a second step, the $q\bar{q}$ pair interacts with the proton. Finally, the $q\bar{q}$-pair forms a bound state, the vector meson, after the interaction.
The color neutral gluon system exchanged between the J/ψ and the proton is referred to as Pomeron in QCD as well as in the Regge interpretation. To underline the difference to a real particle, it is called an *effective* Pomeron trajectory.

Within QCD, the simplest assumption for the diffractive interaction of the J/ψ and the proton is an exchange of a colorless two-gluon system ([30], [31]). Figure 3.7 shows the lowest order diagram for the elastic process. In the presence of a hard scale, which may be given by

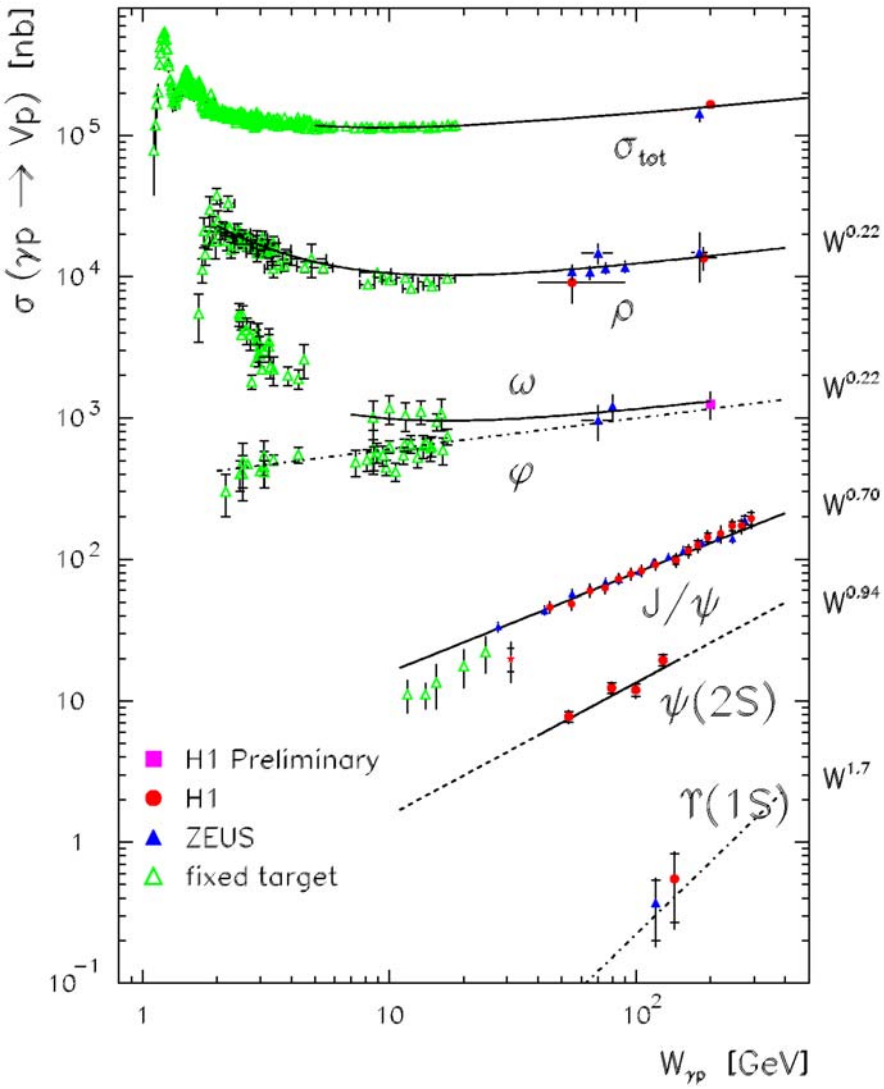

Figure 3.6.: Measurements of the total γp cross section and the cross section for elastic vector meson production as a function of $W_{\gamma p}$ ([16, 17, 18, 19, 20, 21, 22]).

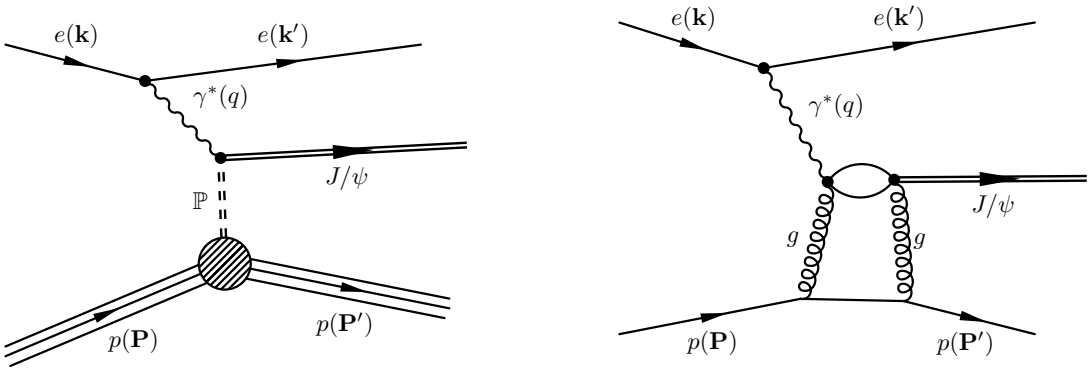

Figure 3.7.: Diagram of elastic J/ψ photoproduction in as modeled by Regge theory (left) and by QCD (right).

a high photon virtuality Q^2 or the mass of a heavy quark m_q[3], the transverse extension of the photon is small and the interaction can be calculated in perturbative QCD. In [32] and [33], the process is calculated in the leading logarithmic approximation (LLA) taking terms of the order of $\alpha_s ln(Q^2_{eff}/\Lambda^2_{QCD})$ into account, where Λ_{QCD} is the QCD scale and the effective hard scale Q^2_{eff} is given by

$$Q^2_{eff} = \frac{Q^2 + M^2_\psi}{4}. \tag{3.51}$$

The differential cross section is calculated by:

$$\frac{d\sigma_{\gamma p}}{dt}|_{t=0} = \frac{\Gamma_{ee} M^3_\psi \pi^3}{48\alpha_{QED}} \frac{\alpha_s(Q^2_{eff})^2}{Q^8_{eff}} (xg(x, Q^2_{eff}))^2 (1 + \frac{Q^2}{M^2_\psi}). \tag{3.52}$$

where

$$x = \frac{4Q^2_{eff}}{W^2}. \tag{3.53}$$

Γ_{ee} is the partial width of the decay $J/\psi \rightarrow e^+e^-$. $g(x, Q^2_{eff})$ is the gluon density of the nucleon. Since $g(x, Q^2_{eff})$ rises steeply with decreasing x equivalent to increasing $W_{\gamma p}$(equ. 3.5, 3.7) and $\sigma_{\gamma p} \propto (xg(x, Q^2_{eff}))^2$, equ. 3.52 yields a steep rise of the differential cross section as a function of $W_{\gamma p}$, which is in agreement with experimental data ([17],[34]). In [32] no prediction for the t dependence of the cross section is made.
The two terms in the last parenthesis in equ. 3.52 correspond to the production with transversely and longitudinally polarized photons, respectively. In [35] the two contributions are modified by different factors taking Fermi motion corrections into account.

A different approach to describe the γp interaction is the colour dipole model ([36],[37],[38]), which also uses the factorisation assumption:

$$A_{\gamma^* p \rightarrow J/\psi p} \propto \Psi(\gamma^* \rightarrow q\bar{q}) \cdot \sigma_{q\bar{q}p} \cdot \Psi(q\bar{q} \rightarrow \gamma^*)$$

[3]For this analysis, $Q^2 \approx 0$ GeV and $m_c = (1.25 \pm 0.09)$ GeV as in [5]

$A_{\gamma^* p \to J/\psi p}$ is the amplitude of the process and $\Psi(\gamma^* \to q\bar{q})$ or $\Psi(q\bar{q} \to \gamma^*)$ are two wave functions. Here, the $q\bar{q}$-pair is set equal to a colour dipole. In contrast to the other approaches, this model does not require a hard scale. The dipole cross section $\sigma_{q\bar{q}p}$ includes soft processes and depends on $\hat{b}$, which is interpreted as the transverse size of the $q\bar{q}$-pair.

In [39],[40], the dipole cross section is given as

$$\sigma_{q\bar{q}p} = \frac{\pi^2}{3}\hat{b}^2\alpha_s(\bar{Q}^2)xg(x', \bar{Q}^2) \tag{3.54}$$

where $\hat{b} < \hat{b}_{Q_0} \approx 0.4$ fm is required. x' and $\bar{Q}^2$ are defined by

$$x' = x(1 + \frac{4m_c^2}{Q^2})(1 + 0.75\frac{\langle\hat{b}\rangle^2}{\hat{b}^2}) = x'_{min}(1 + 0.75\frac{\langle\hat{b}^2\rangle}{\hat{b}^2}) \tag{3.55}$$

$$\bar{Q}^2 = \frac{\lambda}{\hat{b}^2} \tag{3.56}$$

where

$$\langle\hat{b}\rangle^2 = \frac{\lambda}{Q^2 + 4m_c^2} \tag{3.57}$$

and $m_c = (1.25 \pm 0.09)$ GeV denotes the mass of the charm quark. The parameter λ is introduced to determine the dividing line between perturbative and non-perturbative physics. The energy dependence of the effective trajectory $\alpha'_{\mathbb{P}}$ is modeled by the simple equation

$$\alpha'_{\mathbb{P}} = 0.5\frac{\hat{b}^2}{\hat{b}^2 + \hat{b}_\pi^2} \text{ GeV}^{-2}. \tag{3.58}$$

It gives $\alpha'_{\mathbb{P}}(\hat{b}^2 = \hat{b}_\pi^2 \approx 0.65fm) = \alpha'_{\mathbb{P}}|_{soft} = 0.25$ GeV^{-2} and to converge to 0 quadratically at small $\hat{b}$.

Diffractive J/ψ production can be also interpreted in a radiative picture [13]. It describes a time-ordered cascade-like emission of gluons from the $q\bar{q}$-pair, where the momenta of the gluons decrease. The first gluon has a small transverse size. The subsequently following gluons carry smaller momenta and increase in the transverse direction. This more intuitive description of the perturbative process breaks down when the momentum of the last gluon gets too small. Here, non-perturbative forces come into play.
After the interaction with the proton, all emitted gluons are recollected and the $q\bar{q}$-pair forms the J/ψ vector meson. It is this cloud of gluons that leads to the steep rise of the cross section with the energy $W_{\gamma p}$ of the hadronic system. This increase also depends on the transverse size of the $q\bar{q}$-pair. The transverse dimension of the vector meson depends on the quark mass $r_V \propto m_q^{-1}$ with m_q being the respective quark mass. Due to the large mass of the charm quark, the $c\bar{c}$-pair producing the J/ψ has a smaller transverse extension than e.g. the ρ meson, consisting of light u and d quarks plus respective gluons.

In the case of J/ψ, the perturbative process of the gluon emission dominates over the non-perturbative manifestation of the interaction by the last gluon with the proton - even at low photon-virtualities Q^2. For ρ photoproduction, the soft process dominates so that perturbative QCD is not applicable. At higher values of Q^2, where the photon virtuality

provides a hard scale, the rise of the ρ production cross section with $W_{\gamma p}$ has been measured to approach the value of J/ψ photoproduction [18].

3.5. Monte Carlo Simulations

Monte Carlo simulations derive their name from the technical integral role of random number generators to solve numerical integrations over the kinematic variables of scattering amplitudes or to generate physics events according to known probability distributions. In experimental high energy physics, they are used for detector design and optimization, to determine geometrical acceptances and detector efficiences needed for cross section calculations as well as for reproducing statistical signal and background behaviour. Monte Carlo Simulations are conducted in 3 basic steps: *Generation*, *Simulation* and *Reconstruction*. The procedure is described at this point briefly.

First, the generation of physics events is done via numerical integrations or according to known probability distributions. This step of the simulation starts with the initial state particles - here electron and proton - and builds a set of final state particles with four-vector information according to the physics process being studied. Hence, a finite sample of events is produced which represents the kinematic distribution of all subprocesses of the simulated process.

In this analysis, the generator DIFFVM 10.0 [41], was used to generate the process $ep \rightarrow ep\,J/\psi$ and all subsequent decays. It simulates the elastic and diffractive production of vector mesons. This generator is based on the Vector-Dominance-Model and Regge theory, as discussed section 3.3 of this chapter.

$$\sigma_{ep}(Q^2, W, t) \propto (\frac{W}{W_0})^{4\epsilon}(1 + \frac{Q^2}{M_\psi^2})^{-n} e^{b_{el}t} \tag{3.59}$$

Generated four-vectors are then forwarded to the simulation of the H1 detector by the H1SIM software. This package determines the signal response of the detector. A detailed description of the detector geometry and of the absorption properties from various materials is needed in order to simulate the measurement correctly. The simulation is again divided into 2 steps:

GEANT The detector is subdivided into small portions in volume in order to simulate a particles interaction along its track. The software package GEANT calculates the strong and electromagnetic interactions of all particle types under influence of the detector's magnetic field.

H1DIGI The fully realistic digitized response of active detector compartments (from drift chambers, calorimeters to silicon strip detectors) are then simulated respectively by H1DIGI. The H1TRIG software adds a valid trigger simulation for recording the Monte Carlo event.

The result of this procedure are simulated raw data sets that contain the same format and information as if real data would have been written to tape. These Data Storage Tapes (DSTs) are then input to the same reconstruction procedure as real data.

4. The H1 Experiment at HERA

This chapter covers the experimental setup for the measurement of lepton nucleon scattering delivered by the HERA collider facility (*Hadron-Elektron-Ring-Anlage*) at the H1 experiment. The high energy data set used for this analysis was recorded in the years 2006 and 2007. H1 is one of the two collision experiments at HERA where produced electron and proton beams intercept and bunches of both beams are brought to interaction. The accelerator is described, followed by the H1 experiment and its subdetector components as needed for this study.

4.1. The HERA Accelerator

HERA [42, 43] is the only electron-proton colliding beam facility worldwide. It was built at the *Deutsches Elektron Synchroton* (DESY) research laboratory at Hamburg, Germany. As depicted in fig. 4.1, it is enclosed in a fourfold symmetric underground tunnel system, which is built of four straight tunnels of 360 m length, connected by four quarters of a circular tunnel with a radius of 797 m. This gives a total circumference of 6336 m. Inside the tunnel, there are two independent storage rings installed producing counter-circulating beams of electrons and protons with nominal energies of 27.6 GeV and 920 GeV. The electrons are first accelerated in an electron linac to an energy of 500 MeV before they enter two subsequent storage rings (DESY-II and PETRA) for bunching and further acceleration before they are injected into the HERA electron ring for final storage and further acceleration. The protons are stripped from negatively charged hydrogen ions, stepwise accelerated from 50 MeV upto 50 GeV and injected into HERA where they gain the final beam energy of 920 GeV. The limiting factors on accelerating electrons or protons are the compensation of synchrotron radiation for the electrons and the high magnetic field strength to keep the protons in orbit. HERA uses superconducting cavities for electron acceleration and superconducting magnets in the proton ring while the magnets of the electron ring and the cavities of the proton ring are normal conducting.

HERA was authorized in 1984, finished in 1990 and since then upgraded several times [44, 45]. The most important parameter change resulted from changes installed in 2000 from which the determination of the two running period originates, HERA-I (before 2000) and HERA-II after. The HERA accelerator ring provided 4 sites for experimental setup. At two of these locations, classical collider experiments, named H1 [46] and Zeus [47], were built where the beam leptons and protons are brought to collision at a center of mass energy of $\sqrt{s} = 318.4$ GeV every 96 ns leading to a bunch crossing rate of 10.4 MHz. Both Hermes [48] and Hera-B [49] are fixed target experiments using only the electron or proton beam. HERA and its experiments were decomissioned on June 30th, 2007. A summary of nominal beam parameters is given in table 4.1.

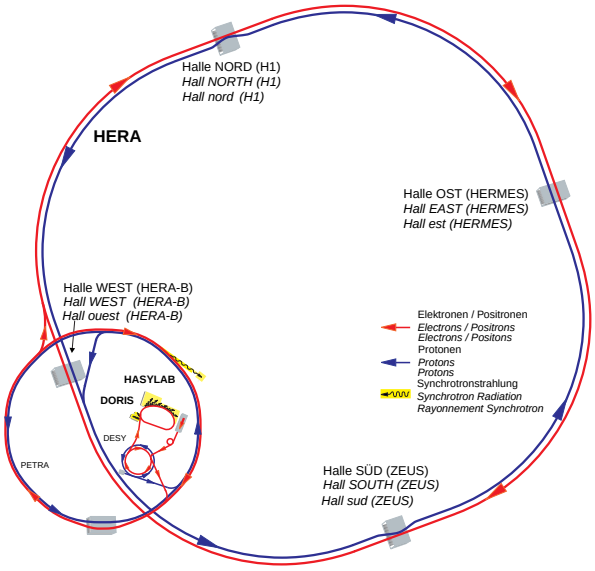

Figure 4.1.: HERA accelerator and tunnel scheme

4.2. The H1 Experiment

The H1 spectrometer [46, 51, 52] is one of two colliding beam experiments at HERA designed to study *ep* interactions. The main body of the detector as depicted in fig. 4.2 covers a volume of $12 \times 10 \times 15$ m^3 with a total mass of about 2800 tons. The detector geometry is azimuthally symmetric around the beam geometry and centered at the nominal interaction point (IP). This setup allows H1 to cover almost a 4π solid angle. The instrumentation, as shown in more detail in fig. 4.3, is enhanced in proton direction due to the comparably high energy of the proton beam boosting the center of mass of the collision into proton direction in the laboratory frame. This behavior defines the proton direction as "forward" and the lepton direction as "backward" . The angular region left between the two is commonly referred to as "central".

The coordinate system used for H1 is a right handed Cartesian system, with an origin close to the nominal one at (0,0,0). The x axis is pointing towards the center of the HERA accelerator ring, the y axis points upwards and the positive z axis is set parallel to the proton beam direction. More conveniently, a spherical coordinate system is often attached to this setup with θ being the polar angle with respect to the z axis ($\theta \in [0, \pi]$) and the azimuthal angle ϕ defined in the x-y plane with respect to the x axis ($\phi \in [-\pi, \pi)$).

The H1 setup follows the standard setup scheme of modern high energy collision detectors and is illustrated in fig 4.2 and 4.3:

Tracking Detectors Moving outward from the beam pipe, H1 contains silicon trackers, proportional and drift chambers. The tracking system is designed to efficiently reconstruct tracks in the region $5^\circ < \theta < 175^\circ$ with an angular precision of $\sigma_\theta \approx 1$ mrad and measure track momenta with $\sigma_p/p^2 \approx \times 10^{-3}$ GeV. In addition, the trackers provide vertex information, trigger signals and particle identification data.

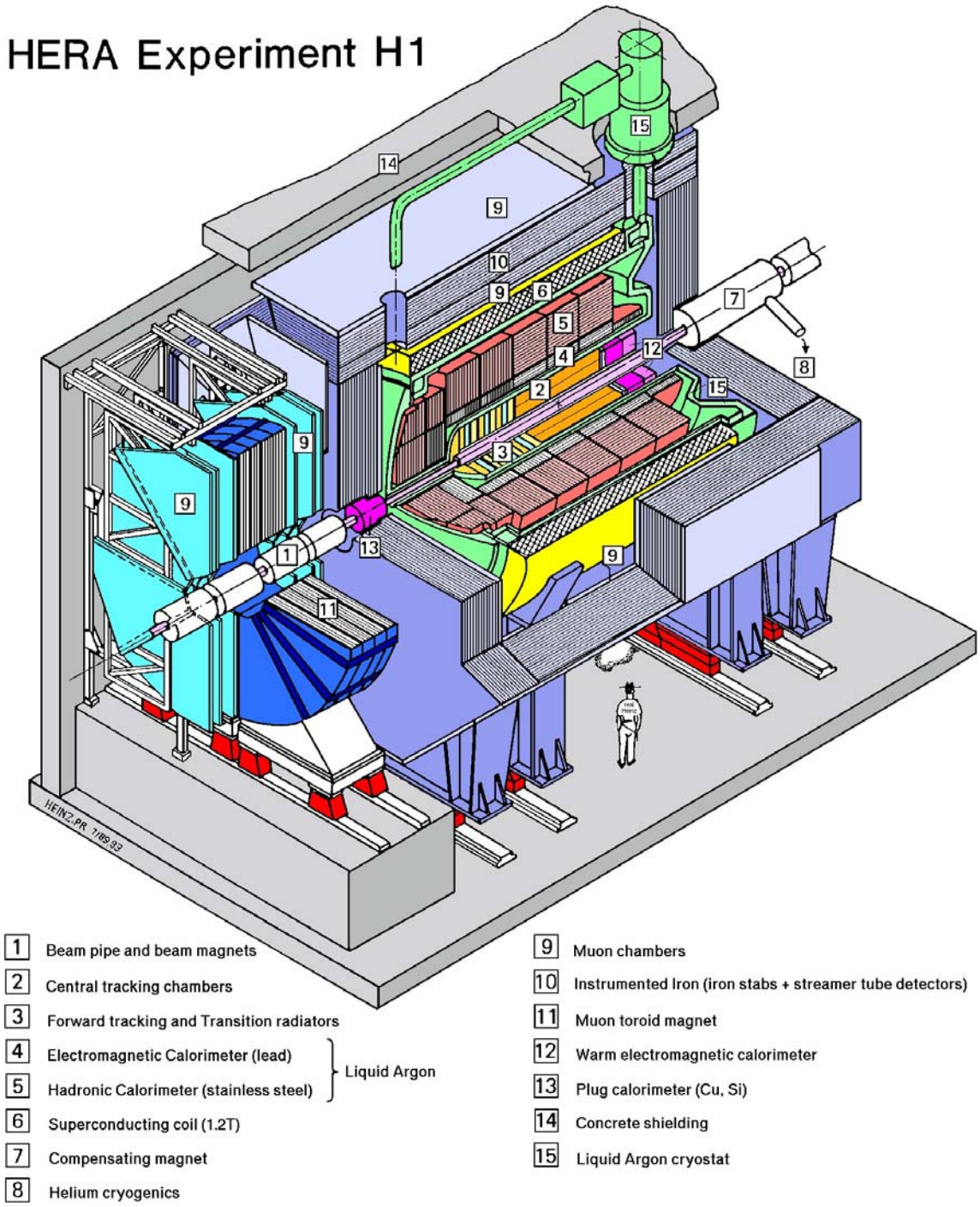

Figure 4.2.: The H1 Experiment in 3D View as of 1993.

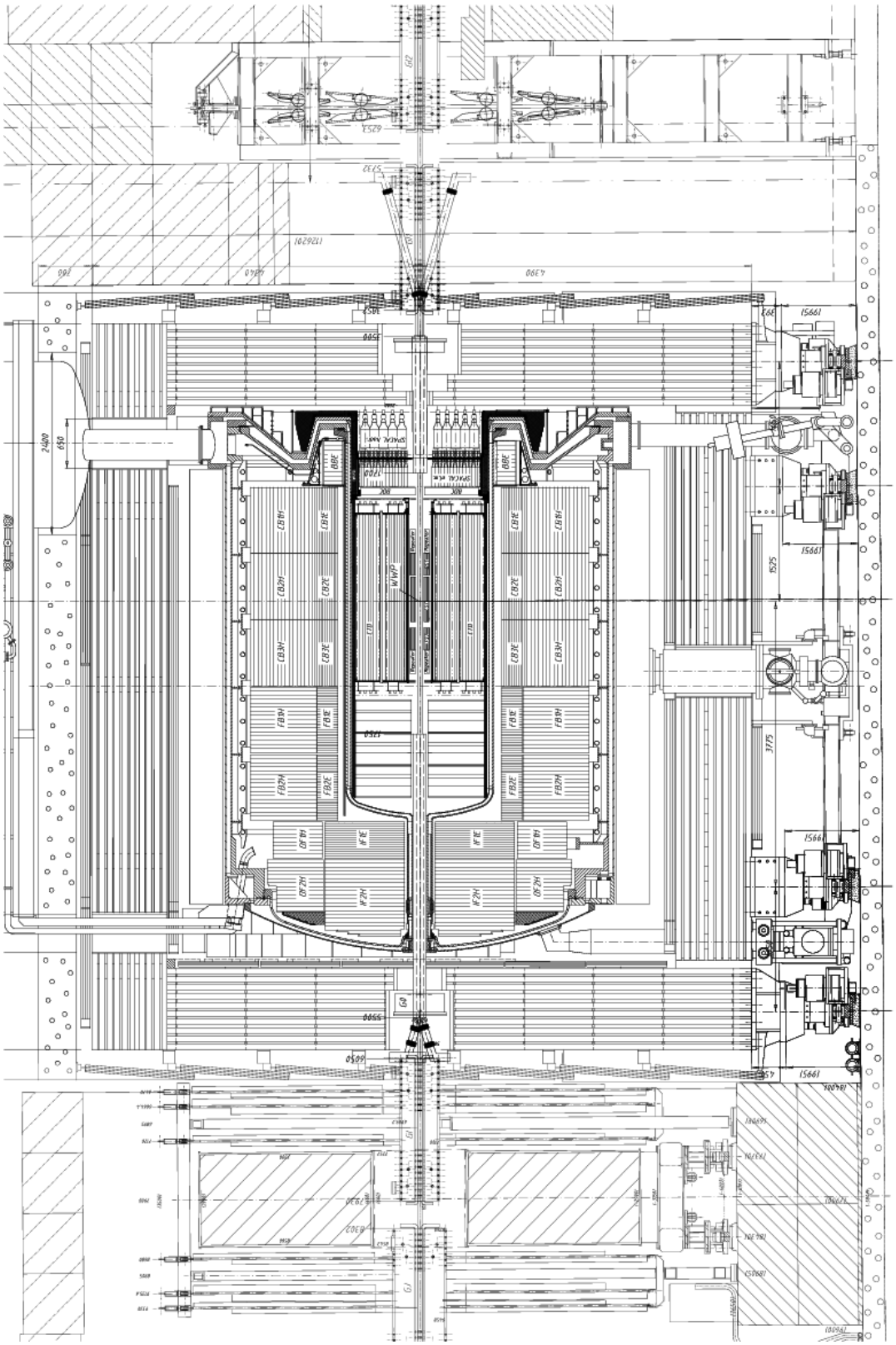

Figure 4.3.: The H1 Experiment in r-z View as of 2006.

Parameter	Units	e-ring	p-ring
Beam energy, E	GeV	27.6	920
Beam current, I	mA	58	140
Particles per bunch, N_{ppb}	10^{10}	4	10.3
Number of bunches, n_{tot}	-	189	180
Number of colliding bunches, n_{col}	-	174	174
β-function at IP, β_x^*; β_y^*	m	0.63; 0.26	2.45; 0.18
emittance at IP, ϵ_x	nm	20	$5000/\beta_y$
emittance ratio, ϵ_y/ϵ_x	-	.17	1
beam size at IP, σ_x;σ_y	μm	112;30	112;30
beam length at IP, σ_z	mm	10.3	191
Polarization	%	45	0
Luminosity, L	$cm^{-2}s^{-1}$	$7.5 \cdot 10^{31}$	
Specific Luminosity, L_s	$cm^{-2}s^{-1}mA^{-2}$	$1.82 \cdot 10^{30}$	

Table 4.1.: Nominal parameters of the HERA facility as listed in [50].

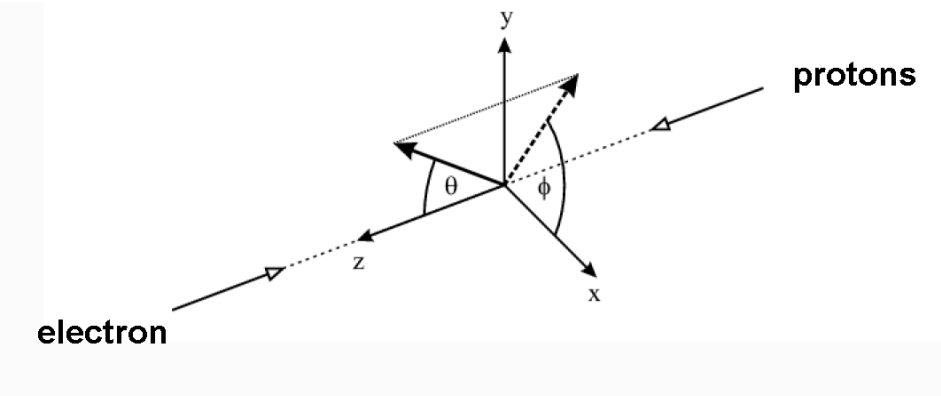

Figure 4.4.: The H1 coordinate system from [53].

Calorimeters Enclosing the H1 trackers, the calorimeters provide high precision energy measurements. The forward and central reconstruction region is covered by a Liquid-Argon Calorimeter (LAr). In the backward direction, where a better energy resolution is needed for scattered electron reconstruction, the instrumentation is provided by a lead-fiber Spaghetti Calorimeter (SpaCal). In addition, a plug calorimeter is setup in the forward region close to the beam pipe.

Magnet The superconducting magnet, needed for momentum measurement of charged particles, surrounds the calorimeters and thus the tracking systems. It provides a magnetic field strength of 1.16 T aligned parallel to the proton beam direction. The 575 cm long solenoid is cooled with liquid Helium.

Muon System The solenoid is surrounded by an iron yoke to return the magnetic flux and to absorb the remaining hadronic showers from the calorimeters. To detect the only particles visible outside the main H1 magnet, which are muons, the iron return yoke has been instrumented with streaming chambers for their identification. In the forward direction, an independent drift chamber with a separate toroid magnet was installed.

Trigger System The main purpose of the H1 trigger system is to select e-p events from the background recorded in H1 and reduce the data volume from processes with high cross sections. It is implemented through the detector subcomponents already described.

Luminosity System The luminosity detectors are not depicted in fig. 4.2 or 4.3. They are located in the tunnel systems in electron direction. Here, the rate of Bethe-Heitler events ($ep \rightarrow ep\gamma$) is measured, since the cross section of this process is well known and can be used as standard candle. Electrons and photons are measured in two separate crystal Cherenkov calorimeters.

Tunnel Systems The tunnel systems are also not depicted in fig. 4.2 or 4.3. They are situated far away from the main detector to study proton diffraction at very low proton scattering angle in the forward direction or trigger photoproduction events in the backward region.

The point of first interaction of a beam lepton with a beam proton is referred to as *primary vertex* and the particles created here are named *primary particles*. Neutral and charged particles are detected by their energy deposition in the calorimeters and, depending on their charge, by the track they leave in the tracking detectors. Muons are detected by a coincidence measurement in the calorimeters, the trackers and the muon system. The missing energy and momentum, e.g. from neutrino production in electroweak charge current interactions, can still be reconstructed from the four-momentum imbalance between summed recorded deposits and the initial state. Weakly decaying particles from the decays of strange, charm and bottom quarks are reconstructed by their decay particles. They leave tracks not fitting to the primary vertex and thus create a *secondary vertex*. Investigating the displacement of the two vertices allows lifetime measurements.

4.3. The Central Tracking Detectors

The H1 central tracking detectors follow a concentric onion-like setup around the beam pipe. As shown in fig. 4.5, starting from the elliptical beam pipe inside, the installation contains the Central Silicon Tracker (CST, 2 layers of Silicon strip ladders visible in profile), the Central Inner Proportional Counter (CIP, 1st dense circular structure), the 1st Central Jet Chamber (CJC1, wire planes tilted versus axial symmetry), Central Outer Z-chamber (COZ), the Central Outer Proportional chamber (COP) and the 2nd Central Jet Chamber (CJC2). All chambers have independent gas volumes and separate electronics shielding. The complete structure is housed in a 4 mm strong aluminum cylinder.

A summary of the central detector geometrical dimensions is given in table 4.2.

4.3.1. The Central Jet Chambers (CJC)

The two concentric Central Jet Chambers ([54]) are the main tracking devices of the H1 experiment. They are able to measure the momentum and the type of a particle, using the deposited charge left by it when penetrating the chamber. They are gas drift chambers.

The measuring principle of the CJC bases on the observation that charged particles ionize atoms and molecules when passing through matter. Gas drift chambers use a gas mixture as identification medium. As depicted in fig. **??**, the chamber houses wires strained in parallel to the beam and the magnetic field between which a potential difference is produced. The

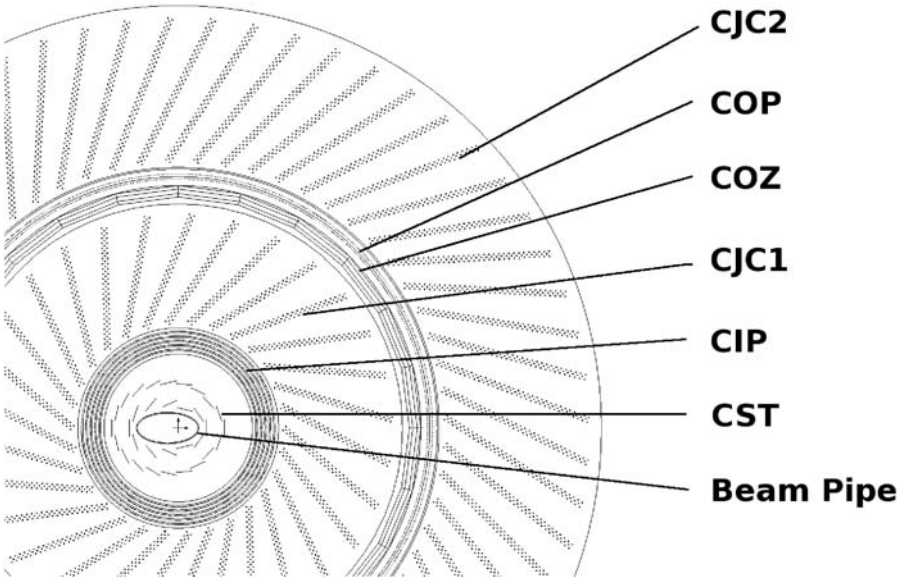

Figure 4.5.: The H1 central tracking detectors in r-ϕ view.

wires are setup to guarantee a mostly homogeneous field distribution between the wire planes. The space between cathode and potential wires is called drift space. Signal wires are located between the potential ones.

Here, the electric field strength increases towards the signal wires in order to guarantee that charge carriers produced by ionizing particles are propelled towards them. Meanwhile, the charge carriers constantly collide with gas molecules and produce more charge carriers resulting in a gas amplification. The two competing effects of acceleration through the electric field and deceleration by means of collisions ensure a constant drift velocity, whereas ever more charge carriers are produced. This results in a avalanche which can be detected by the deposited charge in the signal wires. Their read-out signals are amplified and digitized by Flash-ADCs.

Parameter	Units	CJC1	CJC2	CIP	COP	COZ	CST
Active Length	mm	2200	2200	2190	2190	2160	114
Active Zone from Z	mm	-1125	-1125	-1127	-1127	-1105	-221
Active Zone until Z	mm	1075	1075	1043	1043	1055	221
Active Zone from θ	degrees	11	26	9	26	25	7
Active Zone until θ	degrees	169	154	171	155	155	173
Inner radius	mm	203	530	157	520	460	-
Outer radius	mm	451	844	193	491	485	-
r-ϕ resolution	mm	0.17	0.17	-	-	58	0.012
z resolution	mm	22	22	-	-	0.2	0.022

Table 4.2.: Key Parameters of the Central Tracking System at H1.

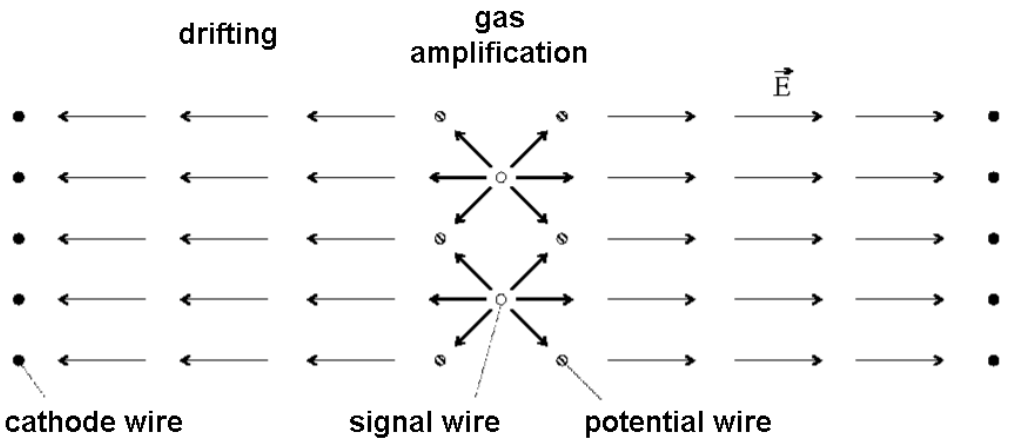

Figure 4.6.: The CJC measuring principle in r-ϕ view.

The structure of the two CJCs has already been introduced in table 4.2. The inner chamber, CJC1, has 720 readout wires. They are subdivided in 30 cells in ϕ and 24 layers in radial direction. The outer chamber, CJC2, contains 60 cells and 32 layers in equal setup. The wire planes are tilted by approximately 30° against the radial axis in the r-ϕ plane. This allows a high energetic track coming from the nominal vertex to pass through anode wire planes and to determine the absolute timing of the detector.

The charge deposited on the wires is read-out at both ends with a constant frequency of 104 MHz. From the time when the signal is produced and the interaction has occurred, the drift time can be calculated. Knowing the drift speed, this results in the drift length which is interpreted as the distance between the particle track and the signal wire. At this point, one cannot decide from which side of the wire the signal originated, creating a left-right ambiguity. This would result in a double reconstruction of the particle track. Each signal contributes a hit which is the input for the track reconstruction algorithm. The tilted cells allow a track to pass several cells and to create so called *track segments* reconstructed from close by hit clusters. Finally, only segments produced by a real particle fit to a common track and are combined to calculate momentum and energy information of the passed particle.

The CJC design and calibration allows a r-ϕ resolution of $\sigma_{r-\phi} = 170$ μm. From the ratio of the charges recorded at each end of a signal wire, the z position of the hit is recorded with a resolution of $\sigma_z = 2.2$ cm. From the total charge recorded per track, the energy loss dE/dx of a particle can be measured and used for particle identify with a relative resolution of 7%.

4.3.2. The Central Z-Chambers (COZ)

The COZ is a cylindrical drift chamber, composed of 24 rings in z, each 9 cm wide. The measuring principle is equivalent to that described for the CJC in section 4.3.1. The charge carrier

avalanche drifts to the positive z direction contributing to the data gathered for reconstructing a particle track in the central region. For further details, see [55, 54].

4.3.3. The Central Proportional Chambers (CIP, COP)

The CIP and COP are complimentary cylindrical multi-wire proportional chambers, used to supply fast trigger signals on the z position of the primary vertex. For details on the design, see [56, 57]. Most importantly, the CIP signals provide a level one trigger bit used to reduce event rates as will be explained in section 4.7.

4.3.4. The Central Silicon Tracker (CST)

The CST, [58], is a silicon vertex detector equipped with double-layer, double-sided, double-metal silicon sensor ladders. The arrangement of the silicon ladders follows the elliptical beam pipe geometry [59]. For the detailed design, please refer to [58]. The CST read-out and measurement principle is similar to that of FST and BST as will be described in sections 4.5.2 and 4.5.3. The signal to noise ratio (S/N) achieved for p-side sensors is 19 and for n-side sensors 8. This results in a hit resolution in r-ϕ of $\sigma_{r-\phi} = 12$ μm which allows precise reconstruction of secondary vertices and the identification of weak decays of heavy quarks.

4.3.5. The Liquid Argon Calorimeter (LAr)

The Liquid Argon Calorimeter was designed to complete the track momentum measurement provided by the tracking system with a precise energy measurement in order to allow a clear distinction, identification and measurement of electrons, muons, photons, neutral hadrons and jets in an environment of high particle density. The LAr was installed between the tracking system and the superconduction magnet coil to minimize the amount of dead material in front of the calorimeter. The geometric acceptance of the LAr is to $4^\circ < \theta < 154^\circ$ by design.

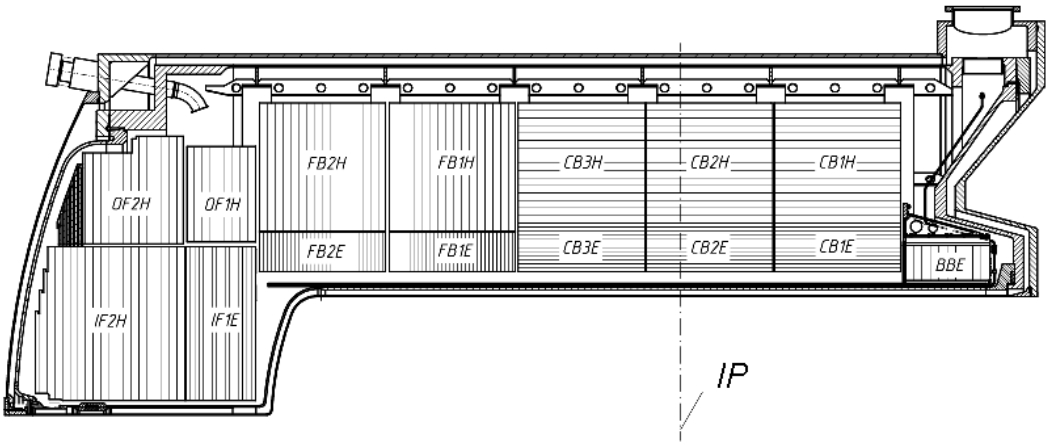

Figure 4.7.: The LAr system in r-z view. The abbreviations F/C/B stand for the forward, central or backward location of the segment in the detector. E/H denotes the electromagnetic or hadronic component of the calorimeter system.

The LAr Calorimeter is a high granularity sampling calorimeter divided into an electromagnetic part (eLAr) and a hadronic part (hLAr). The detector is segmented in Z into 8 self-supporting wheels where each of them is again divided into 8 identical octants in ϕ as depicted in fig. 4.7 and 4.8. The active medium of the LAr is liquid argon cooled down by a gaseous helium cryostat.

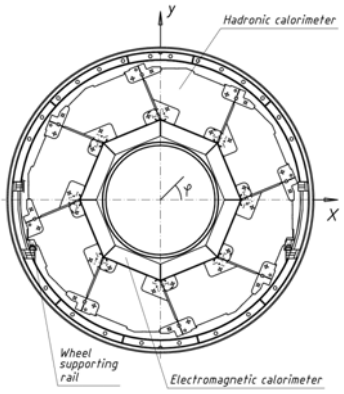

Figure 4.8.: The LAr system in r-ϕ view.

The LAr was built in a sandwich design of 19 mm stainless steel absorber planes alternating with 4.4 mm liquid gas gaps and G10 pads designed to collect deposited charges. The eLAr system is mounted on the rigid structure defined by the hLAr with alternating 2.4 mm lead absorber planes, 2.25 mm active material, a pad readout plane and a high voltage layer. The orientation of the planes was set for particles produced at the interaction point to reach the LAr planes under an angle not smaller than 45° on average. This is the reason why the orientation, as in fig. 4.7, changes from central to forward region. The total thickness of the eLAr varies from 20 to 30 radiation lengths for electrons and 1 to 1.4 interaction lengths for hadrons. The hLAr provides 5 to 9 interaction lengths. The energy resolution of the eLAr amounts to $\sigma_E/E = 12\%/\sqrt{E/GeV} \oplus 1\%$ and $\sigma_E/E = 55\%/\sqrt{E/GeV} \oplus 2\%$ for the hLAr. For more details, the reader is referred to [52, 60].

4.4. The Central Muon Detectors

4.4.1. The Central Muon Detector (CMD)

The iron yoke surrounding the central solenoid magnet is the central muon detector of H1. Besides being instrumented with streamer chambers for identifying muons, it was built to return the magnetic flux of the magnet and to act as tail catcher for incompletely absorbed hadronic showers from the Liquid-Argon Calorimeter (LAr). The CMD is subdivided into 64 modules which built 4 modules: the forward endcap ($5° < \theta < 35°$), the forward and central barrel ($35° < \theta < 130°$) and the backward endcap ($130° < \theta < 175°$).

The installation consists of a 10 layer stack of iron plates with single streamer chambers in-between all but the fourth and fifth plate, which houses a double streamer layer as shown in fig. 4.9. In addition, the inner and outer sides of the iron yoke contain three more layers

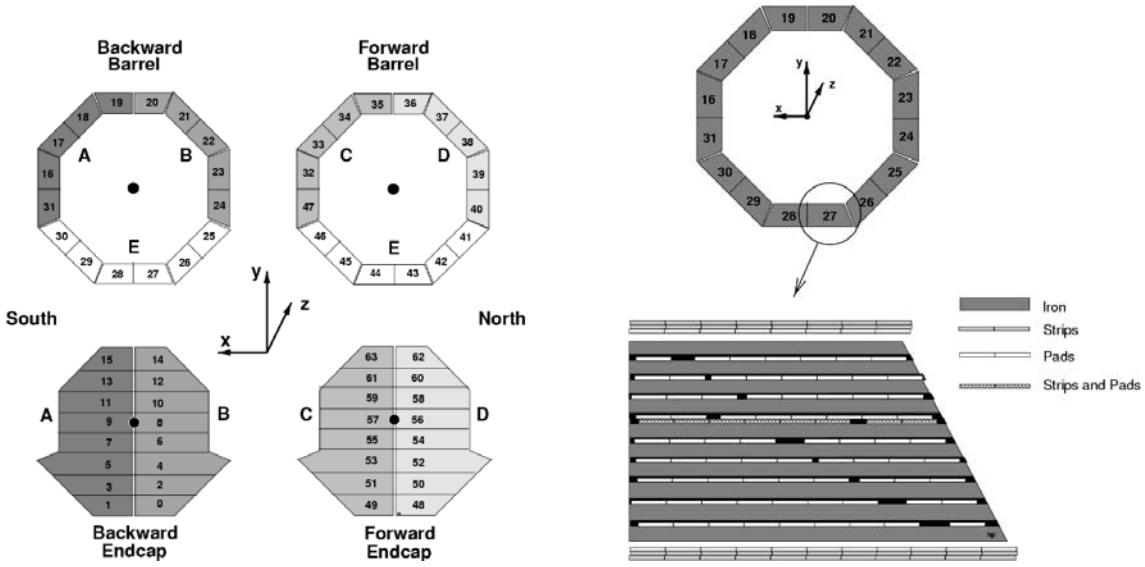

Figure 4.9.: CMD modules and sectors in r-ϕ view (left) and one barrel segment sliced in r-z view (right) to show the setup of the instrumented 10 layer iron plate structure plus streamer chambers.

of streamer chambers, called muon boxes. The CMD thus consists of 16 layers. One layer is made from rectangles with 2 opposite profiles housing each 8 streamer tubes with cross section surfaces of 9×9 mm^2.
The inward side of the tubes is coated with graphite and is used as cathode. Right in the cylindrical center, a copper beryllium wire of 100 μm in diameter is strained along the tube direction. In order to gain a space information, two layers in the muon boxes and the double layer of the interior instrumentation are equipped with influence electrodes. With this, the detection reaches a spatial resolution of $\sigma_\perp = 4$ mm perpendicular to the wires and $\sigma_{||} = 1.2$ cm in parallel. The momentum resolution of the CMD given in [61] to be $\sigma_p/p = 0.35$.

Limited by the overall H1 design, some parts of the muon detector are not instrumented, which result in the holes shown in fig. 4.10 where i.e. the supply of liquid argon or the H1 footing is located.

4.4.2. The Forward Muon Detector (FMD)

As depicted in fig. 4.3, the Forward Muon Detector was placed outside the H1 iron return yoke and copes for the asymmetric HERA kinematics due to the very different proton electron energies.

The FMD was designed to measure high momentum muons in the polar range of $6° < \theta < 18°$. A schematic illustration of its substructure is given in fig. 4.11. The indicated toroidal magnet has an inner radius of 0.65 m and an outer radius of 2.9 m. The toroid extends for 1.2 m in z. The magnet is built from 8 solid iron modules which were assembled into half toroids. The magnetic field varies from 1.75 T at the inner to 1.5 T at the outer radius.

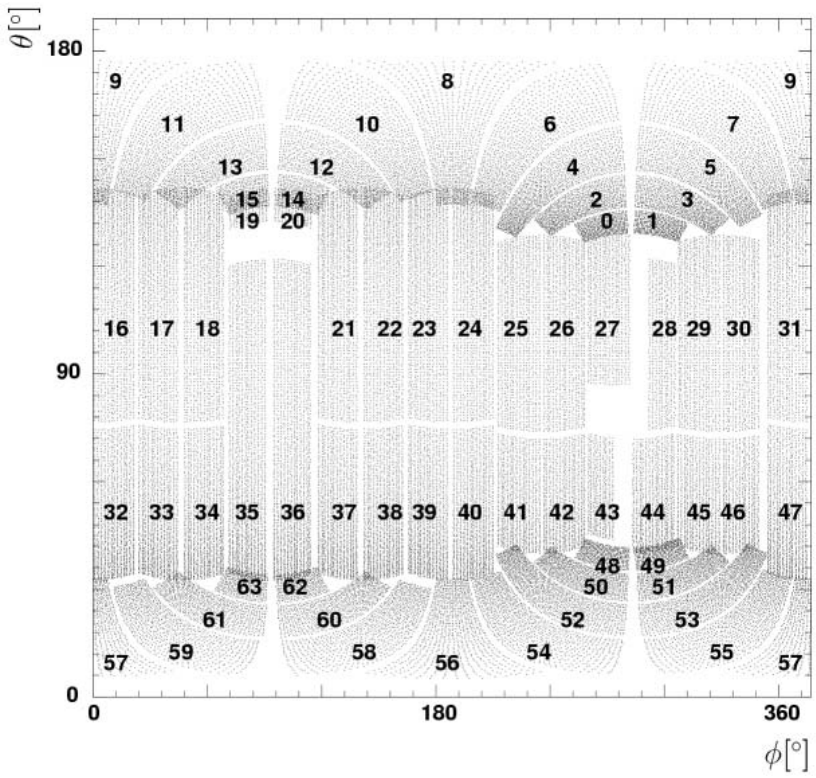

Figure 4.10.: The CMD projected into the θ-ϕ plane using an inline Monte Carlo simulation, as in [62] (0-15: forward endcap, 16-47 barrel, 48-63 backward endcap).

The toroid is surrounded by a symmetric sandwich-like setup of drift chambers to measure the muon track angle θ, ϕ and its momentum. Closest to the magnet, a θ plane was installed followed by a ϕ plane, which was designed like the other planes except for the drift chambers to be aligned perpendicular to those in θ planes, as illustrated in fig. 4.12.
Each plane consists of a double layer of drift cells arranged at a half-cell staggering which resolves left-right ambiguities. The full diameter of a complete octant plane reaches up to 6 m. As can be observed in fig. 4.11, the angle measurement systems allow to record the track polar angle before and after a particle passes the toroid, which is crucial for measuring its momentum through the acting Lorentz force.
The minimum momentum resolution at the lower threshold of 2.25 GeV is $\sigma_p/p \approx 22\%$.

4.4.3. The Central Muon Identification

Until 1994, muon identification at H1 relied on the instrumented iron as muon identificator only. This poses two pitfalls to the user: firstly, tracks need a minimum of $|p| \approx 2$ GeV to reach the iron. To pass it and thus allow a track reconstruction from iron hits, a yet still higher momentum is necessary. Muons as decay particles from vector mesons mostly posses lower momenta. Hence, an identification algorithm was developed in order to use the calorimeter signature of a track for identification, see [63].

When passing through matter muons and electrons loose energy mostly by electromagnetic

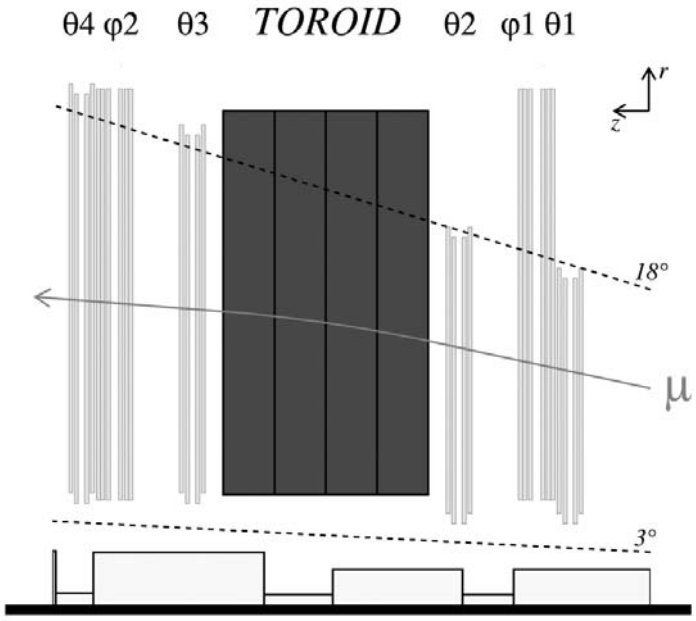

Figure 4.11.: FMD in schematic r-z view. The dashed lines correspond to the geometrical equivalent in θ. Below $\theta = 3°$, a scheme of the HERA beam line is drawn.

interaction with nuclei. The relevant processes are ionization, bremsstrahlung and pair production. For muons, ionization is dominant, because radiative energy losses are negligible for muons with energies $E_\mu < 100$ GeV since the cross section of radiative processes goes with $\sim 1/m^2$. In comparison to electrons, this results in a suppression of radiative processes for muons of 5 orders of magnitude $(m_e/m_\mu)^2 = 2.34 \cdot 10^{-5}$ [5].

The differential energy loss per distance of ionization processes is described by the Bethe-Bloch equation:

$$-\frac{dE}{dx} = 2\pi N_A r_e^2 m_e c^2 \rho \frac{Zq^2}{A\beta^2}[ln(\frac{2m_e c^2 \gamma^2 \beta^2 W_{max}}{I^2}) - 2\beta^2 - \delta - 2\frac{C}{Z}] \tag{4.1}$$

Here, N_A notes the Avogadro constant, m_e the classical electron radius, r_e the electron mass, ρ the material density, Z the atomic and A nucleon number, q the charge of the ionizing particle, W_{max} the maximum energy transferred upon a collision, I the effective ionization potential, ρ the density correction and C a correction factor for the shape of the nucleon's electron shell and $\beta = v/c$ with v being the velocity of the ionizing particle.

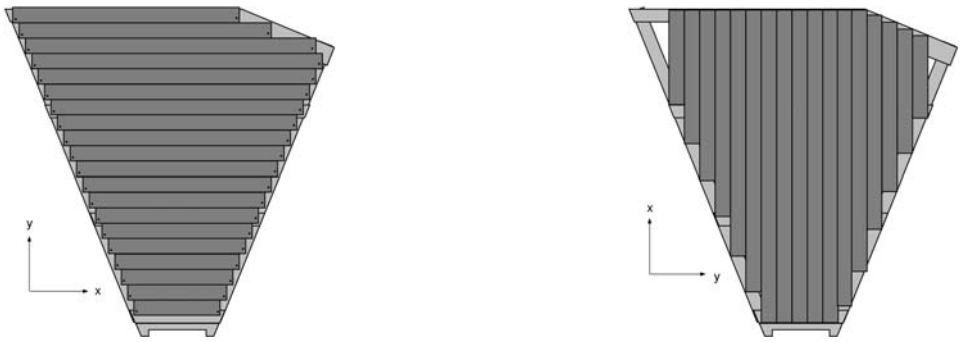

Figure 4.12.: FMD θ (left) and ϕ octants in r-ϕ view. The grey bars indicate drift chambers. The coordinate system depicted is an intrinsic octant one and does not correspond to the general H1 system.

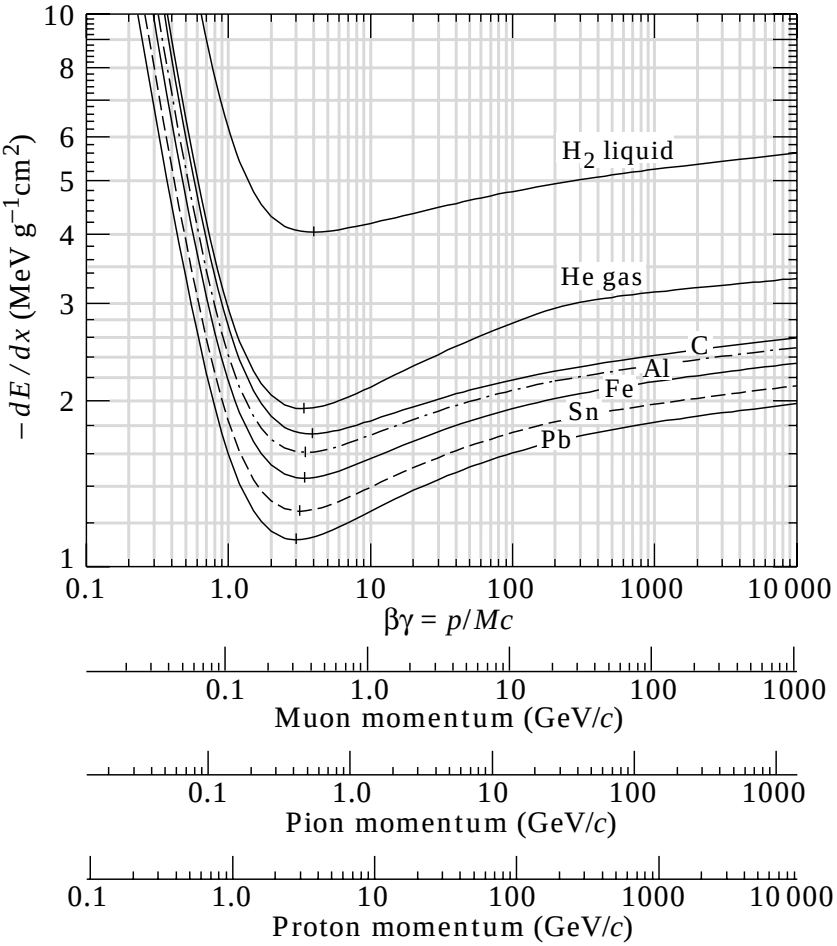

Figure 4.13.: Bethe-Bloch energy loss of protons, pions and muons in various target materials as indicated in the plot, see [5].

fig. 4.13 depicts the Bethe-Bloch behavior of muons, pions and protons in different absorber materials [5]. It can be divided into 3 phases:

low energies	$\beta \leq 1$	High energy loss proportional to β^{-2}.
$E_\mu \approx 300$ **MeV**	$\beta \propto 3$	Minimum ionization loss.
high energies	$\beta >> 1$	Slow rise to infinity, ionization loss for muons due to relativistic effects.

Particles in the minimum of the ionization curve are called *Minimum Ionizing Particles*, so are muons at H1. The total energy loss of muons in the LAr was measured to $dE/dx \approx 0.01$ GeV cm^{-1} by [63]. Taking into account, that the LAr in the central region has a radial dependency of $L \approx 1.3$ m, the total energy needed for muons to pass the LAr completely is $E_\mu \geq 1.3$ GeV. The different Bethe-Bloch behaviors of various particle types results in a large variety of detector signatures produced by them when passing through the H1 LAr. These differences are input to the KALEP identification algorithm [63, 64, 65] to identify muons and calculate estimators to account for the quality of the identification, which are introduced briefly in the following.

As illustrated in 4.14 and crucial for the definition of estimators, all tracks with $|p| > 500$ MeV are parameterized as a helix and extrapolated into the calorimeter. Then, all cells with an energy e_j of more than 10 MeV in two cylinders around the projected track of radius $r_a = 15$ cm and $r_b = 30$ cm suppressing further background contributions. The radii are chosen to contain the electromagnetic shower of an electron completely (15 cm) and 90% of a hadronic shower (30 cm). To construct the estimators, each cell is identified with a distance l_j measuring the length from the tracks entry at the octant limit to the cell. Finally, a weight function h_j is accorded to each cell following a Fuzzy logic distribution being one inside the given radii and quickly falling to zero outside.

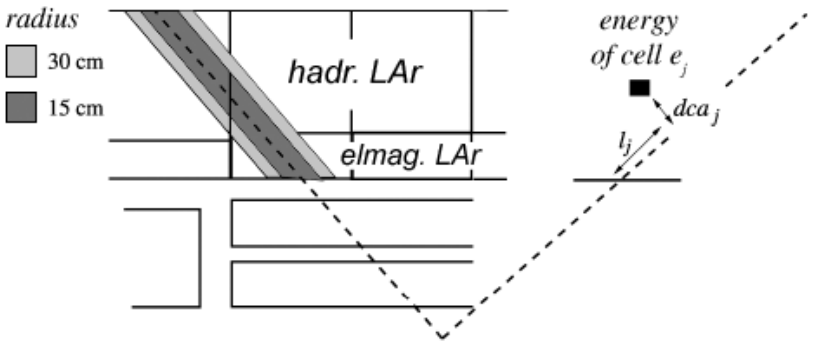

Figure 4.14.: KALEP estimator measurement scheme for the H1 LAr as in [63, 64, 65]. The dashed line corresponds to an extrapolated track helix to the calorimeter.

This results in 4 estimators:

G_1	**eLAr energy inside** r_a	$G_1 = \sum_{j \in N(r_a)} e_j$
G_2	**total LAr energy inside** r_b	$G_2 = \sum_{j \in N(r_b)} e_j \cdot h_j$
G_3	**distance from entry to last cell inside** r_a	$G_3 = max(l_j \cdot h_j(r_a), \forall j)$
G_4	**summed length of hLAr cells inside** r_a	$G_4 = \sum_{j \in N(hLAr)} l_j \cdot h_j(r_a)$

As intermediate step, each estimator is compared to empirical upper limits u_i and lower limits l_i inside which one expects the values for muons. One now calculates the deviations of the estimators to their limits, as:

$$d_i^l = \begin{cases} min(G_i - l_i, 1) & \text{for } G_i > l_i \\ 0 & \text{else} \end{cases} \tag{4.2}$$

$$d_i^u = \begin{cases} min(u_i - G_i, 1) & \text{for } G_i < u_i \\ 0 & \text{else} \end{cases} \tag{4.3}$$

These deviations are then combined with weight factors N_i and summed to give a final combined quality D.

$$D = min(\sum_i [(\frac{d_i^l}{N_i})^2 + (\frac{d_i^u}{N_i})], 1) < C_Q \tag{4.4}$$

C_Q is a constant upper bound to finalize the muon quality calculation and order the resulted identifications in quality classes as shown in table 4.3. The KALEP algorithm is implemented in the H1 analysis framework as an offline muon finder algorithm. The latter combines muon signals from the central muon detectors and the forward muon detector introduced below. Table 4.3 shows the incorporation of the three muon identification devices into on final quality term.

Q_μ	Muon Quality	Limit C_Q
0	no LAr signal	-
1	weak muons	0.5
2	medium muons	0.1
3	good muons	0.015
+10	muon detected in CMD	
+100	muon detected in FMD	

Table 4.3.: Muon Identification qualities Q_μ at H1.

4.5. The Backward and Forward Silicon Tracker

4.5.1. Silicon Detectors

Both the Forward and Backward Silicon Tracking detectors (FST, BST) at the H1 Experiment use Silicon as active material. Silicon is a semiconducting material, showing insulator properties at temperatures close to 0 K. At room temperatures, semiconductors allow electric currents to flow due to their unique charge carrier energy scheme.
All semiconductors are crystalline materials. To obtain them either pentavalent (donors) or trivalent (acceptors) elements are implanted in a crystal lattice of atoms having four valence electrons. Due to the produced excess (deficit) of free charge carriers when introducing donors (acceptors), materials with electron (hole[1]) conductivity are called *n(p)-type*.

Semiconductors are used as p-n junction materials in a high energy detector. In a p-n junction element, the combination of the two opposite materials creates a charge concentration difference between both ends. Electrons and holes drift towards the side with opposite charge and recombine where they meet. This creates a depleted zone with a poor or zero free charge carrier density. This process induces an electric field in the zone, forcing the remaining charge carriers to leave it. This effect can be enhanced by applying a bias voltage resulting in a yet larger depleted zone.

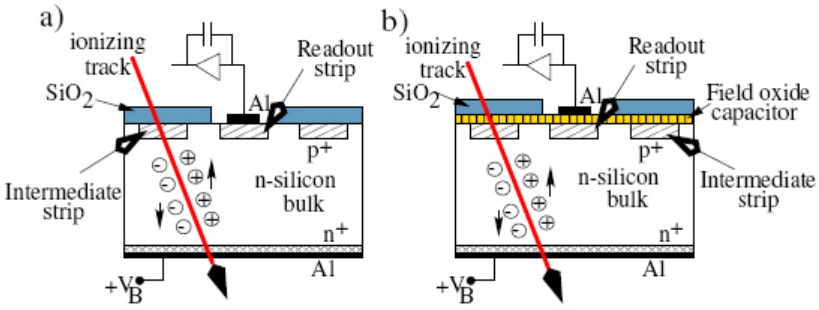

Figure 4.15.: Schematic view of the passage of a particle through a semiconductor detector cell with readout elements. a) DC coupled readout, b) AC coupled readout.

As indicated in fig. 4.15, charged particles ionize matter when passing through. This effect is used in semiconductors for detection. The depleted zone is the active material where passing particles produce electron-hole pairs. The produced charge carriers are subject to the electric field and forced to the respective side of the cell - electrons to n^+ and holes to the p^+ electrode (see fig. 4.15). There the incoming charge carriers are picked up and recorded by a charge sensitive preamplifier.

FST and BST have microstrip sensor elements composed of separate strips made from high resistivity n-type silicon on which p^+ doped strips are implanted with an n^+ strip on the other side. In silicon, a charged particle needs 3.62 eV of energy to produce one

[1] Holes in solid state physics denote atomic lattice impurities, where an electron has left the valence band of a material leaving a conceptual hole behind by disturbing the charge balance and thus producing a positive charge there.

electron-hole pair[2]. The sensor is 300 μm thick which corresponds to 25000 electron-hole pairs produced by a minimum ionizing particle passing perpendicularly through the strip. The time resolution of a silicon detector is very good, since the drift time of electrons (holes) inside the cell amounts to 10(30) ns. In very pure silicon, recombinations occur on average every 1 ms, almost the complete amount of charge can be read out.

4.5.2. The Forward Silicon Tracker (FST)

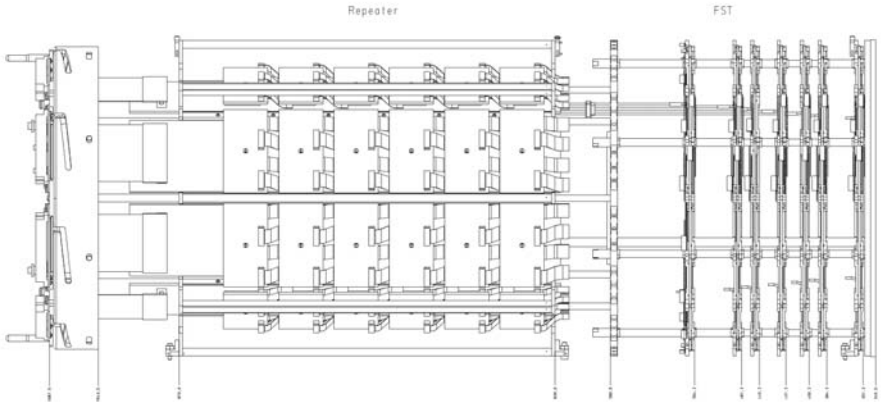

Figure 4.16.: FST in r-z view.

fig. 4.3 shows the FST and BST setup in the H1 tracking system. The FST contacts the +z crid of the CST on one side and the +z end of the central tracker on the other. The radial extension of the FST is limited by the beam pipe and the CJC. It is divided into an active part, installed close to the nominal interaction point and the read-out part with the front-end readout electronics further in +z. The active part contains 5 carbon-fiber-composite wheels equipped with single layer ϕ strip silicon sensors.

Every ϕ wheel is equipped with two layers of 12 modules each mounted back-to-back as illustrated in fig. 4.17 and 4.16. Each ϕ strip sensor contains 640 parallel AC coupled silicon strips with a pitch of 72 μm. They surround the beam pipe in cylindrical symmetry. The sensors facing (back to) the nominal vertex are called u(v) types. Due to the back-to-back mounting, forward and backward layer strips of one wheel intercept at an azimuthal angle of 22.5° and thus create an FST intrinsic coordinate system which allows a two dimensional hit reconstruction of recorded signals. The modules on one side of the wheels are staggered in z to allow a module overlap of 1° in ϕ.
Every third strip is read out by the AC coupling composed of the aluminum strip of same length, as shown in fig. 4.15. The read-out pads are combined to 5 groups of 128 read-out channels each and bonded to the front-end electronics. This results in a total number of 84480 channels. For further details on the FST design and data taking, refer to [68].
The nominal θ range of FST tracks of at least 5 hits is estimated from its geometry to be

[2]The energy gap of silicon is of the order of 1 eV. Two thirds of the deposited radiation energy excite lattice vibrations.

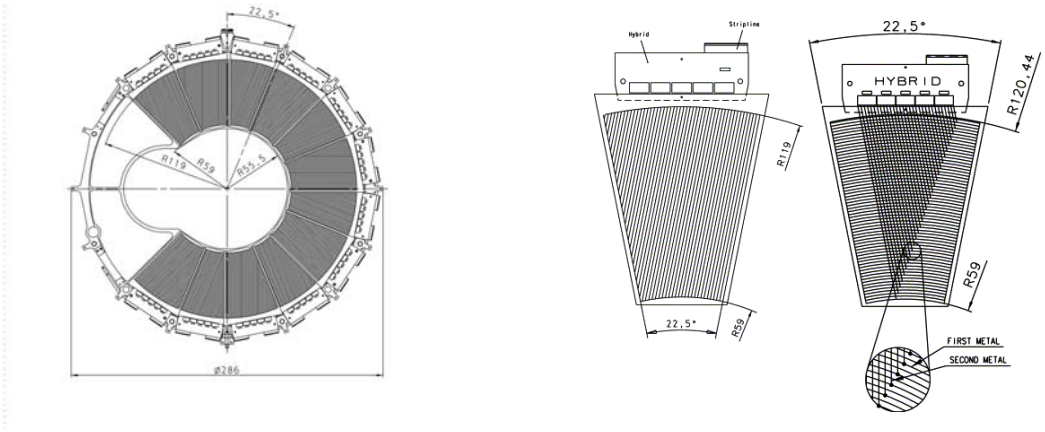

Figure 4.17.: Left: sensor wheel in r-ϕ view and single sensor segments (right) with strip overlay, [66, 67].

$7.8° < \theta < 15.9°$. Due to Gaussian distribution of the vertex z component of $\sigma \approx 10$ cm, the polar acceptance is smeared between 5° ($z_{vertex} = -35$ cm) and $\propto 40°$ ($z_{vertex} = 35$ cm).
One quarter of the FST is not instrumented limiting the ϕ range to $|\phi| < 135°$ due to the elliptical beam pipe. The p_t resolution of the FST varies with the p_t of the track from $\sigma_{p_t}/p_t \approx$25% to 35%. Its hit resolution in u/v is $\sigma = (12 \pm 2)\mu$m, [68, 69]. This resolution can only be achieved after precise alignment of the detector in the H1 experiment. A study of FST acceptances will be given in chapter 6.

4.5.3. The Backward Silicon Tracker (BST)

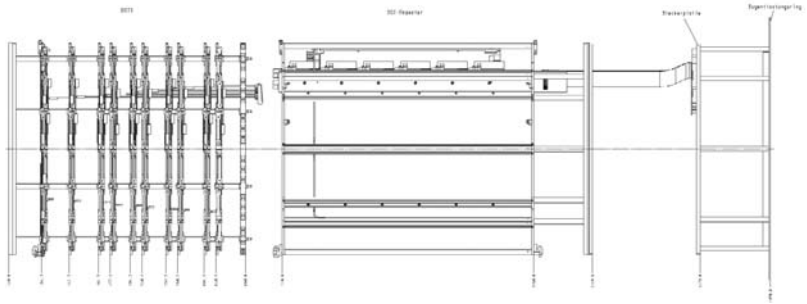

Figure 4.18.: BST in the r-z view,[66].

As depicted in fig. **??**, the BST was installed in the backward region of the central tracking system. Since the FST was designed as a mirror of the BST, both detectors greatly equal in measurement technique and design, fig. 4.18.
The BST contains one more double layer sensor wheel and thus can deliver signals from 92160 channels. It also misses four sectors in ϕ due to the elliptical beam pipe. The θ acceptance of the BST ranges from 165° to 174°. The p_t and ϕ acceptances and resolutions

are equal to those of the FST.

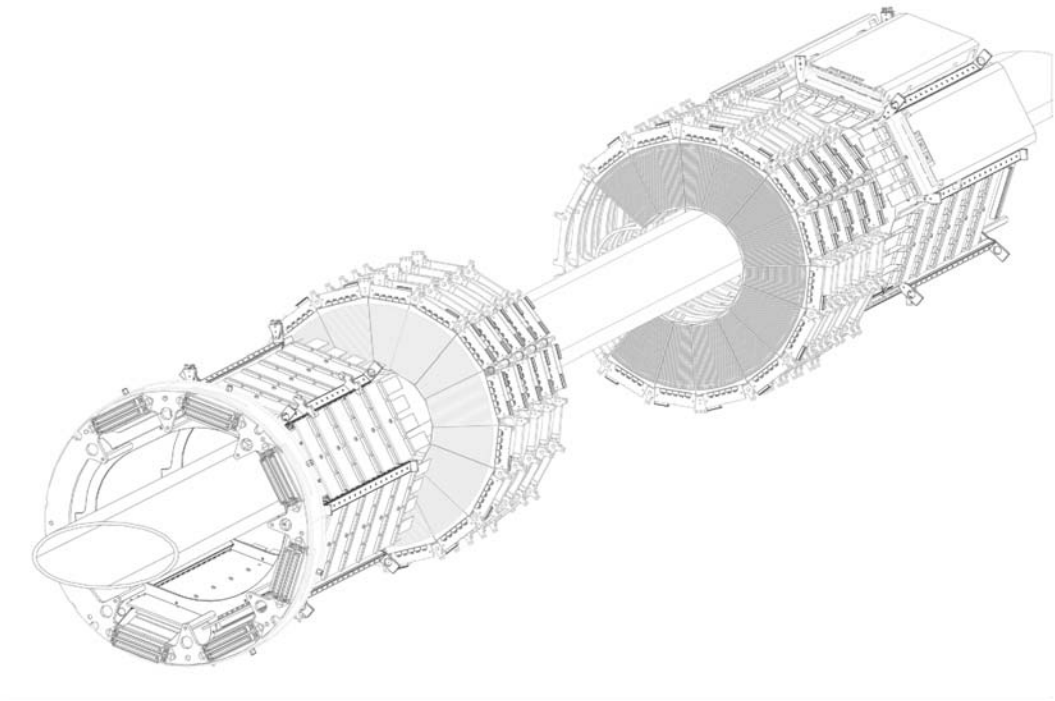

Figure 4.19.: FST and BST in 3D view around the beam pipe, [66].

The motivations to implement both detectors are however very different. FST and BST were both built to provide exact z vertex measurements in kinematical regions where the central vertex is poorly determined and thus enhance the central tracking. Studies of this effect have been done by the author as preface of this investigation [70].
In addition, both instruments show good tracking capacities. This qualifies them for physics studies on various topics to extent the range of the central tracking. The BST primarily serves as high precision detector to characterize the scattered beam lepton in DIS events. Together with the energy measurement in the SpaCal this allows for a precise inclusive measurement of DIS event kinematics whose errors enter directly DIS cross-section measurement.

4.6. The electromagnetic Spaghetti Calorimeter (SpaCal)

The main purpose of the Spaghetti Calorimeter (SpaCal) is to securely identify the scattered beam electron and precisely measure its polar angle and energy as close as possible to the beam pipe. The SpaCal acceptance is limited to $\theta = 177.5°$, which allows to access Q^2 values down to 0.4 GeV^2.

The SpaCal consists of an electromagnetic part, the eSpaCal (closer to the IP), and a hadronic part, the hSpaCal. Both follow the same setup and measurement principle. Scintillating fibers are embedded into a lead matrix parallel to the z axis. The electromagnetic (hadronic) SpaCal consists of 1180 (128) cells with a cross section perpendicular to the z

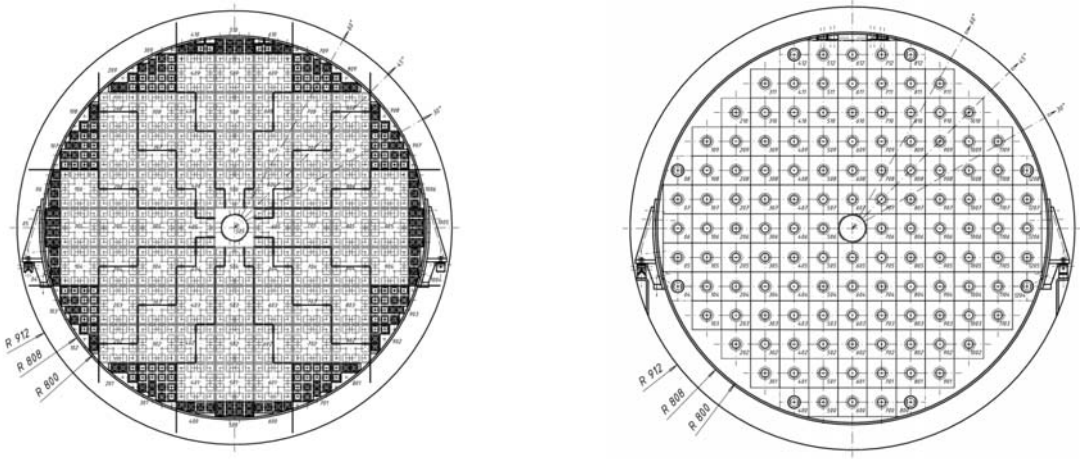

Figure 4.20.: The electromagnetic part of the SpaCal (left) and the hadronic one (right) in r-ϕ view.

axis of 40.5×40.5 mm^2 (119.3×119.3 mm^2). Each cell contains 2340 (3510) fibers of 250 mm length, 0.5 mm (1 mm) diameter. This corresponds to 27.8 (29.4) radiation lengths. The light of 2 (1) cells is mixed in a 80 mm acrylic light mixer and read out by one single photomultiplier.
This results in a energy resolution of $\sigma_E/E = (7.1 \pm 0.2)\%/\sqrt{E/GeV} \oplus (1.0 \pm 0.1)\%$ for the eSpaCal and $\sigma_E/E = (56.0 \pm 3.0)\%\sqrt{E/GeV}$ for the hSpaCal. Due to the installation of an additional beam focusing magnet in the year 2000, some cells of the SpaCal had to be removed. The angular acceptance for the data used in this analysis is by design at $\theta \leq 174.5°$ for eSpaCal and $\theta \leq 173°$. For further details on the SpaCal, see [71, 72, 73].

In addition, the SpaCal disposes of a time resolution better than 1 ns, which allows to reject upstream beam-induced background which has a time-of-flight delay of roughly 10 ns compared to regular ep events. The precise measurement of the scattered electron is vital for any DIS analysis, since the kinematics variables x, y and Q^2 depend on its energy. Hence, the errors of the electron measurement enter directly the DIS physics results. The hSpaCal which delivers a good separation of charged hadrons and electrons is used to suppress photoproduction events which build the background for DIS physics. In this analysis, the SpaCal electron identification is not used to calculate event kinematics since for $Q^2 \to 0$, the scattered electron escapes through the beam pipe.

4.7. The H1 Trigger Scheme

The purpose of the H1 trigger system [52] is to select electron-proton (ep) and to reject background events through a fast interpretation of key detector signals. Possible sources of background are:

- synchrotron radiation from the electron beam
- proton rest gas interactions in the beam pipe vacuum
- beam-wall interactions by off-orbit protons with accelerator elements like collimators or magnets
- beam halo muons from the above
- cosmic ray muons

The HERA bunch crossing rate is about 10 MHz. The overall background rate depends strongly on the machine conditions and can sum up to a rate of the order of 100 kHz. On the other hand, ep events occur roughly once in thousand bunch crossings giving an ep rate of 10 kHz. Due to the wide variety of ep processes and their cross-sections, the signal rate per process can vary from kHz for photoproduction to one event per week or month depending on the luminosity.
Currently, H1 is able to store data at a maximum rate of 30 Hz. Thus, the trigger system is designed to reduced the data rate from approximately 100 kHz to 30 Hz by rejecting the background events and prescaling ep events by their physics signal importance. At H1, the detector components deliver their measurements to create trigger signals, upon which a decision is taken automatically whether to keep the event or to discard it. Events occurring on top of the 30 Hz rate fall into the *dead time* of the detector so that H1 does not record them.

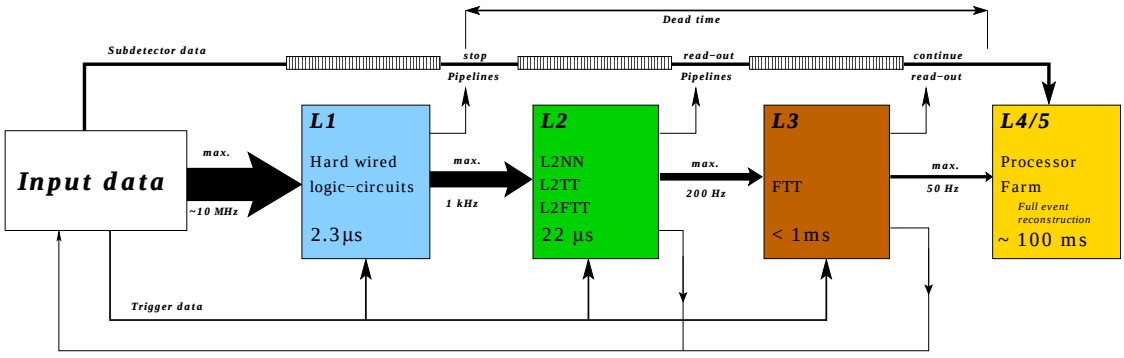

Figure 4.21.: Overview of the H1 trigger scheme.

As illustrated in fig. 4.21, the H1 trigger scheme is segmented into 4 levels.

Level 1 (L1) Here, a first trigger decision is taken in 2.3 μs. This level provides a trigger decision for each bunch crossing without causing dead time. It reduces the event rate by 5 orders of magnitude from 10 MHz to 1 kHz. For the decision, the input data from different subdetectors is encoded in 256 boolean variables referred to as trigger

elements. These variables can be combined logically to form 128 subtrigger bits. These subtriggers can be prescaled to levels at which the output does not overload bandwidth and storage capabilities. A prescale of n corresponds to one of n events being accepted by L1. After the positive decision is made, the L1 system sends a L1Keep signal to all subsystems which then keep the data of last bunch crossings stored in pipelines now coming to a halt. The dead time of H1 starts here.

Level 2 (L2) The second trigger level verifies the L1 decision based on a neural network (L2NN, [74]), topological correlations (L2TT, [75, 76]) and a fast track trigger (FTT, [77]). The L2Keep needs to be issued within 22 μs and starts the read-out of the event data from detector pipelines. This reduces the event rate from 1 kHz to 100 Hz.

Level 3 (L3) This level verifies the L2Keep based FTT. The FTT runs on a Power-PC farm where decay particles are quickly reconstructed using data from the central trackers. If L3Keep is issued, the event data is sent to Level 4 and the H1 data taking is resumed. Here the H1 dead time ends. This level further reduces the event rate from 100 Hz to 50 Hz.

Level 4 (L4) This is the level where the full event reconstruction is issued using the fortran77 software package H1REC [78]. Here, the initial calibration and alignment of all detectors is applied and an event classification is done. These events are then written to POTs (Production Output Tapes).

4.8. Track Reconstruction and Data Taking

A charged particle moving inside a magnetic field is subject to the Lorentz force and its trajectory is bent. In a homogenous solenoidal field, the trajectories of particles form a helix. Due to magnetic field inhomogeneities, multiple scattering effects[3], bremsstrahlung energy loss, track kinks due to one-prong decays[4] or wrong detector alignment, particles can deviate from ideal helix tracks.
At H1, the *dca parameterization* was chosen to reconstruct tracks. The parameters involved to fit track segments and to build a non-vertex fitted track are:

κ**, Signed Curvature** This is the signed inverse radius R of the track ($\kappa = \pm 1/R$). The sign of κ is defined by the particle track projection on the x-y plane. If the particles move counterclockwise, κ is positive and vice versa. If $\vec{p} = \vec{p}(t)$ defines the 3-momentum vector of a particle, κ writes as $(\vec{p} \times \dot{\vec{p}})_z > 0 \Leftrightarrow \kappa > 0$.

d_{ca}**, Distance of Closest Approach** This gives the signed closest distance between a track and the H1 z axis. The respective point on the track is called the d_{ca} point, having a position vector to it, $\vec{d}_{ca}$. The formal approach is $(\vec{d}_{ca} \times \vec{p}(d_{ca}))_z > 0 \Leftrightarrow d_{ca} > 0$.

z_0**,** $\vec{d}_{ca}$ **z component**

ϕ**, Azimuthal Angle** This angle is defined as for a canonical spherical coordinate system with reference to the tangent to the track projection in the x-y plane at $\vec{d}_{ca}$.

[3] particles scatter elastically from nuclei changing their direction but not their total momentum
[4] One-prong decays involve neutral decay particles, like neutrons or neutrinos, that are not recorded by the tracking detectors.

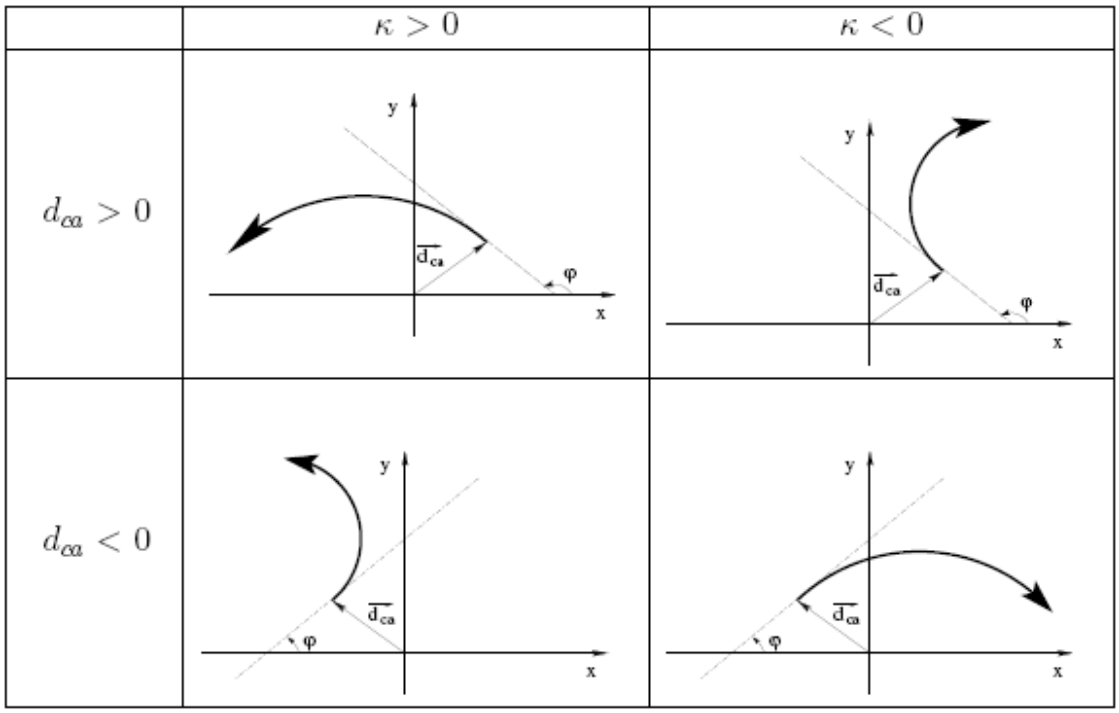

Figure 4.22.: Definitions of κ and d_ca.

θ, Polar Angle Defined by the positive z axis and the tangent to the track projection in the r-z plane at $\vec{d}_{ca}$.

With these parameters, the track properties can be calculated as a function of the integrated track length s along the helix. The coordinates of any point on the helix can be given as:

$$x(s) = x_0 + \frac{\sin(\phi + \kappa\, s)}{\kappa} \tag{4.5}$$

$$y(s) = y_0 - \frac{\cos(\phi + \kappa\, s)}{\kappa} \tag{4.6}$$

$$z(s) = z_0 + s \cdot \cot\theta \tag{4.7}$$

Where (x_0, y_0) gives the center of the circle resulting from the helix projection on the x-y plane. They can be given by

$$x_0 = -(1/\kappa - d_{ca})\, \sin\phi \tag{4.8}$$

$$y_0 = (1/\kappa - d_{ca})\, \cos\phi. \tag{4.9}$$

As equ. 4.7 refers to $z(s)$ without any dependence on the y or x coordinate, this parameterization fits well to the H1 tracking detector design, since the main track detection is delivered by a drift chamber having resolutions in x-y of 0.2 mm and in z of 2 cm which differs by two orders of magnitude, see section 4.3. The problem to measure the five helix parameters $(\kappa, d_{ca}, \phi, z_0, \theta)$ is hence decomposed into a measurement of three non-linear parameters (κ, d_{ca}, ϕ) in the x-y plane and of the linear relation, equ. 4.7, between (z_0, θ). For the circle fit in (x,y) good linearizations are used.

The 3-momentum of a particle $\vec{p}$ can thus be given by:

$$p = \sqrt{p_x^2 + p_y^2 + p_z^2} = \sqrt{p_t^2 + p_l^2} = \frac{p_t}{\sin\theta} \tag{4.10}$$

$$p_t = \sqrt{p_x^2 + p_y^2} = \frac{qB}{|\kappa|} = p\sin\theta \tag{4.11}$$

$$p_l = \frac{p_t}{tan(\theta)} = p\ \cos\theta \tag{4.12}$$

$$p_x = p_t\ \cos\theta \tag{4.13}$$

$$p_y = p_t\ \sin\theta \tag{4.14}$$

$$p_z = p_t\ \tan\theta \tag{4.15}$$

where q denotes the particle charge, B the absolute value of the magnetic field strength along the z direction and p_t (p_l) the transversal (longitudinal) component of the 3-momentum $\vec{p} = (p_x, p_y, p_z)$.
The 4-momentum vector $\mathbf{p}$ of a particle with mass m and energy E is given in the Minkowski metric by

$$E^2 = m^2 + \vec{p}^{\,2} \tag{4.16}$$

$$\mathbf{p} = (E, \vec{p}) = (E, p_x, p_y, p_z) \quad . \tag{4.17}$$

5. Event Selection and Cuts

In this analysis, two extreme kinematic and detector regions are studied, the forward and backward regions. This chapter describes how to select these regions and J/ψ events on event and track level and how to reduce the background.

5.1. Run Selection and Trigger

For this analysis, not all data taken by H1 during the 2006 and 2007 running period was chosen. FST and BST started operation on May 15th, 2006 (run number 460649) after being upgraded with radiation hard electronics. As reported in [79], the BST was not operational to full efficiency until May 27th, 2006 (run number 463266). Runs before this date were excluded from the sample used. On July 13th, 2006, HERA switched from electrons to positrons as beam leptons. This configuration was used until the end of the high energy data taking at HERA and H1 on March 26th, 2007 (run number 500611) which also marks the end of the data sample used for this analysis.

The data recorded is classified into *good, medium* or *bad* runs depending on luminosity, general detector, high voltage supply (HV) and read-out status of the detector components. Only good and medium runs are considered here. In addition a HV selection corresponding to the experimental need of this analysis was done. For preselecting events, a cut on the z vertex position $|z_{vtx}| < 30$ cm to correct for early and late satellite bunch interactions was applied. Most importantly, the L1/L2 subtrigger *s18* was used to trigger elastic J/ψ events from data. A detailed trigger setup and efficiency study will be given in section 6.6.

	2006 e^-, 2006 e^+	2007 e^+	(total $\pm$ error)
L on tape $/pb^{-1}$	93.9	43.7	137.87 ± 5.52
L forward ($pf = 1.04$) $/pb^{-1}$	90.0	43.5	133.75 ± 5.35
L backward ($pf = 1.04$) $/pb^{-1}$	87.7	43.5	131.25 ± 5.25

Table 5.1.: Summary of integrated luminosities. The errors are dominated by $\pm 4\%$ according to [80]. Given luminosities have been corrected for prescale factors.

The forward and backward luminosity referred to in table 5.1 denotes the event classification introduced in the next section.

5.2. Event classification

The leptonic decay of the J/ψ vector meson into two muons leaves a variety of detector signals in H1. The purpose of this analysis is to observe this decay using the FST or BST as track

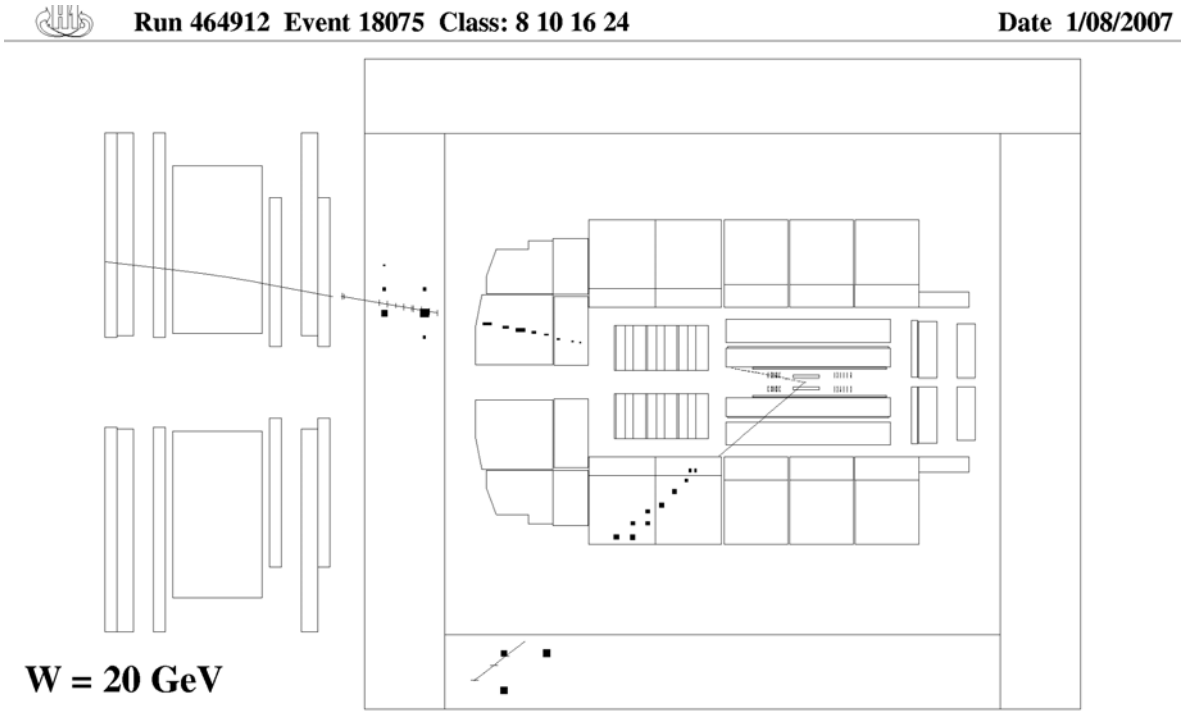

Figure 5.1.: H1 event display of a forward elastic J/ψ at a low value of $W_{\gamma p}$. The input by FST and the instrumented Iron is important.

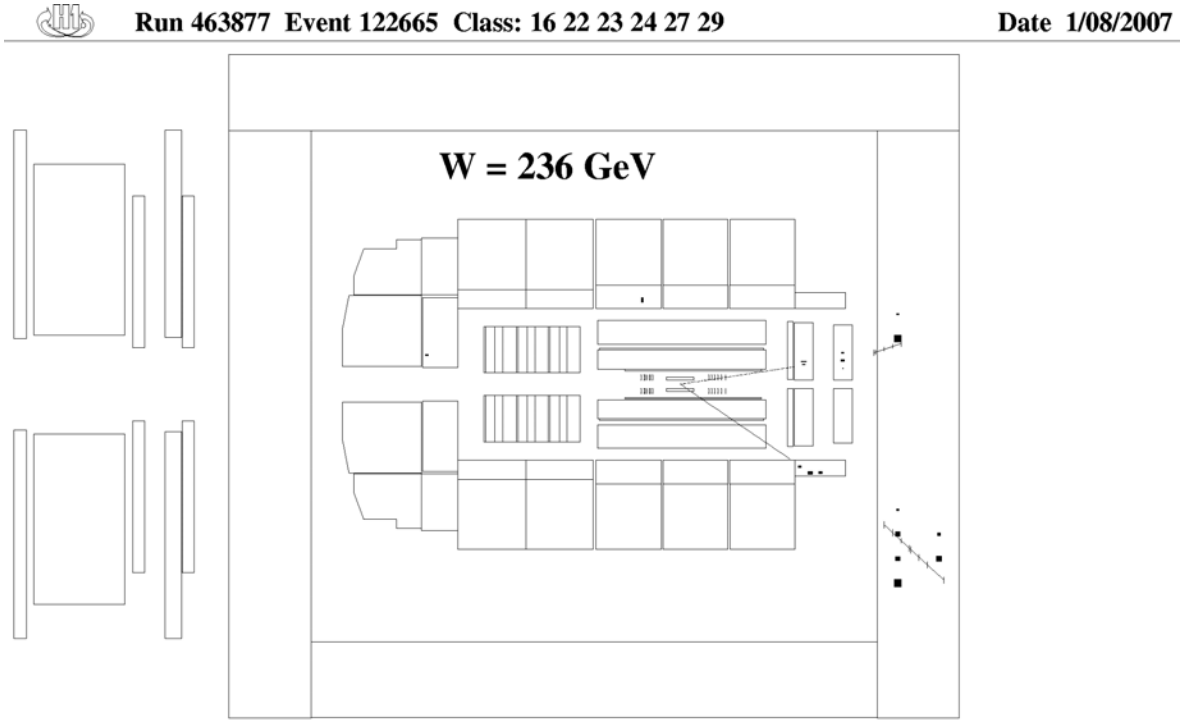

Figure 5.2.: H1 event display of a backward elastic J/ψ at a high value of $W_{\gamma p}$. The large polar angle of one track narrow opening angle indicates the importance of the BST track measurement and the SpaCal muon identification, see section 6.4.

detector for one decay muon. For this purpose, the detector signal of a J/ψ can be classified into three categories:

Forward One decay muon track is measured by the FST, the other by the central tracker CJC.

Central Both decay muon tracks are measured by the CJC.

Backward One decay muon track is measured by the BST, the other by the central tracker CJC.

To illustrate the event selection, two event displays have been chosen in fig. 5.1 and 5.1. Both illustrate the kinematic context of the event selection. The forward J/ψ sample corresponds to low values of $W_{\gamma p}$ and the backward sample to high $W_{\gamma p}$.

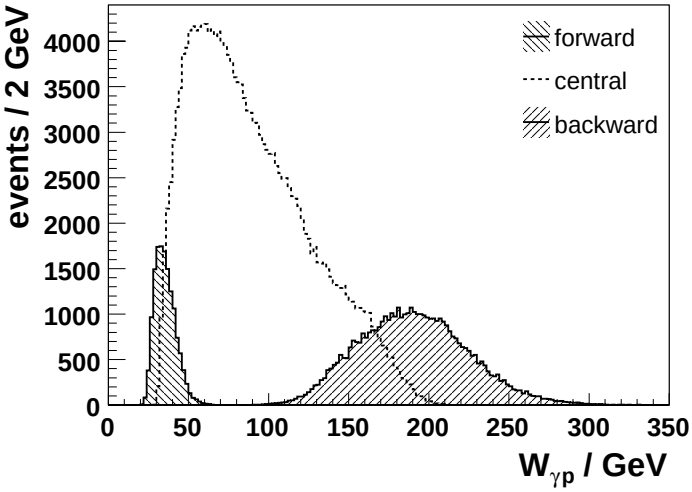

Figure 5.3.: Number of MC J/ψ events versus $W_{\gamma p}$ of the forward and backward data sample. The central sample is plotted for comparison.

The kinematic coverage of $W_{\gamma p}$ by the FST and BST is summarized in fig. 5.3.

5.3. Track Cuts

In order to extract a clear J/ψ signal and to reduce data sample size, a preselection has been performed on the H1 recorded data on tape as introduced in section 5.1. In addition to the documented cuts, the number of reconstructed central tracks during the preselection of data was restricted to "one or two". This ensures all know muon track configurations to be included. This track cut is included in the luminosity measurement.

Further, the central track is required to have $p_t > 0.8$ GeV to reduce background and to ensure that it can be detected in the LAr or the instrumented Iron respectively. It is not required to be reconstructed by the FTD since this showed medium efficiency during the data taken. The minimum criteria for tracks to be reconstructed in the central region of H1 are the *Lee-West criteria* ([81]).

Tracks from FST and BST are required to be reconstructed inside the detector acceptance which requires at least five hits. They are also required to carry $p_t > 0.8$ GeV in order to reduce background occurring close to the beam pipe.

To reconstruct the J/ψ particle from its decay leptons, the conservation of charge is used by selecting only events with two oppositely charged tracks. To conclude, the tracks were faced with various muon identification criteria which are subject of the following section. All track and identification cuts are summarized in table 5.2.

Forward	**Central**	**Backward**
1 or 2 central tracks		
$p_t > 0.8GeV$		
Both tracks from primary vertex		
$Q_{track1} * Q_{track2} < 0$		
no cosmic muons (topological)		
no cosmic muons (track timing)		
2 identified muons	2 identified muons	1 identified muon
CJC: $\mu\, Qual > 2$, $\mu\, Grade < 5$	CJC: $\mu\, Qual > 2$, $\mu\, Grade < 5$	-
FST: $\mu\, Qual > 2$	-	BST: SpaCal ID

Table 5.2.: Cuts to reconstruct $J/\psi \rightarrow \mu^+\mu^-$ vector mesons. For details on background and lepton identification see sections 5.5 and 5.4.

5.4. Decay Muon Identification

5.4.1. Central Muon ID

The central subsample created to control kinematic features of the forward and backward signal is governed by a double track muon identification. In addition to the muon quality introduced in section 4.4.3, there is another quality track feature provided by the identification algorithm of the central muon detectors.
In order to exploit the onion-like setup of H1 and the possibility of a muon track to pass both

Muon Grade	criterion
1	Inner and outer track linked with a minimum χ^2
2	Inner and outer track linked by an η - ϕ match
3	Inner track with a matching tail catcher cluster
4	Inner track with calorimeter muon data
5	Outer track

Table 5.3.: Muon Matching Grades.

muon detectors, the LAr and the instrumented Iron, matching criteria provide a measure on how well an iron track is fit to a LAr signal or a central track. All tracks involved in the latter are filtered by requiring the *Lee-West criteria*. The muon grade is a bit information translated into an integer value to cut on. It is defined in table 5.3 where "inner" and "outer" refer to Lee-West tracks detected by the CJC or LAr and in the Iron ([82]).
The central analysis reconstruction thus utilizes two tracks, both possessing a muon quality greater than 2 and a grade smaller 5, due to a wide polar angle acceptance of the first and a better momentum resolution of the latter. The need for a double muon identification can be documented by observing the signal as in fig. 5.4.

5.4.2. Forward Muon ID

In the forward data set, the same muon identification strategy as in last section is applied. Figure 5.5 shows that much more background is present for the forward direction then observed in the central sample. Forward events with two identified muons show a high signal purity and are preferred for this thesis.
The muon finder algorithm to provide muon tracks for the analysis in the central region is extended to low values of the polar angle θ by implementation of FMD tracks. Since the FST acceptance is not covered by a central muon identificator, FST tracks are matched with combined tracks from FMD, LAr and the Iron. The matching precision is presented in section 6.4.

5.4.3. Backward Muon ID

The backward analysis poses an exception in terms of muon identification. The comparison of reconstructed mass distributions from 0, 1 or 2 identified muon samples favors to ask for one identified muon by the SpaCal. The reason is the asymmetric H1 detector setup, leaving a hole in the iron behind the BST. In addition, backward events drag the central track into regions with low muon identification efficiency. This will be discussed in further detail in section 6.4.

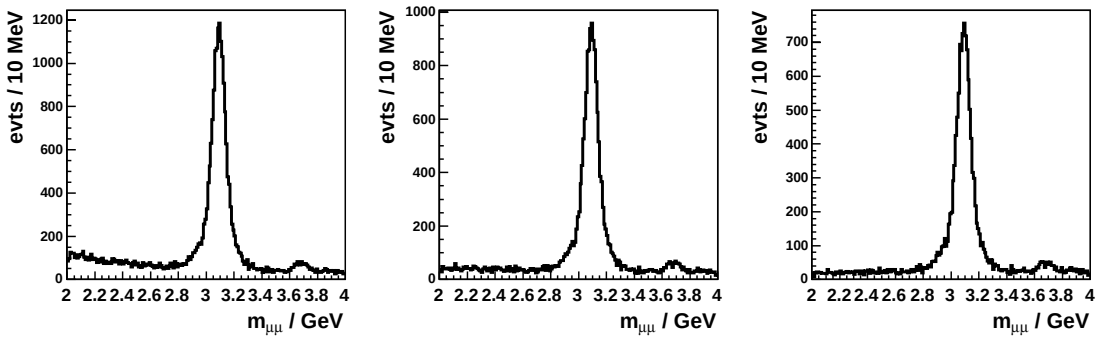

Figure 5.4.: Reconstruction of the invariant J/ψ mass with both decay muons inside the CJC acceptance. The reduction of background when demanding 0, 1, 2 (from left to right) identified muons is visible.

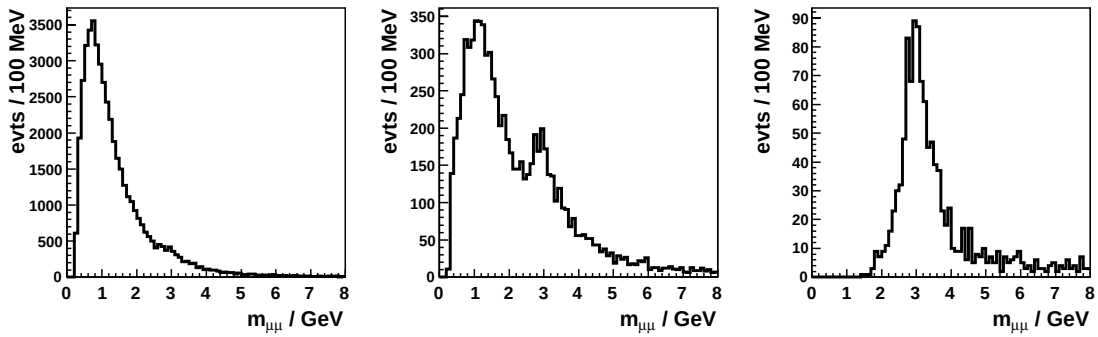

Figure 5.5.: Invariant mass distribution from forward double muonic decay events with one muon in the FST and one in the CJC acceptance. The reduction of background when demanding 0, 1, 2 (from left to right) identified muons is visible.

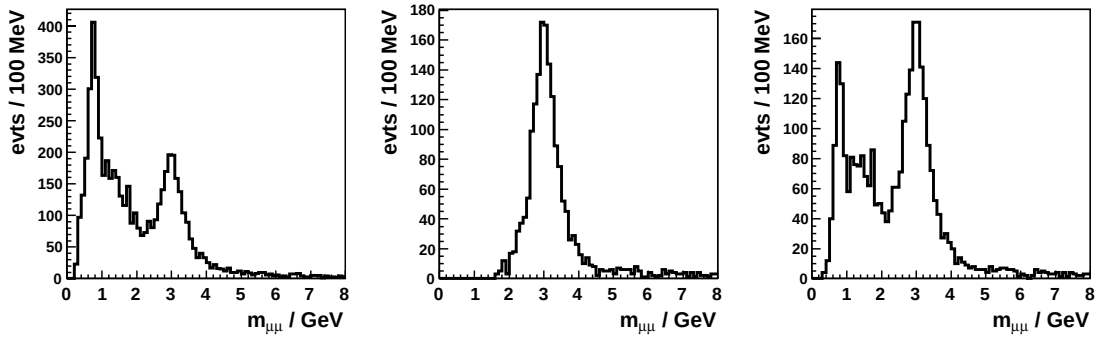

Figure 5.6.: Invariant mass distribution from backward double muonic decay events with one muon in the BST and one in the CJC acceptance. From left to right 0, 1, 2 identified muons are required.

5.5. Background Treatment

5.5.1. Resonant Background

The resonant background is a competing physical process resulting in a J/ψ signal that would pass all cuts and thus contribute to the signal. For this analysis, this background stems from $\psi(2S)$ decays. This radial excitation of the J/ψ decays in (23.0 ± 0.4) % of all cases into the J/ψ plus neutral particles ([5]) where the subsequent decay of the J/ψ can be muonic. This decay channel gives a similar detector signal than the process aimed for in this investigation. The ratio of elastic cross sections for the $\psi(2S)$ production decaying into J/ψs has been measured in [19].

$$R = \frac{\sigma_{\psi(2S)}}{\sigma_{J/\psi}} = 0.166 \pm 0.007(\text{stat.}) \pm 0.008(\text{sys.}) \pm 0.007(\text{BR})$$

This results in a total signal contribution of $(3.8 \pm 1.3)\,\%$ from $\psi(2S)$ decaying into J/ψ + neutrals. The mode $\psi(2S) \to J/\psi\,\pi^+\,\pi^-$ though showing the largest branching ratio $BR = (30.5 \pm 1.6)\,\%$ is suppressed in elastic photoproduction of J/ψ vector mesons due to the "one or two central track" cut on all events, [83].

5.5.2. Non-Resonant Background

There is also important background from cosmic ray muons, some of which are filtered by the trigger system before. To increase the purity of the data sample, additional cuts are applied.

Cosmic ray muons traveling through the H1 detector from top to bottom will be reconstructed as two tracks, showing a back-to-back topology. In addition, the timing of the upper track is early compared to the lower track, because a cosmic ray muon traverses first the upper, then the lower half of the jet chamber, while a J/ψ decaying into two muons coming from the vertex region generates two tracks with the same timing

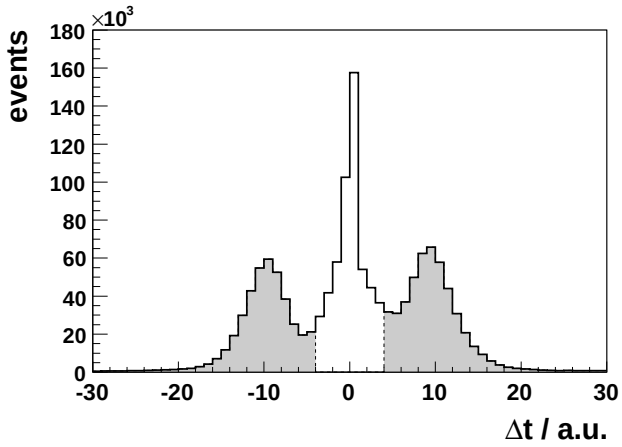

Figure 5.7.: Time difference $\Delta\,t = t_{event} - t_{CJC}$.

The common origin of cosmic ray muon tracks allows a cut on their geometric behavior. Both tracks are required to have equivalent parameters in (ϕ, θ)-space by asking that their

deviation from this hypothesis to originate from the same track is less than one sigma. A χ^2 test renders this through the ellipse parameter $R < 1$ as in

$$\sqrt{(\frac{180^\circ - \Delta\,\theta}{\sigma_\theta})^2 + (\frac{180^\circ - \Delta\,\phi}{\sigma_\phi})^2} < 1$$

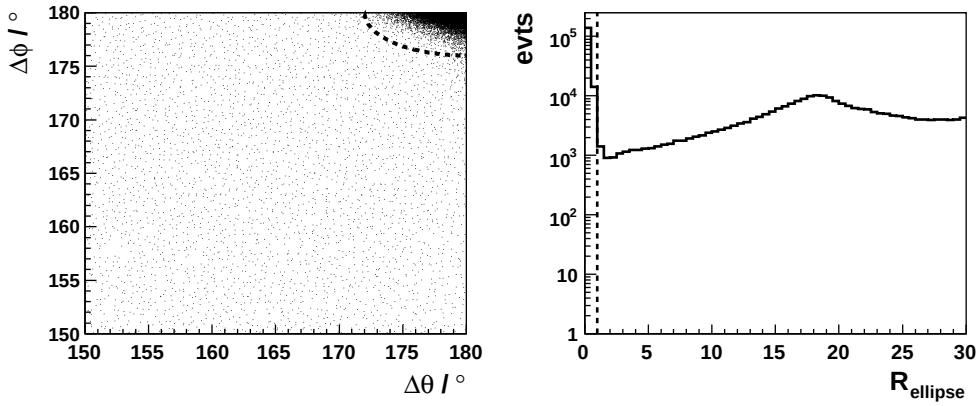

Figure 5.8.: Left: Central cosmic ray muons plotted in the ($\Delta\,\phi$, $\Delta\,\theta$) plane showing a clear accumulation of cosmic candidates near (180°, 180°) where tracks coming from a common accumulate. Right: The distribution of R in logarithmic scale. The a dashed line marks the $R = 1$ limit.

On the left hand side of fig. 5.8, the accumulation of cosmic muons near ($\Delta\,\theta = 180^\circ; \Delta\,\phi = 180^\circ$) can be observed. The introduced cut at $R = 1$ is illustrated as a dashed line in the one-dimensional and the two-dimensional histogram.
FST and BST tracks have not been subject to a cosmic muon track investigation, since cosmic rays mainly come from above. Figure 5.7 depicts the 2 local maxima outside the expected asymptotic behavior at $\Delta\,t \approx 0$. The shaded areas under the curve show the exclusion regions after a cut of $|\Delta\,t| \leq 4$ is applied. The $\Delta\,t$ and the topological method have been motivated by [84, 85].

5.6. Event Reconstruction

In photoproduction processes, the scattered beam electron is not detected by H1. It escapes through the beam pipe and cannot be used to reconstruct the event kinematics as would be done in a DIS analysis, see [21, 86]. In elastic processes, the proton also escapes through the beam pipe undetected. This leaves the two decay muons of the J/ψ vector meson as the only source for reconstructing the event kinematics. The essential variables are:

$m_{\mu^+\mu^-}$	invariant mass reconstructed from two decay muons of the J/ψ
t	the squared four-momentum transfer at the proton vertex
$W_{\gamma p}$	center-of-mass energy in the hadronic system

The double muonic invariant mass is reconstructed from the muon track four-momenta as in

$$m_{\mu^+\mu^-} = (p_{\mu^+} + p_{\mu^-})^2 \tag{5.1}$$

where p_{μ^+} and p_{μ^-} represent the track momenta as in equ. 4.17. The squared four-momentum transfer at the proton vertex t is calculated by the approximation given in equ. 3.8. For reconstructing the hadronic center-of-mass energy without information on the scattered

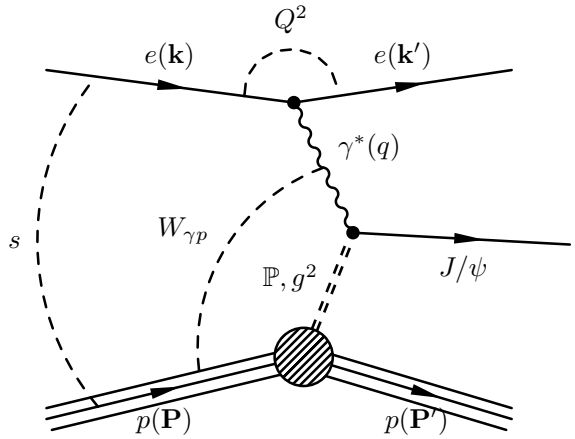

Figure 5.9.: Diagram of elastic J/ψ photoproduction and involved kinematic variables.

beam lepton, the *hadron method* or *Jaquet-Blondel method* is applied using information available from the hadronic final state, [87, 21]. For the elastic photoproduction, the hadronic final state contains only the produced J/ψ through its decay leptons. This method calculates the variable

$$\Sigma = \sum_i (E_i - p_{z,i}) \overset{here}{=} E_{J/\psi} - p_{z,J/\psi} \tag{5.2}$$

summing over all particles of the hadronic final state, here the J/ψ. Using Σ, the inelasticity y can be obtained via

$$y = \frac{\Sigma}{2E_e} \tag{5.3}$$

with E_e being the energy of the beam lepton. Using equ. 3.7, this gives

$$W^2_{\gamma p} = \frac{\Sigma}{2E_e} s + m_p^2. \tag{5.4}$$

Motivated by this method, the definition of $W^2_{\gamma p}$ was adapted to the proton vertex.

$$\begin{aligned} W^2_{\gamma p} &= (\mathbf{p_{J/\psi}} + \mathbf{p}')^2 \\ &= m^2_{J/\psi} + m_p^2 + 2\,\mathbf{p_{J/\psi}} \cdot \mathbf{p}' \\ &= m^2_{J/\psi} + m_p^2 + 2\,E_{p'}\,(E_{J/\psi} - |\vec{p_{J/\psi}}|\cos\theta_{J/\psi}) \\ &= m^2_{J/\psi} + m_p^2 + 2\,E_{p'}\,|\vec{p_{J/\psi}}|\,(\sqrt{1 + \frac{m^2_{J/\psi}}{\vec{p^2_{J/\psi}}}} - cos\theta_{J/\psi}) \end{aligned} \tag{5.5}$$

Equation 5.5 is used in this analysis to reconstruct $W_{\gamma p}$. Further, the relativistic invariant pseudo-rapidity η is reconstructed to monitor its distribution from J/ψ signals. It is calculated from the polar angle $\theta_{J/\psi}$ of the hadronic final state through

$$\eta = -\ln(\tan\theta_{J/\psi}/2). \tag{5.6}$$

5.7. J/ψ Event Cuts

In order to ensure the observation of elastic photoproduction, two approaches have been taken to select events of this production mechanism. First, DIS events have to be excluded from the data sample. Their analysis bases on the characterization of the scattered beam lepton. The SpaCal was designed to record the scattered lepton's energy and scattering angle.

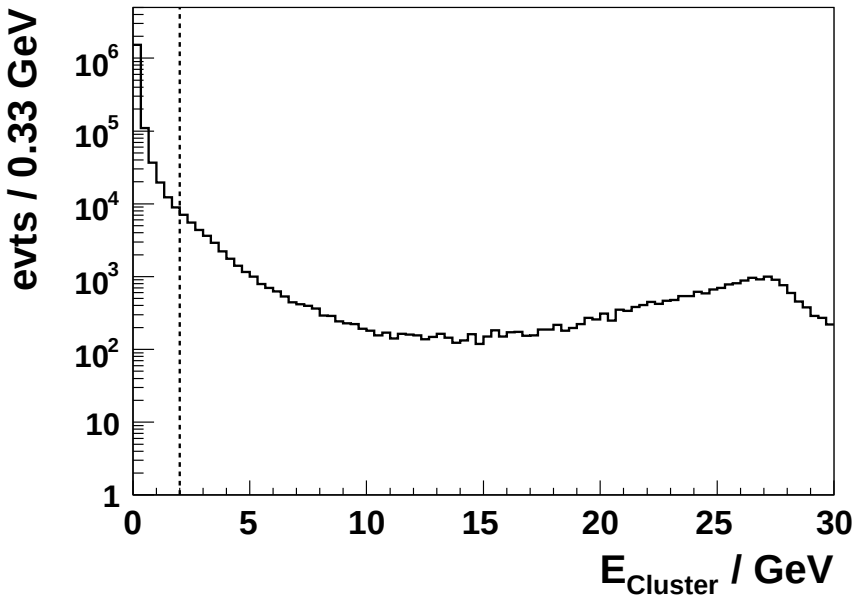

Figure 5.10.: SpaCal cluster energy distribution of all events selected by the trigger s18. The dashed line illustrates the event cut $E_{cluster} < 2$ GeV taken to select elastic processes.

The SpaCal cluster energy distribution, shown in fig. 5.10, exhibits a clear peak at the energy of the beam lepton, the kinematic peak for DIS scattering. In photoproduction however, the electron escapes H1 through the beam pipe. This motivates a cut on the cluster energy $E_{cluster} < 2$ GeV excluding most DIS events.

Elastic diffraction processes can be characterized by the 4-momentum transfer at the nucleon vertex t, equ. 3.8 and 3.9. Here, the distinction of elastic and proton dissociative processes can be investigated qualitatively. Events with $t \to 0$ are considered elastic events, others are allocated to proton dissociative processes. To ensure comparability to published H1 results, [20, 84, 85], and to suppress proton-dissociative background events, a cut on $t < 1.2$ GeV^2 was introduced.

The error on t reconstruction is measured in MC by fitting a Gaussian to the $t_{REC} - t_{GEN}$

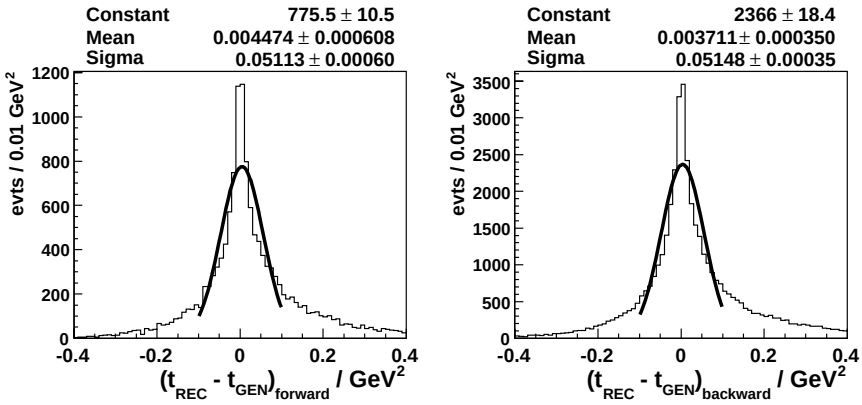

Figure 5.11.: $t_{REC} - t_{GEN}$ distributions for the forward sample (left) and the backward one (right).

distribution and computing the standard deviation $\sigma(t_{REC} - t_{GEN})$. In the following, the distribution of events as a function of t is recorded with a bin width of twice the standard deviation gathered in fig. 5.11.
Figure 5.12 exhibits the distribution of t in data and MC, whereas the full MC simulation is a mixture of a elastic and proton dissociative sample to simulate real data conditions. It is compared with a pure elastic MC sample. Data and MC show a logarithmic rise towards $t = 0$ below the chosen cut in t. This reflects their comparability.

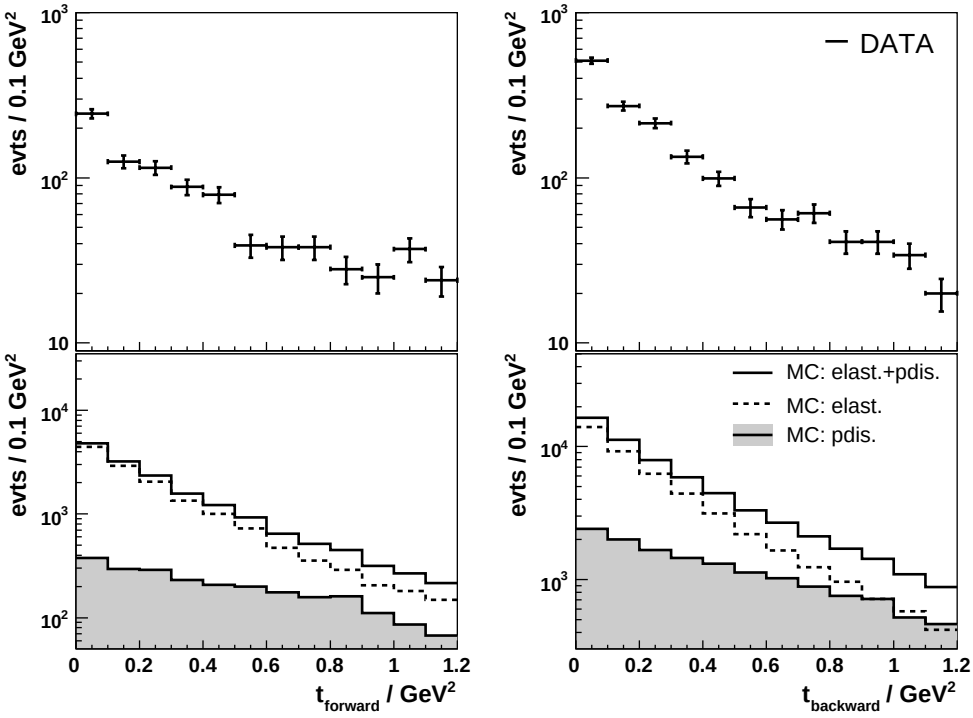

Figure 5.12.: The distribution of reconstructed J/ψ candidates from the forward sample (left) and the backward sample (right) in DATA (top) and MC (bottom) as a function of t. The dashed line illustrates the cut at $t < 1.2$ GeV^2.

6. Acceptances, Resolutions and Efficiencies

Essential ingredients for the cross section determination are geometric detector acceptances as well as reconstruction and trigger efficiencies. All of the above will be covered in the following sections by the order of sub-detectors if necessary.

6.1. Detector resolutions with MC

The track reconstruction of the decay muons is the first step in reconstructing the J/ψ signal. This analysis is done completely inside the MC framework which provides for data on the reconstruction and on the generator or simulation level, all of which have already been introduced in section 3.5. The difference between simulated and reconstructed track parameters is filled into a histogram and then fitted with a Gaussian distribution, since this is the expected error distribution of the detector reconstruction. Assuming that the MC correctly describes the detector effects, the width of this distribution is a measure of the resolution of the plotted quantity.

Figure 6.1 shows, that the central jet chambers performs with a transverse momentum resolution of $\sigma(p_t) = 24$ MeV. The relatively poor *theta* performance, $\sigma(\theta) = 11$ mrad, is caused by the bad z resolution of the CJC of the order of centimeters, stated in section 4.3, being a tribute to its design.
As one of the main trackers used to reconstruct the J/ψ signal in the forward direction, the FST shows a very good angular resolution, $\sigma(\theta) = 1$ mrad and $\sigma(\phi) = 2$ mrad in fig. 6.2. Due to the much shorter radial track length which enters the resolution quadratically, $\sigma(p_t) = 224$ MeV is 10 times worse than for the CJC.
This already outlines a major feature of reconstruction, as showed in [70], since the error by the low FST p_t resolution dominates the width of the J/ψ signal over the error by the CJC θ performance. The same is true for the J/ψ signal in backward direction recorded with the BST and CJC as in fig. 6.3.

The improvement compared to the FST is due to the additional sensor plane added in the BST. In addition to the major tracking devices, the muon identificators are also investigated upon their tracking performance.

The FMD, shown in fig. 6.4, has an intermediate momentum resolution of 164 MeV and an angular resolution at $\sigma(\phi) = 7$ mrad and $\sigma(\theta) = 11$ mrad. When combined with the overlapping central muon detectors this performance is improved as can be observed in fig. 6.5. The latter two sub-detectors are used for muon identification. Due to their good resolutions, a use as main trackers is within the reach of their capabilities.

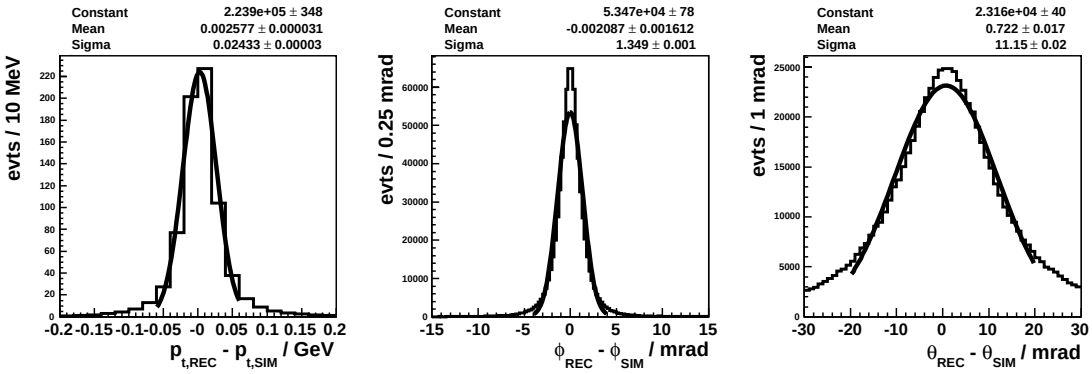

Figure 6.1.: CJC track resolution in MC in p_t, ϕ and θ.

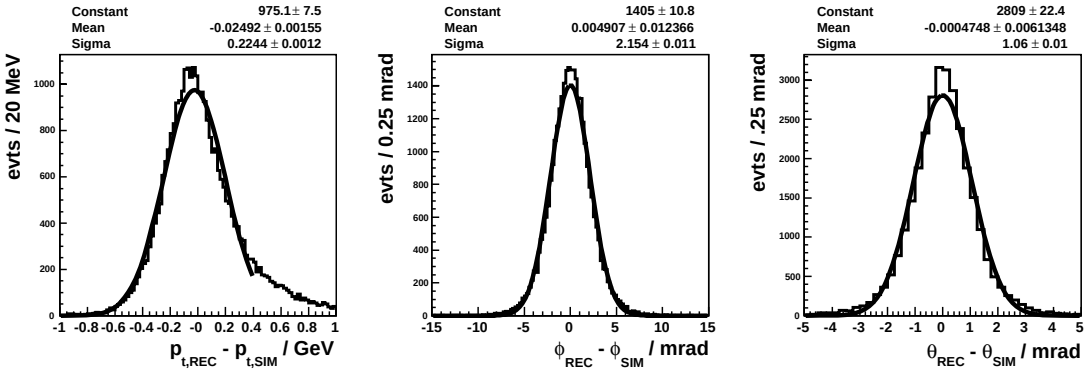

Figure 6.2.: FST track resolution in MC in p_t, ϕ and θ.

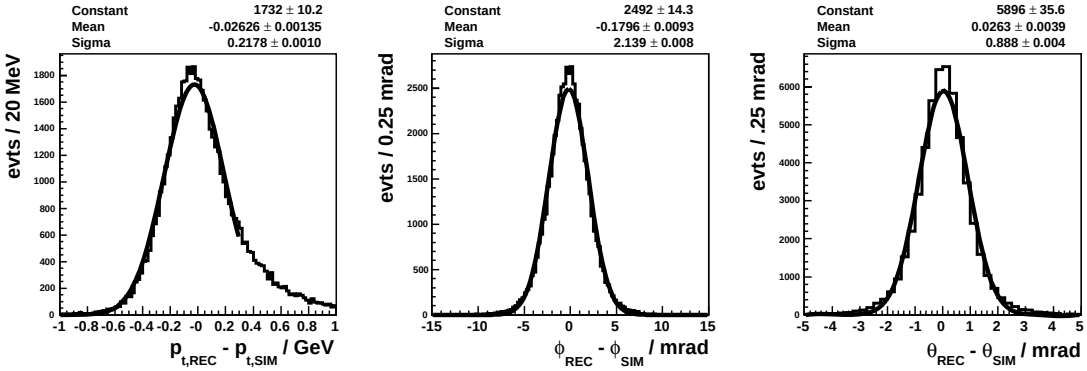

Figure 6.3.: BST track resolution in MC in p_t, ϕ and θ.

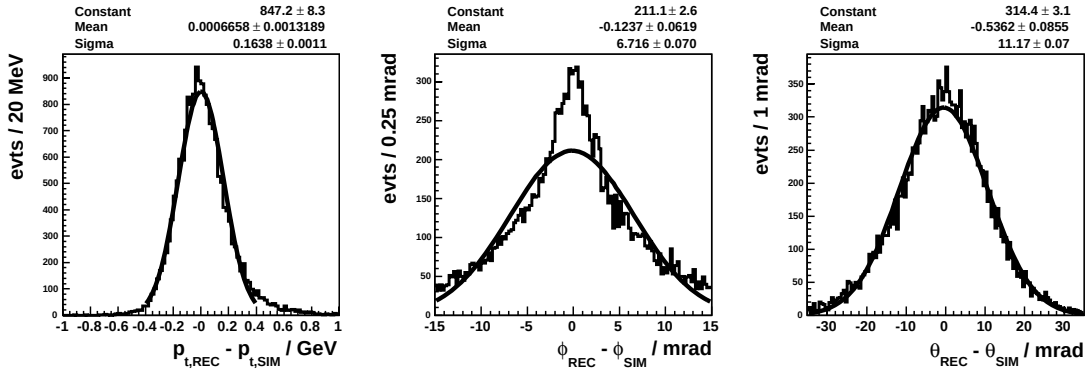

Figure 6.4.: FMD track reconstruction resolution in MC in p_t, ϕ and θ.

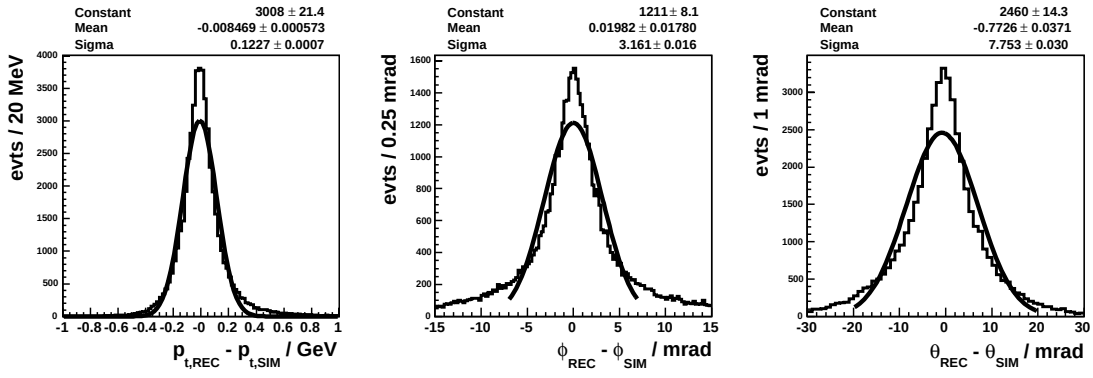

Figure 6.5.: FMD track resolution in MC in p_t, ϕ and θ.

6.2. Geometric Acceptances and Reconstruction efficiency

To understand the total acceptance of elastic J/ψ particles from decay muons in H1, the sub-detector's track acceptances give essential qualitative and quantitative information. At first, the track acceptances in θ_{track} and $p_{t,track}$ are investigated. Figure 6.6 depicts the track efficiency for the main trackers in this analysis. The CJC shows track reconstruction efficiency of more than 95% over an acceptance range $20° < \theta < 160°$. FST and BST θ_{track} efficiencies are limited to $\epsilon < 0.75$ due to a missing quadrant in ϕ as explained in sections 4.5.2 and 4.5.3.

The z smearing effect is more clearly observable in fig. 6.7. Here, the θ track histograms are compared for FST and BST with two cuts on the event vertex z-position. The acceptance for $|z_{vertex}| < 5$ cm reaches a plateau of maximal track reconstruction efficiency at 75%.

Another critical aspect of the application of MC reconstruction studies is their verification on data. This method incorporates the observation of analysis parameters on different investigative levels in MC and data, while scaling the latter to MC histogram content or luminosity. The produced distributions are called control plots. As essential track parameter, the transversal three-momentum component p_t is measured directly from the track curvature κ, see section 4.8. Figure 6.8 illustrates that MC matches the data distribution within errors. The polar angle θ is a track parameter of equal essence as p_t. Figure 6.9 shows MC and data for it under a mass cut of $m_{\mu\mu} < 4$ GeV to ensure comparability with the signal MC.

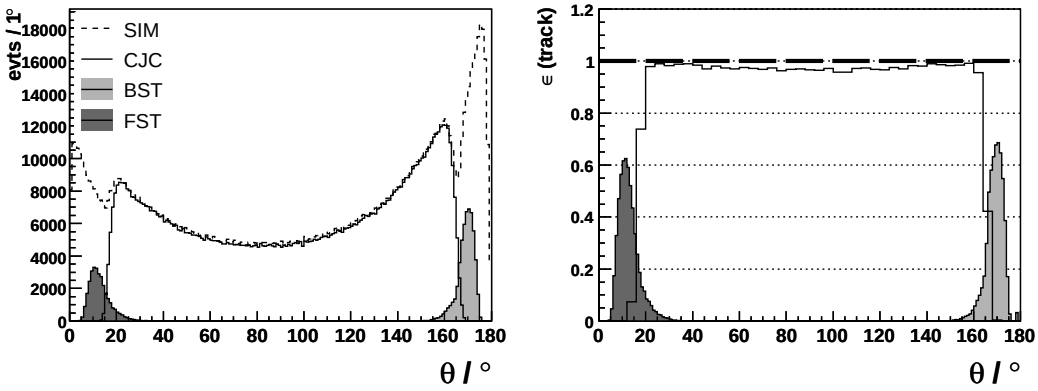

Figure 6.6.: CJC, FST and BST θ track acceptance (left) and reconstruction efficiency (right) in MC. The dashed line indicates the maximum efficiency of 75%.

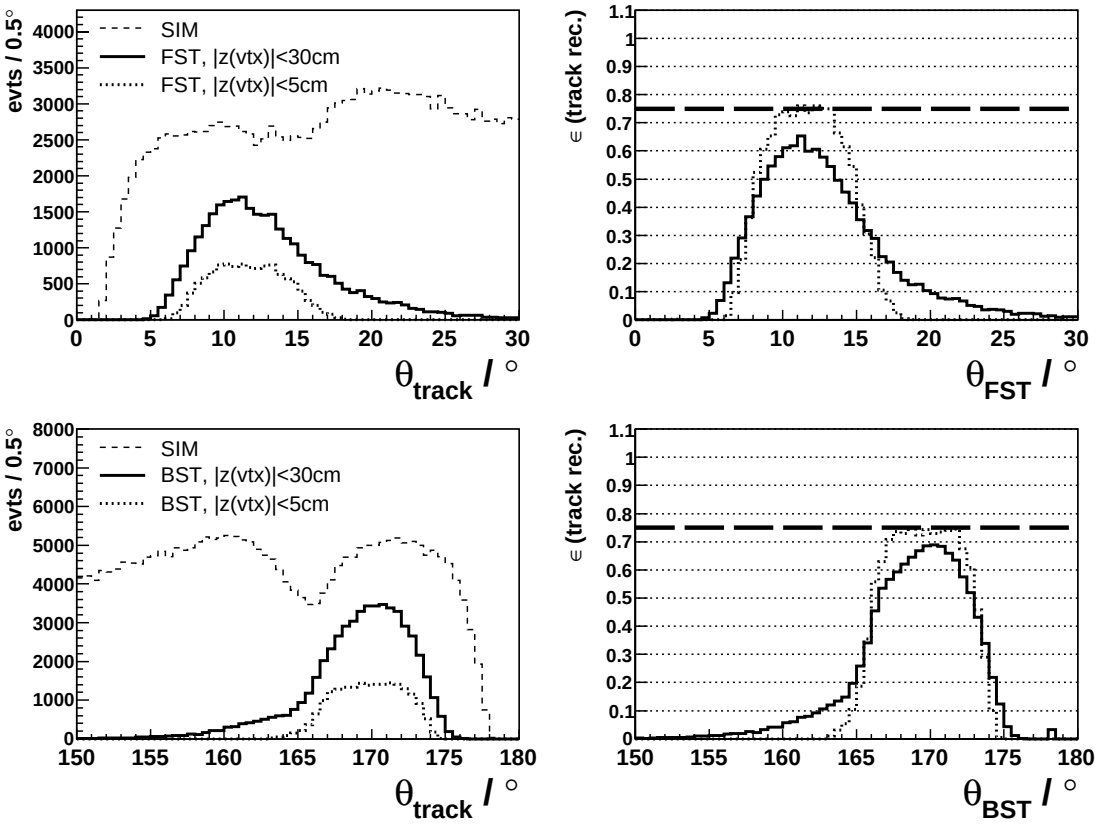

Figure 6.7.: FST and BST θ track acceptance (left) and reconstruction efficiencies (right) in MC.

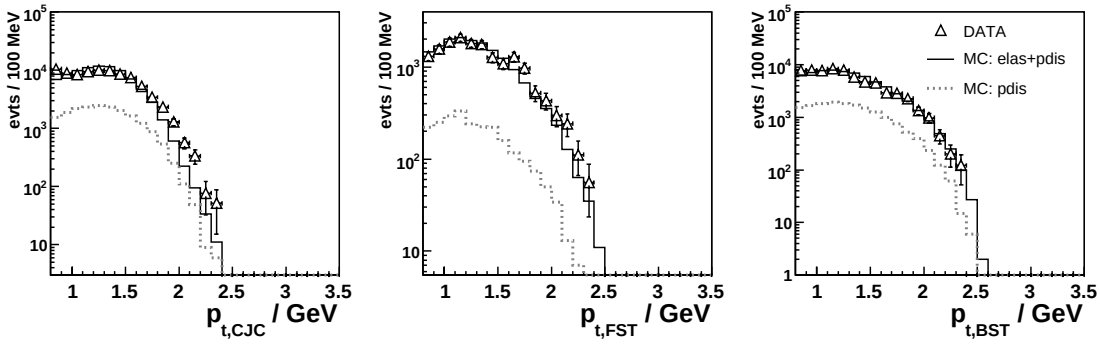

Figure 6.8.: CJC, FST and BST track p_t distribution for MC and data. For the MC, the proton dissociative background is also shown.

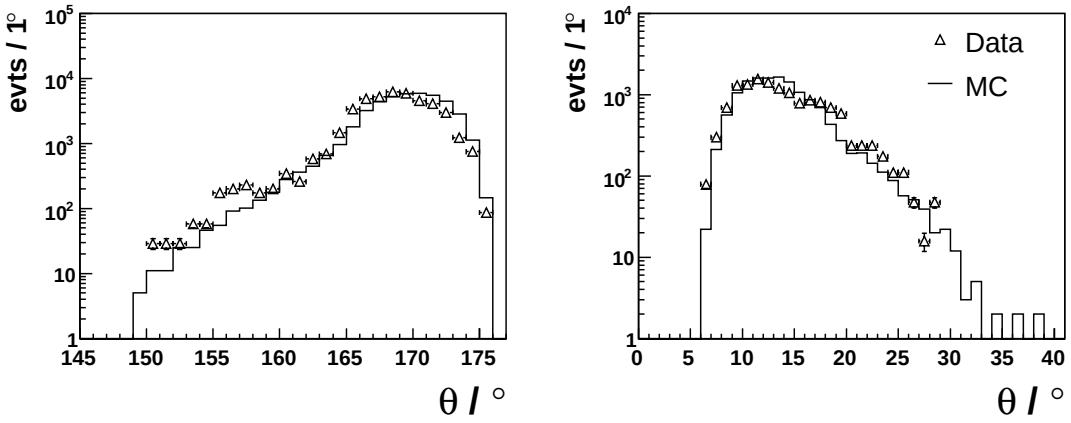

Figure 6.9.: FST(left) and BST(right) track θ control plots.

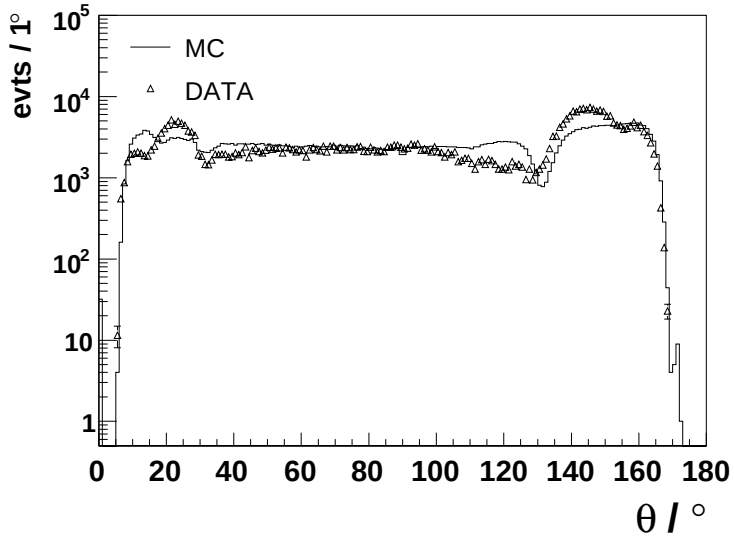

Figure 6.10.: Muon System track θ control plots.

6.3. Muon matching precision

In H1, the muon identification of CJC tracks by the central muon systems is a standard analysis algorithm also used in this study. Up to now, FST tracks have never been matched with muons reconstructed by the muon detectors. In order to achieve this, the resolutions $\Delta x = x_{MUSYS} - x_{FST}$, where x denotes a track parameter reconstructed by the muon systems $MUSYS$ or the FST have to be studied. The purpose is to mark matching criteria for both detectors.

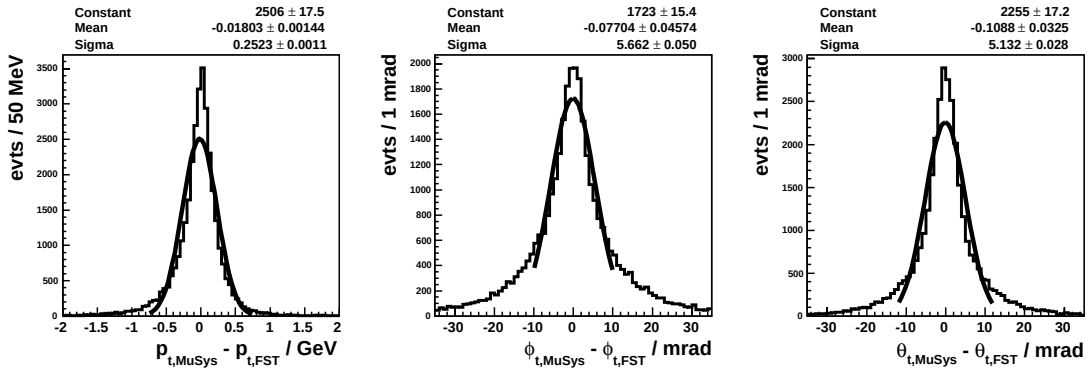

Figure 6.11.: FST track matching precision with the muon system (FMD,LAr,Iron) in MC in p_t, ϕ and θ.

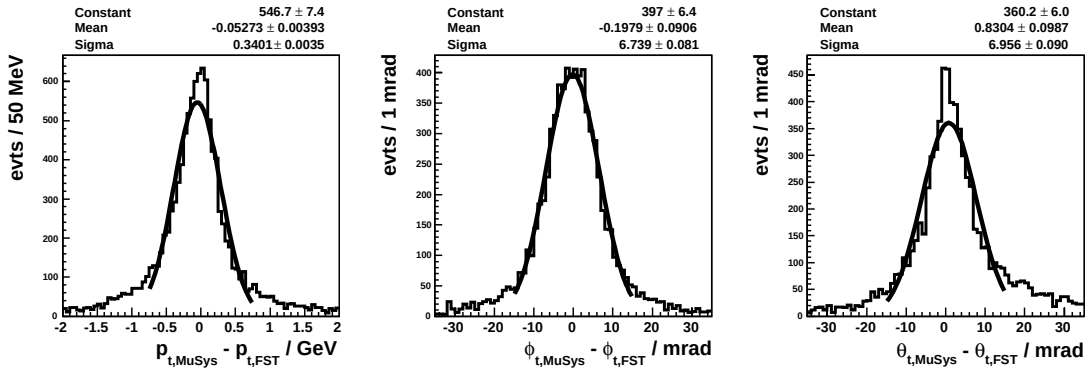

Figure 6.12.: FST track matching precision with the muon system (FMD,LAr,Iron) in DATA in p_t, ϕ and θ.

Figures 6.11 and 6.12 depict these resolutions in data and MC. A 3σ cut on both angles as matching limit was chosen. This gives an angular matching frame of $|\Delta\phi| < 25$ mrad and $|\Delta\theta| < 25$ mrad. Assuming that the matching follows a Gaussian error function, this includes most of the data illustrated in the scatter plot of the two angular track differences of fig. 6.13.

In the backward direction, a new method for identifying muons had to be introduced. As argued in section 5.4, the backward sample shows a clear rise of background when required to have a double muon identification. The SpaCal was designed for electron measurements, see section 4.6. It is implemented into MC and data with electron calibrations basing on electron clustering of violent electromagnetic showers, see [88]. The idea of calibrating

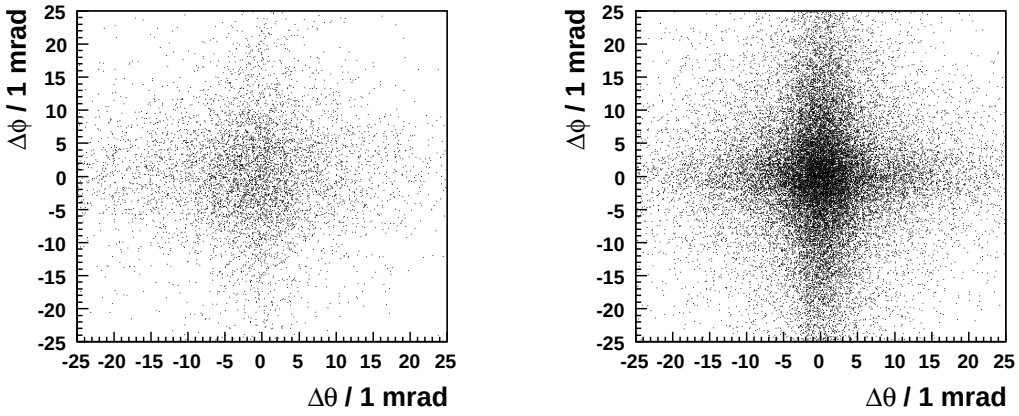

Figure 6.13.: FST-Muon System track matching in $\Delta\phi = \phi_{MUSYS} - \phi_{FST}$ versus $\Delta\theta = \theta_{MUSYS} - \theta_{FST}$ scatter plot in data (left) and MC (right). The plot limits represent the chosen matching cut.

SpaCal with muons was first introduced in [73], where a cluster energy threshold for muons was given for the eSpacal, 288 ± 37 MeV, and for the hSpacal, 323 ± 33 MeV. For the electromagnetic nature of muons and the final results of [73], the eSpaCal was hence used for muon identification. The read-out is thus restricted to uncalibrated eSpaCal clusters.

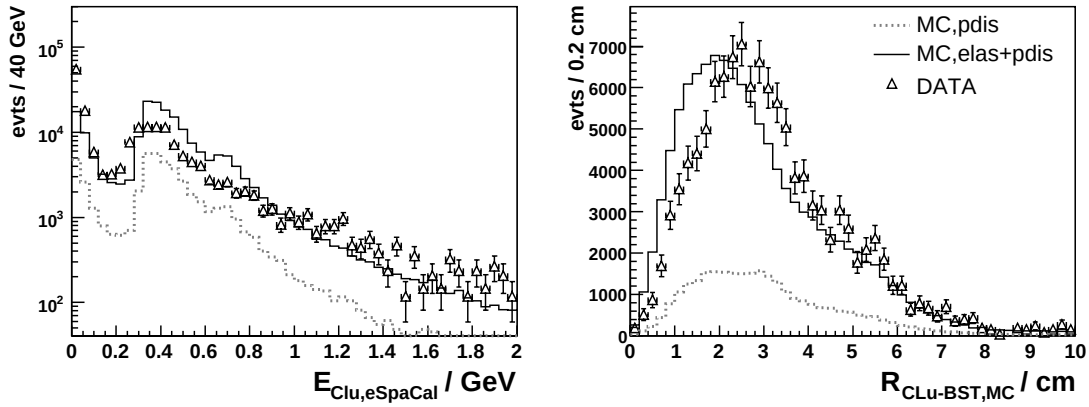

Figure 6.14.: Cluster energy (left) and SpaCal-BST radial distance distributions (right) in data and MC of 2006/2007. The difference in R is due to a misalignment of the BST versus the SpaCal in MC, [89]

Figure 6.14 shows the energy distribution of eSpaCal clusters. This exhibits a local maximum at $E_{Cluster} \approx 300$ MeV which can be identified as caused by muons. The SpaCal muon identification uses this energy disposition as upper limit. Further, a respective cluster is matched with an extrapolated BST track, which is continued into the SpaCal. Here the radial distance R of the impact point of the BST track from the barycentre, marking the center of hottest calorimetric energy disposition in the cluster, of the electromagnetic cluster is taken

as second identification limit. In reference to fig. 6.14, a BST track is identified as a muon if depositing less than 2 GeV of energy in the eSpaCal and if having $R_{BST-SpaCal} < 6$ cm. This is the first time that the SpaCal calorimeter is used as muon identificator in H1.

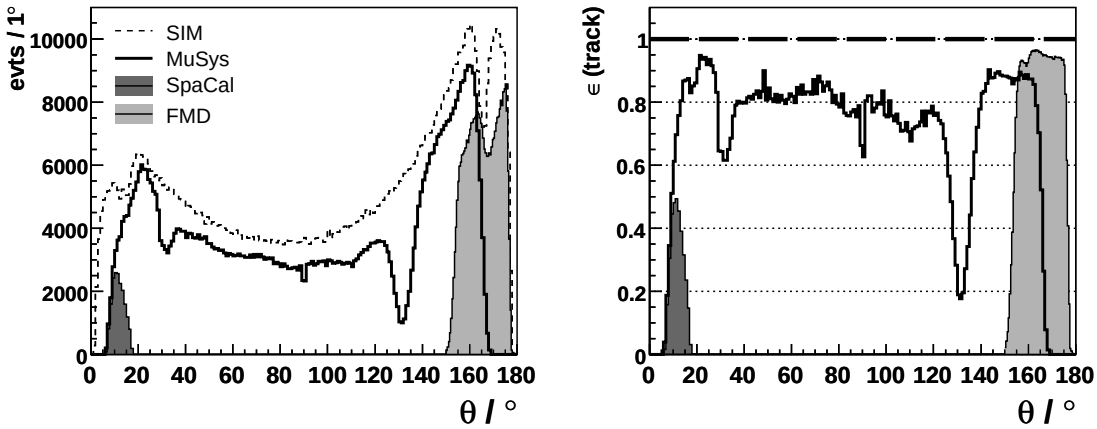

Figure 6.15.: Track θ acceptance and reconstruction efficiency of all systems used for muon identification (FMD, central muon system, SpaCal). The cracks between the barrel and endcap systems are visible at 30° and 135°.

Figure 6.15 summarizes the muon identification capabilities of H1 as used in this analysis. In the backward direction, $\theta > 150°$, the early breakdown of the central muon detectors is taken over by the SpaCal. In forward direction, $\theta < 40°$, the FMD is used with an efficiency of about 0.5. This track efficiency has been measured in data.

The FMD θ acceptance rises for low values of the polar angle to unreasonable efficiencies of 100 % in MC contradicting its polar acceptance by design, see section 4.4.2. Besides providing an object of physics investigation, the J/ψ allows detailed detector studies from data.
For this, one decay muon is measured and identified in a given detector. The remaining track, which is coupled by charge conservation and the J/ψ mass to the other, is utilized as scanning probe to study the detector response. For a given track parameter x two samples are created. One, where the desired detector response is demanded of the track and another one, where this is not done. Their ratio gives the efficiency from data.

For the case at hand, the central muon detectors were used to scan the FMD detector response. First, a J/ψ signal was reconstructed using only the central muon detectors. Here, θ was binned in 10 sections of 1.5° width. Inside each of these bins from 4.5° to 19.5° an invariant mass plot is fitted with a Gaussian function. The content of these fits is then filled into a histogram versus θ giving $N_{FMD \cup \neg FMD}$. This algorithm is repeated with an additional condition for one of the decay muons to be recorded by the FMD to give N_{FMD}.
The calculated $\epsilon = N_{FMD}/N_{FMD \cup \neg FMD}$ versus θ is illustrated in fig. 6.16. As can be seen from the plot, the resulted histogram is fitted with a polynomial of 4th order to model the analytical behavior of the detector in θ. The difference of data and MC in fig. 6.16 can be associated with a false FMD simulation in the H1SIM software package which builds an essential element of all H1 MC simulations.

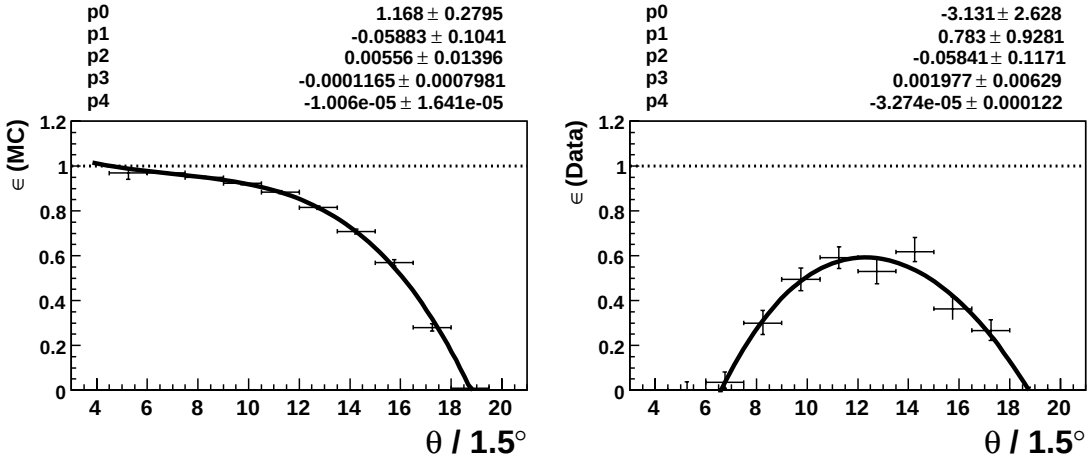

Figure 6.16.: FMD θ track efficiency for MC (left) and data (right). A polynomial of 4th order was used for fitting: $f(\theta) = p_0 + p_1 \cdot \theta + p_2 \cdot \theta^2 + p_3 \cdot \theta^3 + p_4 \cdot \theta^4$.

For this analysis, FMD tracks have been rejected in each event upon the decision of a Mersenne Twister random number generator simulating the θ polynomial fitted in fig. 6.16 when FMD tracks were provided. This reduced the false MC acceptance to the real one. For details on the Mersenne Twister generator, see [90].

6.4. Muon ID efficiency

The muon identification efficiency is calculated in the MC simulation framework. First, the forward performance is analyzed. As introduced in section 5.4, the forward sample is created by a double muon identification of the FST and the CJC track separately. The hence given efficiencies are calculated by bin-wise dividing the histograms of the reconstructed parameter x_{REC} by the simulated track parameter x_{SIM} giving a track reconstruction efficiency $\epsilon = x_{REC}/x_{SIM}$. Due to the detector resolution at mrad dimensions and the high statistics available in MC, both statistical and systematic errors are negligible.

The CJC muon identification is summarized in fig. 6.17. The given efficiency nicely underlines basic features of the H1 experiment. The dip at $\theta = 90°$ corresponds to the vertical opening shaft of the experiment. The dips at $\theta = 35°$ and $135°$ mark the edges between the barrel and endcap sections of the instrumented iron which also contain mounting shafts. The high efficient plateaus between $20 - 35°$ and $140 - 165°$ resemble the forward and backward endcap acceptances which will be of importance when studying the trigger efficiencies in the next section. Finally, the low efficiency for tracks with $\theta > 90°$ already indicates a special treatment of the backward sample.

For the forward direction, FMD tracks are added to the muon system tracks to allow a detector acceptance to low θ. This enables this combined tracker to cover the FST acceptance and thus serve as muon identification tool. Figure 6.18 (left) depicts the θ angles of FST reconstructed tracks (dotted) and muon identified FST tracks (solid). The solid line efficiency in fig. 6.18 (right) was computed as $\epsilon = N_\theta(FST, \mu\,ID)/N_\theta(FST)$ to avoid the

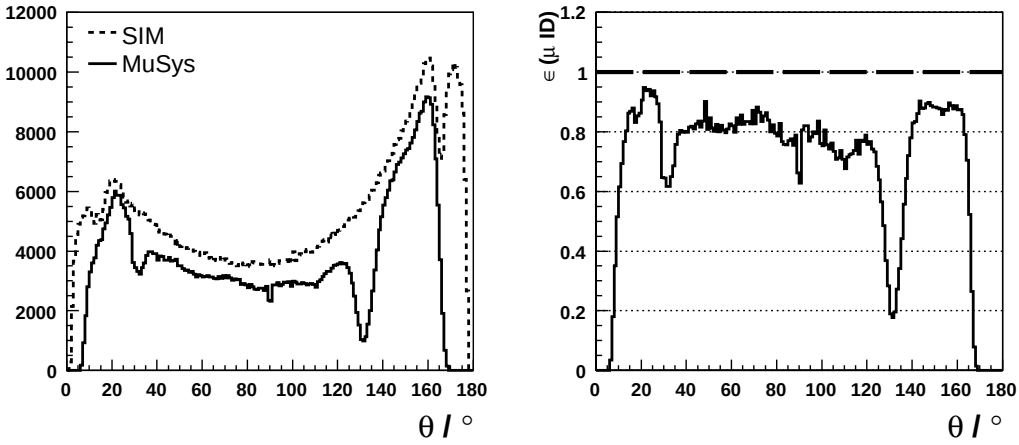

Figure 6.17.: Polar angle acceptance of the central muon system tracks used to identify CJC tracks as decay muon tracks in MC (left) and the calculated efficiency of simulated tracks (right).

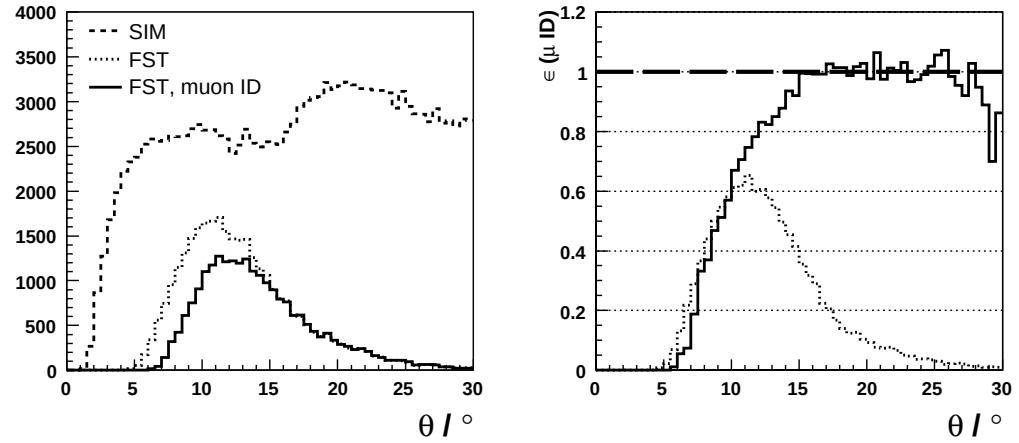

Figure 6.18.: Acceptance of the forward muon system for tracks used to identify FST tracks in MC (left) and the calculated efficiency from simulated tracks (right) as a function of the polar angle θ.

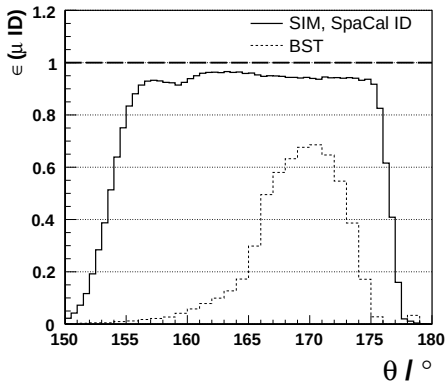

Figure 6.19.: Efficiency of simulated tracks identified as muons by the eSpaCal in MC. The BST θ track reconstruction efficiency has been overlaid for comparison as a function of the polar angle θ.

FST reconstruction performance bias. The fluctuation above the maximum value of $\epsilon = 1$ is due to smearing effects.

BST tracks have been identified with SpaCal clusters as introduced in section 6.3. The performance of this new technique is not easily described. To circumvent the bias from electron calibration in the SpaCal MC simulation, simulated tracks have been extrapolated to the eSpaCal and then fit with the muon identification limits already introduced.

Figure 6.19 shows the resulting efficiency of this method. As can be observed, the plateau with $\epsilon \approx 0.95$ covers the θ acceptance of BST tracks completely and thus gives a strong argument in favor of the SpaCal muon identification.

6.5. J/ψ reconstruction

The measurement of the cross section $\sigma(W_{\gamma p})$ is performed in intervals of the total hadronic energy $W_{\gamma p}$. The choice of these intervals in $W_{\gamma p}$, the so called *binning*, is governed by reconstruction resolution of these variables. The bin width is set to a minimum of two standard deviations of the reconstruction resolution.

Figures 6.20 and 6.21 give the reconstruction errors from the fits with a Gaussian function. For the forward sample (fig. 6.22, 6.24), the region 20 GeV $< W_{\gamma p} <$ 35 GeV has been chosen containing the maximal statistics and highest efficiency. In the backward region (fig. 6.23, 6.25), the interval 150 GeV $< W_{\gamma p} <$ 200 GeV was selected for the same reasons. The errors shown combine the statistical and systematic errors of the reconstruction efficiency quadratically. Since the MC simulation was changed significantly in this study, starting with deteriorating the FMD in forward direction and changing the BST alignment in backward direction, the simulation was varied in order to simulate the effects of these changes to the reconstruction efficiency. The resulting errors of the reconstruction efficiency $\delta\alpha_{REC} = 5-25\%$ in forward direction and 15-20 % in backward direction.

A summary of bins selected for this analysis is shown in table 6.1. The bin center of each interval was calculated from the center of gravity in each bin for MC events.

		Forward			Backward	
min. $W_{\gamma p}$	[GeV]	20	25	30	150	175
max. $W_{\gamma p}$	[GeV]	25	30	35	175	200
$< W_{\gamma p} >$	[GeV]	22.8	27.6	32.5	162.3	187.2
α_{REC}	[-]	0.012	0.092	0.144	0.20	0.294
$\delta\alpha_{REC}$	[-]	0.002	0.003	0.005	0.03	0.059

Table 6.1.: $W_{\gamma p}$ binning, reconstruction efficiency α_{REC} and its error $\delta\alpha_{REC}$.

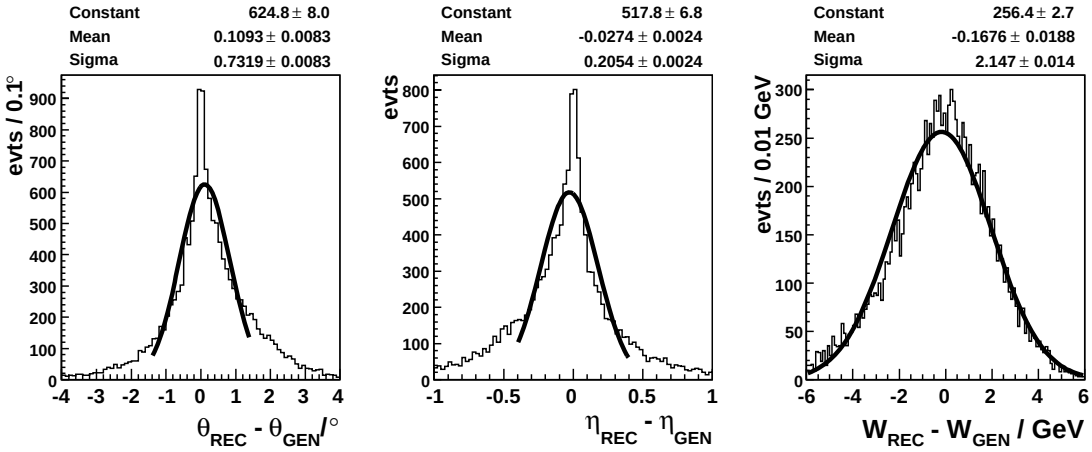

Figure 6.20.: Kinematic variable resolutions showing the $x_{REC} - x_{GEN}$ distributions for the kinematic variables $\theta_{J/\psi}, \eta, W_{\gamma p}$ in forward direction.

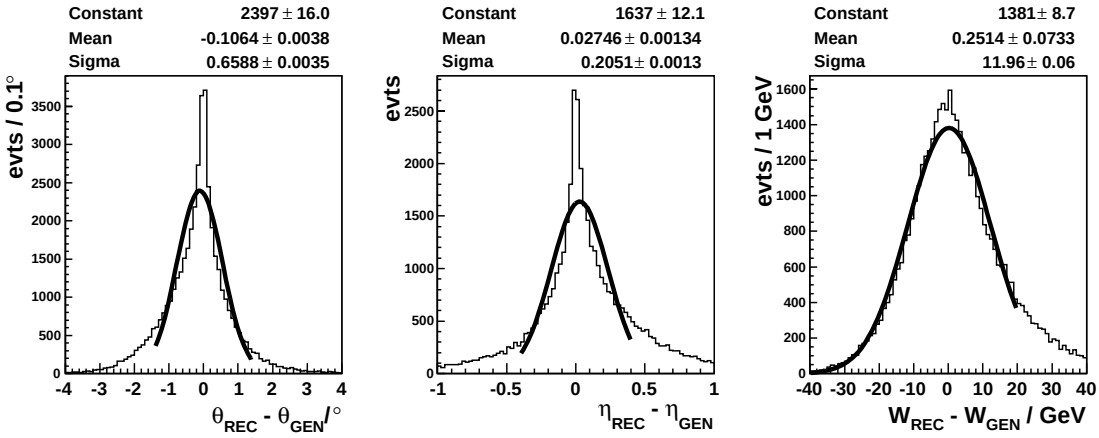

Figure 6.21.: Kinematic variable resolutions showing the $x_{REC} - x_{GEN}$ distributions for the kinematic variables $\theta_{J/\psi}, \eta, W_{\gamma p}$ in backward direction.

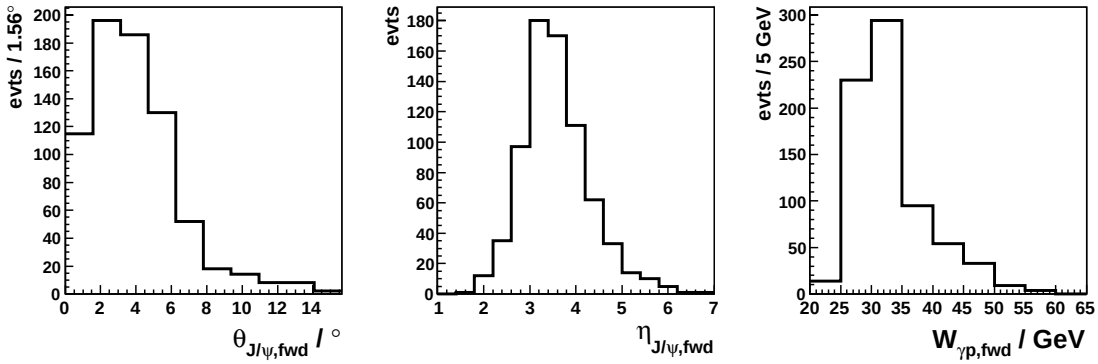

Figure 6.22.: Number of reconstructed J/ψ mesons as a function of the kinematic variables $\theta_{J/\psi}, \eta, W_{\gamma p}$ in forward direction.

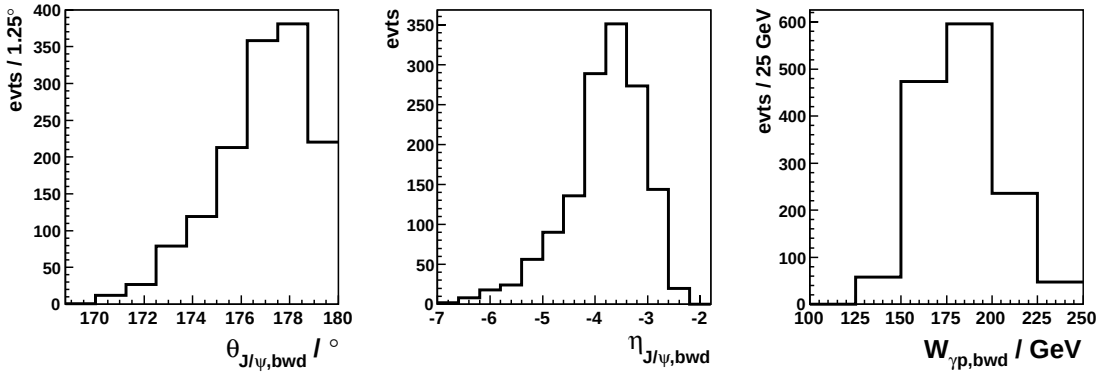

Figure 6.23.: Number of reconstructed J/ψ mesons as a function of the kinematic variables $\theta_{J/\psi}, \eta, W_{\gamma p}$ in backward direction.

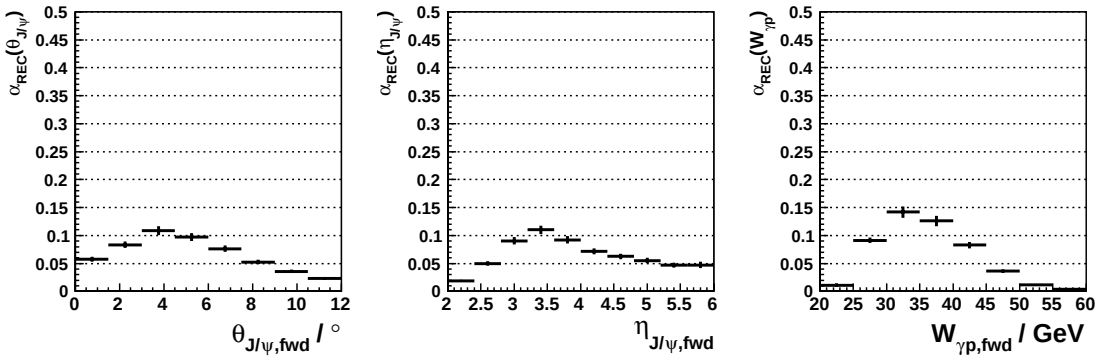

Figure 6.24.: J/ψ reconstruction efficiency in the three kinematic variables, $\theta_{J/\psi}$, $\eta_{J/\psi}$ and $W_{\gamma p}$ for the forward sample.

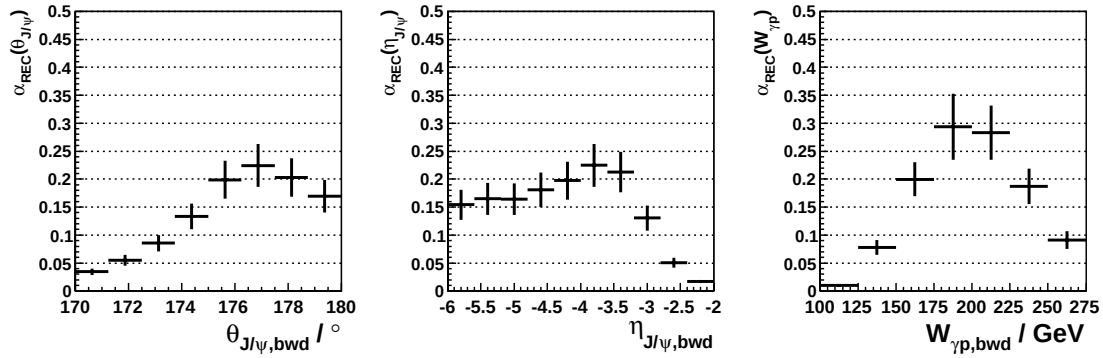

Figure 6.25.: J/ψ reconstruction efficiency in the three kinematic variables, $\theta_{J/\psi}$, $\eta_{J/\psi}$ and $W_{\gamma p}$ for the backward sample.

6.6. Trigger efficiency

The setup of the H1 trigger system has been introduced in section 4.7. For this analysis, subtrigger *s18* was used for the event preselection. This trigger has trigger level L1 and L2 subcomponents. The setup scheme can be subdivided into four sections, where all four are combined logically to give the subtrigger signal.

$$subtrigger(s18) = s18Track \cap s18Muons \cap s18Background \cap s18L2 \tag{6.1}$$

All elements $s18Track$, $s18Muons$ and $s18Background$ work on L1 and $s18L2$ on trigger level 2. All subtrigger components are made from a logical conjunction of trigger elements corresponding to detector signals provided by H1 for every event. For a detailed understanding of the s18 performance, an investigation of all subtrigger elements is needed.

$$\begin{aligned}
s18Track &= (FTT_mul_Td > 0) \cap (CIP_mul < 6) \cap (FTT_mul_Ta < 7) \\
s18Muons &= (MU_Bar) \cup (Mu_ECQ) \\
s18Background &= \neg(SPCLh_AToF_E_1) \cap \neg(VETO_BG) \cap \neg(SToF_BG) \\
&\quad \cap (\neg(BToF_BG) \cap BToF_Gl \cap \neg(BToF_IA)) \cap (FIT_IA \cup \neg(FIT_BG) \\
&\quad \cap \neg(SPCLe_AToF_E_1) \cap (CIP_T0 \cap (CIP_sig > 0)) \\
s18L2 &= L2 : s81(FTT)
\end{aligned}$$

In nuce, only the essential trigger elements shall be described here. For more details, see [85, 57, 77, 91].

FTT The Fast Track Trigger (FTT) allows to reconstruct three-dimensional tracks in the central drift chamber down to a transverse momentum of 100 MeV/c within a time window of $\tilde{2}3$ μs. FTT_mul trigger elements give track multiplicities in central H1 at various transversal momentum thresholds. For FTT_mul_Ta, all tracks with $p_t > 100$ MeV are counted and FTT_mul_Td works on a limit of $p_t > 900$ MeV. L2:s81(FTT) contains only the FTT trigger bit 'FTT_Tc_gt_0' corresponding to the number of tracks with a transversal momentum of $p_t > 416$ MeV.

CIP The CIP trigger bits provide trigger bits corresponding to CIP measurements. CIP_mul corresponds to the number of tracks allocated to CIP signals in the forward, backward and central H1 detector without any limits on track parameters.

Muon System The muon systems, i.e. the instrumented iron, provides a trigger signal when recording muons in the endcap, Mu_ECQ, or in the barrel region, Mu_Bar. The trigger uses five layers of the CMD (3, 4, 5, 8, 12), see section 4.4. In the barrel (Mu_bar) two out of the innermost four trigger layers are required. Mu_ECQ represents the logic junction of $Mu\_FOEC \cup Mu\_BOEC \cap Mu\_BIEC$ requiring three out of five layers in the detector component to signal. Note, the forward inner endcap trigger element is not included [91].

The method to analyze the trigger efficiencies was taken as follows. The data was selected without a subtrigger requested, but with the offline reconstruction using instrumented Iron, LAr and FMD signals to give a minimum of one muon track per event. This created a statistically monitor subsample of events since the offline muon reconstruction requires at

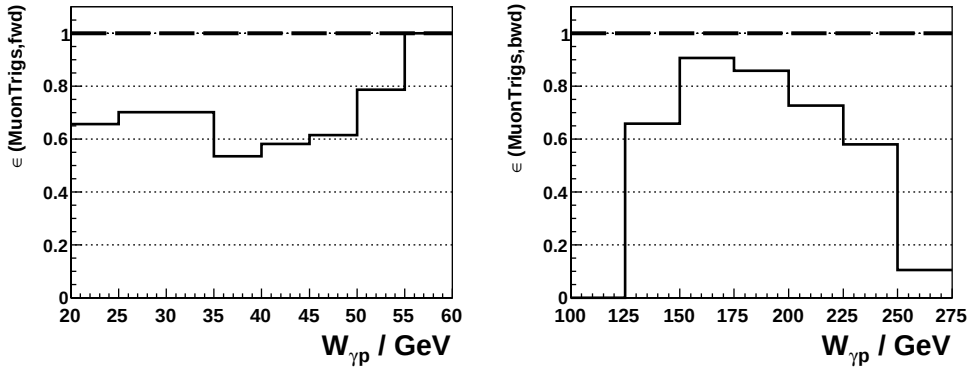

Figure 6.26.: Muon system trigger efficiency in s18, forward (left) and backward (right)

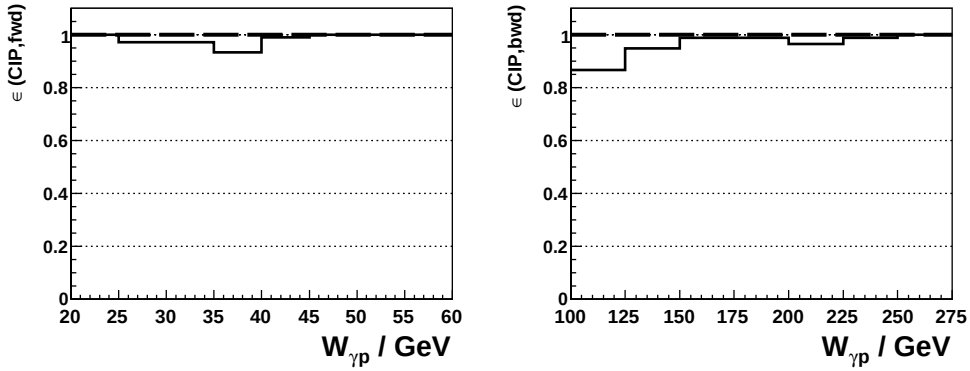

Figure 6.27.: CIP trigger efficiency in s18, forward (left) and backward (right).

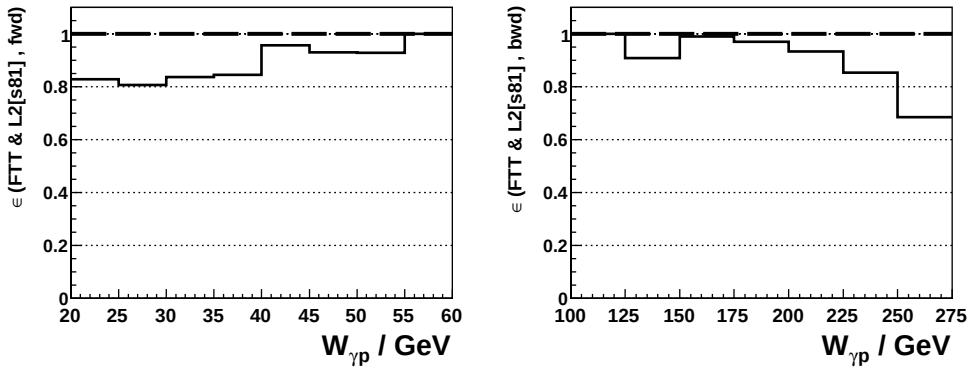

Figure 6.28.: FTT on L1 and FTT L2 subtrigger 81 efficiency in s18, forward (left) and backward (right).

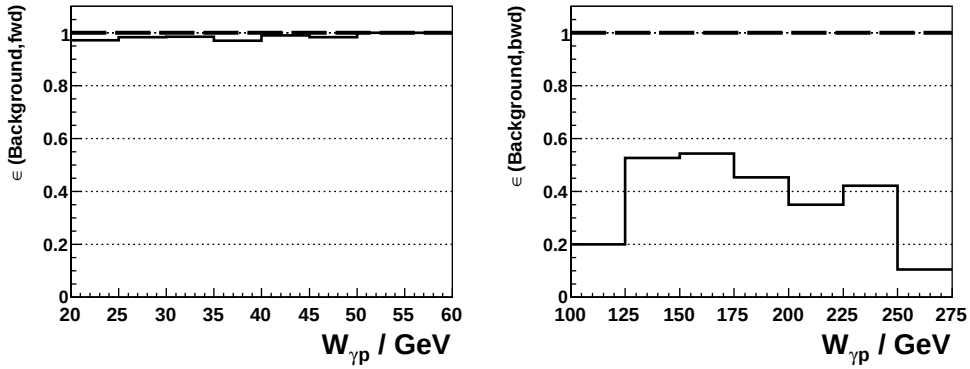

Figure 6.29.: Background trigger elements efficiency in s18, forward (left) and backward (right).

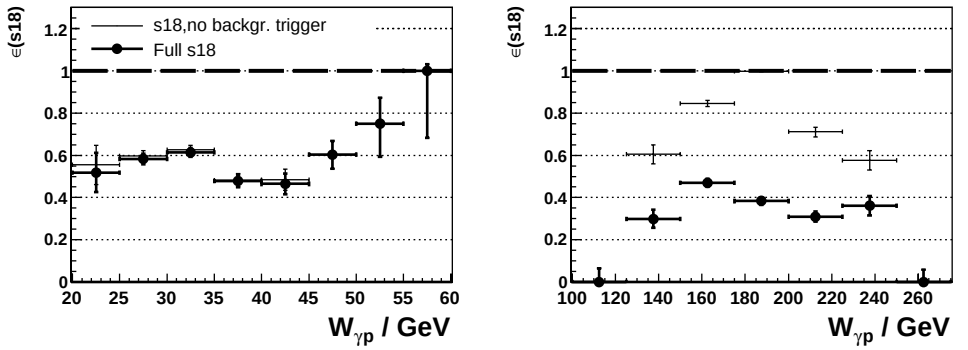

Figure 6.30.: Total trigger efficiency of s18, forward (left) and backward (right).

least good muon quality in the LAr and instrumented Iron to output a muon track, ([82]). This demands a minimum energy of the muon track of 1.2 GeV and a muon quality greater two. The L1 CMD trigger elements require a track energy of at least 2 GeV. They represent a measurement by the drift chamber layers in the instrumented Iron. Hence, the offline selection created a monitor sample for events triggered by *s18*. Upon this, the J/ψ events were counted within a 2σ cut on the invariant mass of the two decay leptons.

For every trigger element TE, the trigger efficiency ϵ_{trig} was calculated from

$$\epsilon_{trig} = \frac{N(\text{Offline} \cap TE)}{N(\text{Offline})} \tag{6.2}$$

where $N(\text{Offline} \cap TE)$ denotes all entries in a bin of the kinematic variable observed which were made with the respective trigger element and the offline muon reconstruction to give a positive bit and $N(\text{Offline})$ when only the offline reconstruction gave a result. Figures 6.26 to 6.29 illustrate the trigger element efficiencies that logically build the s18 subtrigger. Errors are not given due to the descriptive character of these plots. They were studied to understand the substructure of the s18 setup.

The muon system exhibits a rise towards 100 % performance, although the acceptance of the FST-CJC is decreasing for $W_{\gamma p} > 45$ GeV. This indicates smearing effects. The CIP trigger efficiency, fig. 6.27, shows a good performance throughout the kinematic interval observed. The FTT histogram, fig. 6.28, depicts an decrease in efficiency towards the high and low $W_{\gamma p}$ limits, because the opening angle of the decay leptons decreases with very high or low $W_{\gamma p}$. This drags the central muon track towards the limits of the FTT acceptance resulting in a lower trigger efficiency. The background suppressing trigger elements show a clear inefficiency in the backward data set. The reason for this is still not understood and may be caused by the DIS motivated setup, i.e. suppressing low energy depositions in the SpaCal.

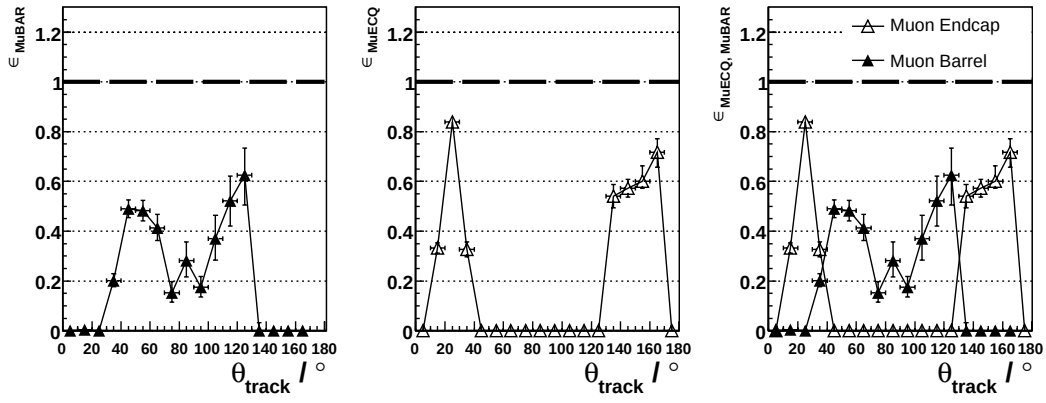

Figure 6.31.: Trigger element track reconstruction efficiency, muon barrel (left), endcap (middle) and both for comparison (right).

The total trigger efficiency for the s18 was finally measured by filling invariant mass histograms in bins of $W_{\gamma p}$. The resulting mass distributions were fit with a Gaussian

function. The contents of these fits were used as input for equ. 6.2. The fit errors and the resulting division according to Bayes statistics, [92], are taken into account.

Figure 6.30 illustrates the low performance of background suppressing trigger elements for the backward sample. The overall result is expected, from the low stability of the barrel and endcap muon detectors. They have been subject of an independent acceptance and reconstruction efficiency investigation.
The method used equals the one used for recording the FMD acceptance in θ_{track} in section 6.3, see fig. 6.16.

The results of this study, fig. 6.31, show the performance of the forward and backward muon endcap within their acceptance at $20° < \theta_{track} < 45°$ and $125° < \theta_{track} < 175°$. The barrel muon detectors show a medium performance averaging at 60 % over a wide range in its polar acceptance. Combining this observation with the FTT tracking trigger elements results in a efficiency below 0.6. It is this interplay between muon trigger elements, foremost the muon endcap triggers, and the FTT, which is limited to the central tracker acceptance, that allows for high and low $W_{\gamma p}$ measurements on the muon side.

7. Signal and Cross Section Determination

Finally, the J/ψ signals are extracted from the data and fitted with a background contribution in bins of the kinematic variables. The cross section is calculated as a function of the invariant hadronic center-of-mass energy $W_{\gamma p}$ taking into account efficiencies, acceptances and their errors. This measurement is compared with earlier measurements at HERA.

7.1. Cross Section Determination

7.1.1. The Cross Section

The cross section for elastic J/ψ photoproduction $ep \to epJ/\psi$ ([20]) in the electron-proton system as observed by the H1 detector is calculated as

$$\sigma(ep \to epJ/\psi) = \frac{N_{signal} \cdot (1 - f_{\psi(2S)}) f_{elas}}{\alpha_{REC} \cdot \epsilon_{trig} \cdot L \cdot BR}. \tag{7.1}$$

Here, N_{signal} gives the fitted number of J/ψ events for the given data sample. $f_{\psi(2S)}$ denotes the correction factor for background events caused by the $\psi(2S)$ decay mode $\psi(2S) \to J/\psi$+neutral particles. f_{elas} is the correction for elastic diffraction in a data sample containing also proton-dissociative background events, see section 5.5.1.

As in sections 6.5 and 6.6, α_{REC} and ϵ_{trig} refer to the J/ψ reconstruction efficiency and the trigger efficiency used, $BR = (0.0593 \pm 0.0006)$ ([5]) notes the branching ratio of the double leptonic J/ψ decay into two muons. L gives the total integrated luminosity for the used data sample as in table 5.1. The cross section is determined in each $W_{\gamma p}$ interval independently. The result of this calculation is attributed to the center of each $W_{\gamma p}$ bin, as given in table 6.1.

The cross section measurement in the electron-proton system is normalized to the photon flux due to its production mechanism and in order to compare it with published results of other experiments.

7.1.2. Photon Flux Determination

The normalization of the electron-proton cross section to the photon-proton system, see section 3.3.4, is given by

$$\sigma(\gamma p \to J/\psi\, p) = \frac{\sigma(ep \to e\, J/\psi\, p)}{\Phi_\gamma} \tag{7.2}$$

where Φ_γ denotes the integrated photon flux in the observed $W_{\gamma p}$ bin. This is an approximation using the Weizsäcker Williams Approximation ([93, 94]), where the Born cross section is treated as

$$\frac{d\sigma_{ep}(y,Q^2)}{dy\ dQ^2} = \Phi_\gamma^T \sigma_{\gamma^* p}. \tag{7.3}$$

Φ_γ^T denotes the transversely polarized virtual photon flux as in

$$\Phi_\gamma^T = \frac{\alpha_{QED}}{2\pi\ y\ Q^2}(1+(1-y)^2 - 2m_e^2\ \frac{y^2}{Q^2}). \tag{7.4}$$

Integration over the inelasticity y and the virtuality Q^2 leads to

$$\sigma_{ep} = \int_{y_{min}}^{y_{max}} dy\ \int_{Q^2_{min}}^{Q^2_{max}} dQ^2\ \Phi_\gamma^T(y,Q^2)\ \sigma_{\gamma^* p}(y,Q^2). \tag{7.5}$$

The minimum required Q^2 due to the event kinematics is given by $Q^2_{min} = m_e^2\, y^2/(1-y)$. Using the relation between y and $W_{\gamma p}$, equ. 3.7, this gives

$$\Phi_\gamma = \int_{W_{min}}^{W_{max}} dW\ \int_{Q^2_{min}}^{Q^2_{max}} dQ^2\ \Phi_\gamma^T(W,Q^2) \tag{7.6}$$

for a point (W_0, Q_0^2) in phase space. This point can be defined as

$$\Phi_\gamma = \int_{W_{min}}^{W_{max}} dW\ \int_{Q^2_{min}}^{Q^2_{max}} dQ^2\ \Phi_\gamma^T(W,Q^2)(\frac{W}{W_0})^\delta(\frac{M^2_{J/\psi}+Q_0^2}{M^2_{J/\psi}+Q^2})^{-n} \tag{7.7}$$

under the assumption $\sigma_{\gamma^* p} \propto \frac{W^\delta}{(M^2_{J/\psi}+Q^2)^{-n}}$.

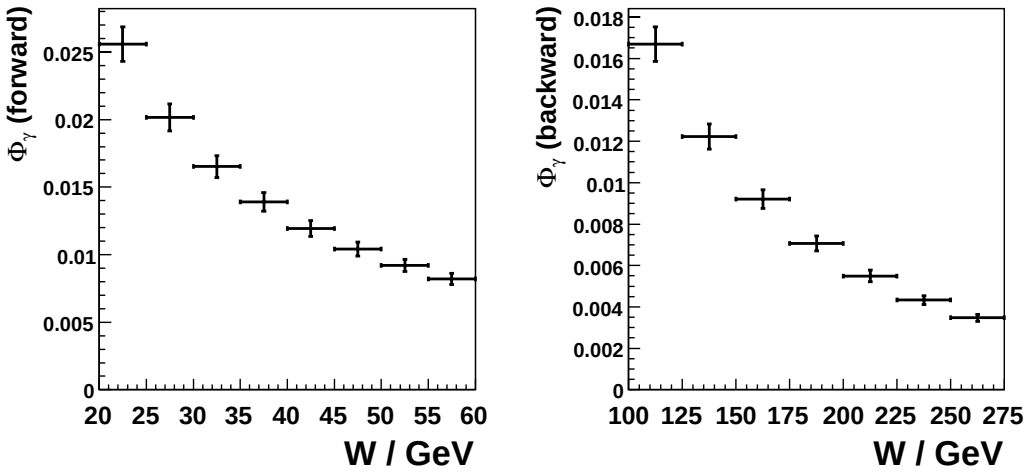

Figure 7.1.: Photon Flux Φ_γ calculated for the forward (left) and backward sample (right).

The photon flux was calculated by numerical calculation over all observed $W_{\gamma p}$ bins according to equ. 7.6. Figure 7.1 depicts the result.

7.2. Signal Extraction

7.2.1. The J/ψ Signal from H1 Data in 2006 and 2007

At first, the total J/ψ signal is extracted from the data and fitted with a Gaussian function to retrieve the signal width and the number of J/ψ events.

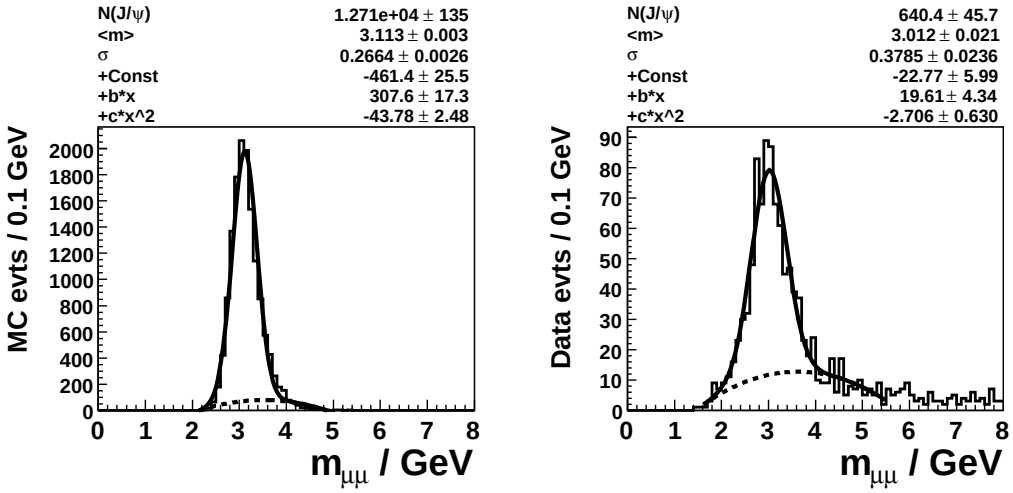

Figure 7.2.: Forward invariant mass distribution for data and MC.

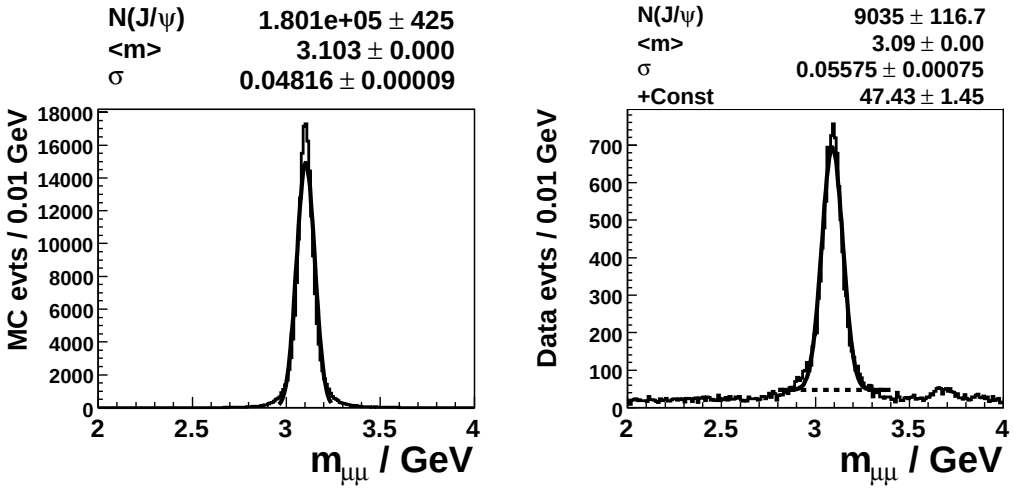

Figure 7.3.: Central invariant mass distribution for data and MC.

The signals from data have been fit with a Gaussian function plus a polynomial of second order to characterize the background. For a given event distribution as a function of the invariant mass m, this gives

$$f(m) = \frac{N(J/\psi)}{\sqrt{2\,\pi}\,\sigma} e^{-\frac{(m-<m>)^2}{2\sigma^2}} \cdot BW + a\,m^2 + b\,m + Const. \tag{7.8}$$

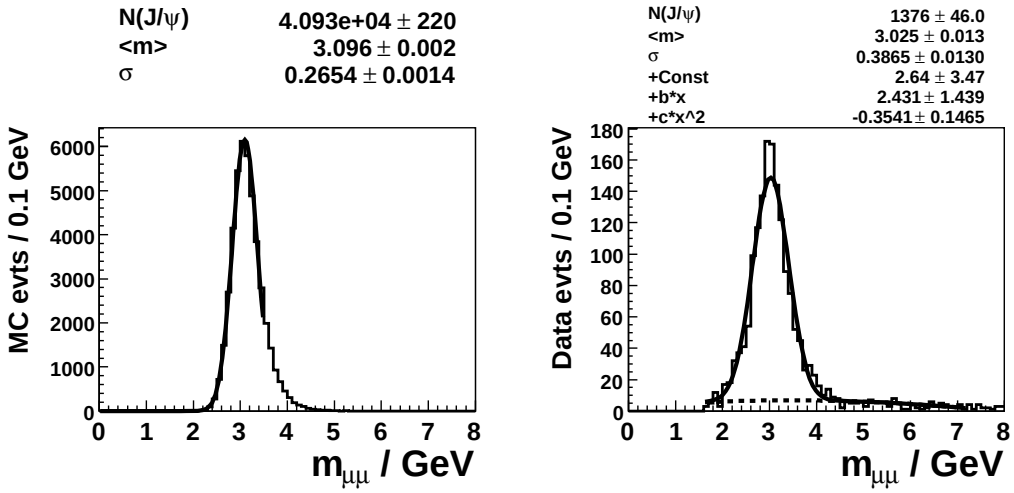

Figure 7.4.: Backward invariant mass distribution for data and MC.

where $N(J/\psi)$ notes the integral content of the fitted Gaussian, BW the bin width, $< m >$ the mean of the Gaussian and σ_m its standard deviation. Due to the asymmetric signal shape, different fitting functions have been proposed in the past, [85, 84], but were not used in this thesis since they resulted from central studies.

The background in forward and backward direction, fig. 7.2 and 7.4, has been fit empirically with polynomials of second order, equ. 7.8. The central signal, fig. 7.3, has been fit with equ. 7.8 where $a = b = 0$ due to lower background contribution. Again, the fit widths demonstrate, that the p_t resolution of the detectors, as in fig. 6.1 to 6.4, contribute more dominantly to the signal than the angular resolution. In addition to the large angular acceptance of the central tracking detectors, this results in a sharp central J/ψ signal with indications of reconstructed $\psi(2S)$ signals at $m_{\mu\,\mu} = 3.686$ GeV decaying as $\psi(2S) \rightarrow \mu^+\mu^-$ ([5]) in the invariant mass distribution. This latter cannot be observed for the forward and backward sample due to a higher signal width.

Further, the fit contents exhibit an increase towards the backward sample, i.e. to higher values of $W_{\gamma p}$. This behavior is confirmed by the MC signals. For fig. 7.2 to 7.5, the mean value of the fitted Gaussian suits the J/psi mass at $m = 3.097$ GeV within the chosen bin widths. Due to the acceptance of the forward trackers, the FMD was also selected for J/ψ reconstruction to give an additional forward sample in competition to the FST.

The higher FMD momentum resolution gives a sharper J/ψ signal. Still, the ratio of fitted signal entries does not match for MC and data. This has to be attributed to unrealistic treatment of the FMD track reconstruction efficiency and unrealistic track loss effects simulation, e.g. multiple scattering, in the MC arguing that the FMD though having a different polar acceptance than the FST allows a track measurement for the full azimuthal range in ϕ_{track}. Still, the FMD used for J/ψ reconstruction exhibits a lower signal number than the FST for the same data sample. The FMD reconstruction mode was discarded from further studies due to the physics motivation to reconstruct J/ψ signals with the FST and BST.

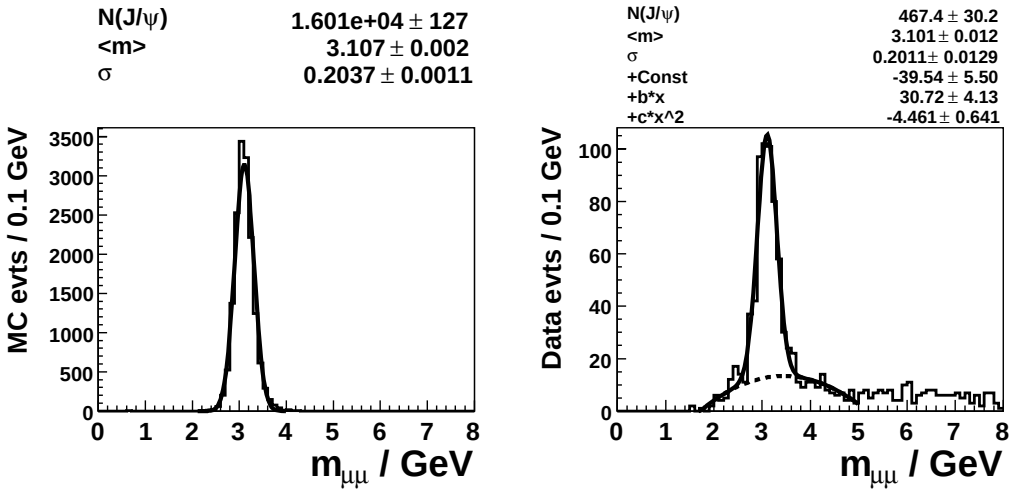

Figure 7.5.: FMD invariant mass distribution for data and MC.

7.2.2. Correction Factors

To correct for $\psi(2S)$ decay background contributions, $f_{\psi(2S),fwd} = (0.032 \pm 0.003)$ and $f_{\psi(2S),bwd} = (0.050 \pm 0.004)$ were extrapolated from results in [19] for the forward and backward analysis respectively.

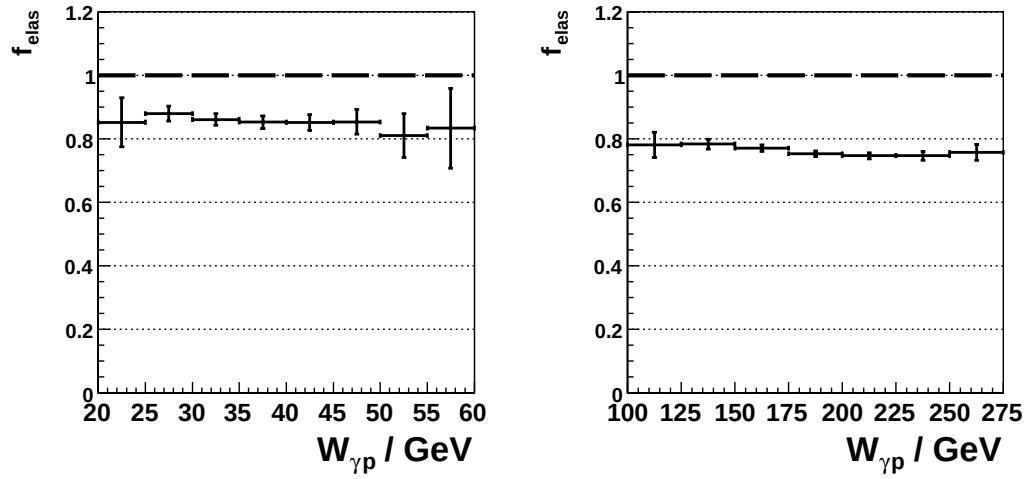

Figure 7.6.: Ratio of elastic signal events in a mixed elastic and proton-dissociative MC f_{elas}.

The ratio of elastic signal events in a sample with proton-dissociative contributions was determined from a MC mixture of elastic and proton-dissociative MC samples simulating the data. Hence, the fraction $f_{elas} = N(elas)/N(elas+pdis)|_{W_{\gamma p}}$ was calculated in each observed $W_{\gamma p}$ interval. Figure 7.6 notes f_{elas} for the complete $W_{\gamma p}$ range in forward and backward direction.

7.3. Statistical and Systematic Uncertainties

The total error of the measured cross section is derived from a quadratic summation of statistical and systematic errors which are summarized in the following. The systematic error of the cross section is derived by quadratically adding the single systematic errors of values entering directly into the calculation as of equ. 7.1. The **statistical error** is obtained from the uncertainties when fitting the signal in kinematic bins of $W_{\gamma p}$, see appendix A.

The **branching ration** for the decay $J/\psi \to \mu^+\mu^-$ is $BR = (0.0593 \pm 0.0006)$ ([5]) giving a relative uncertainty of 1%. The correction factor for **contamination from $\psi(2S)$ decays** is $f_{\psi(2S),fwd} = (0.032 \pm 0.003)$ and $f_{\psi(2S),bwd} = (0.050 \pm 0.004)$ [19] giving a published relative error of 7.7% for both, the forward and backward correction. The calculation of the total integrated luminosity was described in section 5.1. Here, the error on the **luminosity measurement** gave 4% according to [80]. The **correction for proton-dissociative events** contaminating the elastic signal in data with f_{elas} is allocated to an error of 4 - 6 % as documented in [20, 84].

The **trigger efficiencies** have been determined from data due to false simulation of the muonic trigger elements in the MC simulation, as illustrated in section 6.6. The dominating uncertainty within the method used to determine the trigger efficiency from data is hence the fitting error in respective bins of $W_{\gamma p}$. For the forward sample, these relative trigger efficiency errors range from 3 - 16 % in the observed kinematic intervals. For the backward analysis, 4 % are observed.

The **J/ψ reconstruction efficiency** is dominated by the muon identification efficiency and the track reconstruction performance of the detectors used. The MC simulation was changed significantly in this study, starting with deteriorating the FMD in forward direction and changing the BST alignment in backward direction. To characterize the systematic uncertainties, the simulation has been varied in order to simulate the effects of these changes to the reconstruction efficiency. The resulting errors of the reconstruction efficiency $\alpha_{REC} = 5 - 25$ % in forward direction and 15-20 % in backward direction.

All contributions to the systematic and statistical uncertainties of the cross section measurement are summarized in table 7.1.

Sample		Forward			Backward	
min. $W_{\gamma p}$	[GeV]	20	25	30	150	175
max. $W_{\gamma p}$	[GeV]	25	30	35	175	200
$< W_{\gamma p} >$	[GeV]	22.8	27.6	32.5	162.3	187.2
N_{Fit}		31	228	322	472	581
δN		8	17	19	22	25
	[%]	25.8	7.5	5.9	4.7	4.3
$f_{\psi(2S)}$			0.032		0.05	
$\delta f_{\psi(2S)}$			0.003		0.004	
	[%]			7.7		
f_{elas}		0.864	0.872	0.858	0.771	0.754
δf_{elas}		0.051	0.053	0.051	0.046	0.045
	[%]			6		
α_{REC}		0.012	0.092	0.144	0.20	0.294
$\delta\alpha_{REC}$		0.003	0.005	0.010	0.03	0.059
	[%]	25	5.2	4.1	15	20
ϵ_{trig}		0.52	0.58	0.61	0.47	0.38
$\delta\epsilon_{trig}$		0.09	0.09	0.03	0.02	0.02
	[%]	17	15	4.9	4.2	5.2
L	$[nb^{-1}]$		133745		131245	
δL	$[nb^{-1}]$		5350		5250	
	[%]			4		
BR				0.0593		
δBR				0.0006		
	[%]			1		
Φ_γ		0.026	0.020	0.017	0.0092	0.0070
$\delta\Phi_\gamma$		0.001	0.001	0.001	0.0005	0.0004
	[%]			5		
$\delta\sigma(W_{\gamma p})_{stat.}$	[%]	26	7	6	5	4
$\delta\sigma(W_{\gamma p})_{sys.}$	[%]	33	14	14	20	24
$\delta\sigma(W_{\gamma p})_{tot.}$	[%]	42	15	15	20	24

Table 7.1.: Sources for statistical and systematic uncertainties and their effect on the cross section $\sigma(W_{\gamma p})$. The total error of the cross section is calculated from the individual errors by quadratic summation.

7.4. Results

The elastic J/ψ photoproduction cross section $\sigma(W_{\gamma p})$ has been determined as a function of the photon-proton center of mass energy $W_{\gamma p}$. The cross section was measured in three $W_{\gamma p}$ intervals for the forward data sample and in two $W_{\gamma p}$ bins for the backward data set.

Sample		Forward			Backward	
$< W_{\gamma p} >$	[GeV]	22.8	27.6	32.5	162.3	187.2
N_{Fit}		31	228	322	472	581
$f_{\psi(2S)}$			0.032		0.05	
f_{elas}		0.864	0.872	0.858	0.771	0.754
α_{REC}		0.012	0.092	0.144	0.20	0.294
ϵ_{trig}		0.52	0.58	0.61	0.47	0.38
L	$[nb^{-1}]$		133745		131245	
BR			0.0593			
Φ_γ		0.026	0.020	0.017	0.0092	0.0070
$\sigma(W_{\gamma p})$	[nb]	20.8	22.8	23.5	51.4	67.2
$\delta\sigma(W_{\gamma p})_{stat.}$	[nb]	5.6	1.7	1.4	2.4	2.9
$\delta\sigma(W_{\gamma p})_{sys.}$	[nb]	7.3	3.1	3.3	10.0	15.8
$\delta\sigma(W_{\gamma p})_{tot.}$	[nb]	9.2	3.5	3.6	10.3	16.1

Table 7.2.: Input and results of the elastic J/ψ photoproduction cross section $\sigma(W_{\gamma p})$, the statistical $\delta\sigma(W_{\gamma p})_{stat.}$, the systematic $\delta\sigma(W_{\gamma p})_{sys.}$ and the total cross section uncertainty $\delta\sigma(W_{\gamma p})_{tot.}$ are given.

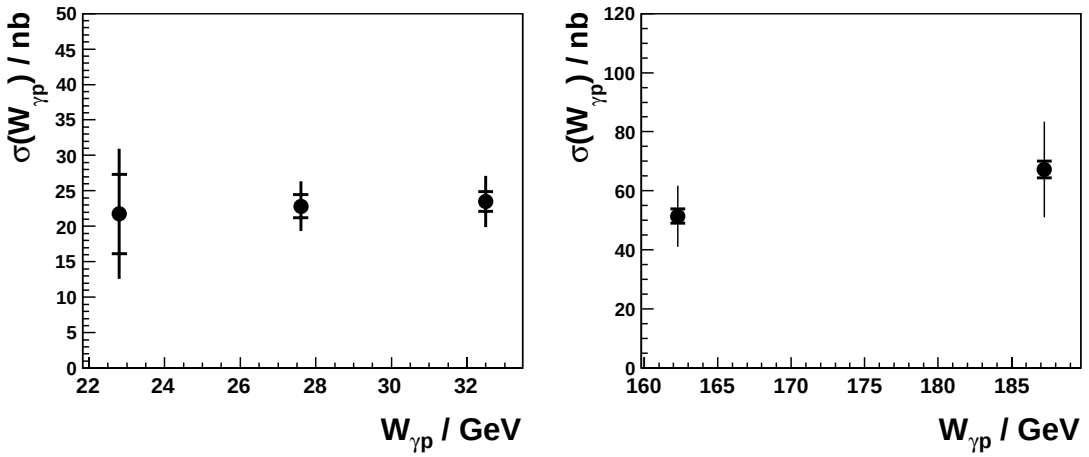

Figure 7.7.: The cross section $\sigma(W_{\gamma p})$ for elastic J/ψ photoproduction as a function of $W_{\gamma p}$ for the forward (left) and the backward data sample (right). The inner error bars correspond to the statistical error and the outer error bars to the total error.

The input for the calculation and the determined statistical as well as systematic uncertainties are listed in table 7.2 as of section 7.3. To retrieve the total uncertainty $\delta\sigma(W_{\gamma p})_{tot.}$ the statistical and systematic errors have been added quadratically. Figure 7.7 shows the

obtained cross section as a function of $W_{\gamma p}$.The inner error bars corresponds to the statistical error and the outer error bars to the total error.

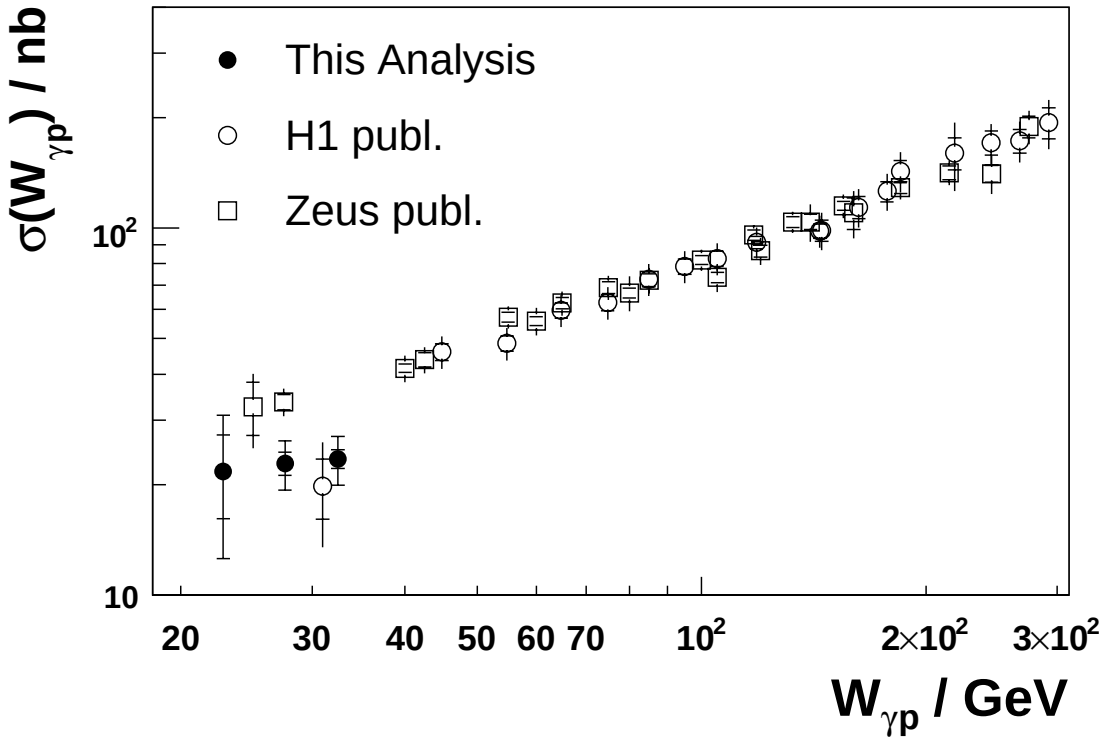

Figure 7.8.: The cross section $\sigma(W_{\gamma p})$ for elastic J/ψ photoproduction as a function of $W_{\gamma p}$. The inner error bars correspond to the statistical error and the outer error bars to the total error. The results of this analysis have been overlaid with the published H1 results [20, 17] and the ZEUS measurements [34].

In fig. 7.8, the results are compared with previously published results of the HERA experiments H1 ([20, 17]) and ZEUS ([34]). The data analyzed by [17] correspond to an integrated luminosity of 20.5 pb^{-1} for a central measurement in H1 and 10.0 pb^{-1} for a high $W_{\gamma p}$ topology of the years 1996 and 1997. Measurements by [20] used an integrated luminosity of 30.26 pb^{-1} for the central study and 26.9 pb^{-1} for the high $W_{\gamma p}$ range from 1999 and 2000. Both analyses combine measurements in the electron decay channel of the J/ψ through $J/\psi \to e^+e^-$ and in the muonic decay $J/\psi \to \mu^+\mu^-$. The results of [20] reach values of $W_{\gamma p} = 305$ since the BST was used as tracker in combination with the SpaCal for electron identification to resolve events where both decay electrons miss the CJC acceptance and can only be detected by SpaCal and BST.

The data used for the published ZEUS results were taken during the years 1999 and 2000 and use an integrated luminosity of 33 pb^{-1} for the muonic decay channel and 55 pb^{-1} for the electron channel.

As in chapter 3 section 3.3.4, a fit of the form $\sigma_{\gamma p} \propto W_{\gamma p}^{\delta}$ was applied to the data. The fit function was motivated by Regge theory.

The fit to the joint cross section results by this analysis in fig. 7.9 yields

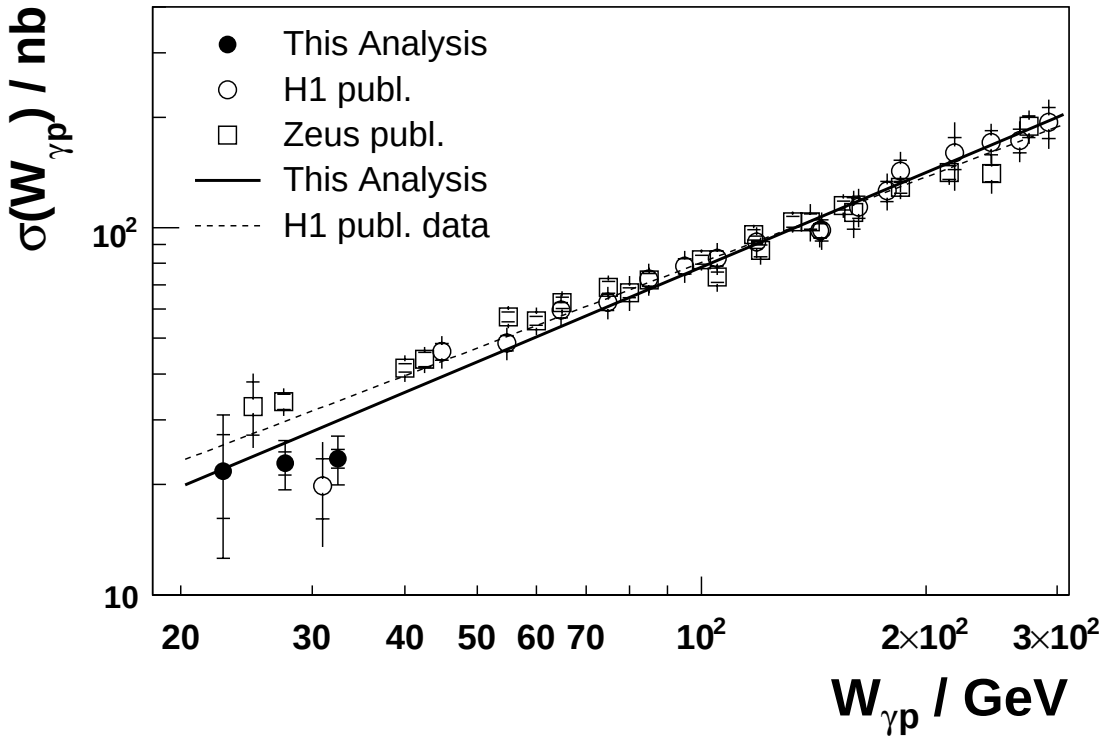

Figure 7.9.: The cross section $\sigma(W_{\gamma p})$ for elastic J/ψ photoproduction as a function of $W_{\gamma p}$. The inner error bars correspond to the statistical error and the outer error bars to the total error. The results of this analysis in forward direction have been joined with published H1 results [20]. A fit of the $\sigma_{\gamma p} \propto W_{\gamma p}^{\delta}$ is applied to the joint data set and to the published data only. The results by the ZEUS experiment ([34]) are depicted for comparison.

$$\delta(25\ \text{GeV} < W_{\gamma p} < 305\ \text{GeV}) = 0.86 \pm 0.02 \pm 0.04 \tag{7.9}$$

where the first error is statistical and the second error is the systematic uncertainty. The statistical error is the fit error, if the fit is applied to the data with statistical errors only. Applying the fit to the data taking the total errors into account yields the total error of δ. The systematic uncertainty results from a quadratic subtraction.

Published measurements by the H1, depicted in fig. 7.9, and ZEUS collaboration in determined δ to be

$$\delta(26\ \text{GeV} < W_{\gamma p} < 305\ \text{GeV}) = 0.76 \pm 0.03 \pm 0.04 \tag{7.10}$$

$$\delta(30\ \text{GeV} < W_{\gamma p} < 290\ \text{GeV}) = 0.69 \pm 0.02 \pm 0.03 \tag{7.11}$$

Again, the first errors correspond to the statistical uncertainty while the second gives the systematic error. In the double logarithmic view, the low forward cross section determined by this analysis pulls the linear fit to the data. Thus, δ is increased. The resulting δ yields a value which corresponds to the published H1 result within errors.

As already pointed out in section 3.3.4, the high value of δ give a higher value than predicted by Regge theory at $\delta \approx 0.22$ for a single Pomeron. In order to describe the steep rise of the cross section, Donnachie and Landshoff introduced the hard Pomeron along the remaining soft Pomeron, see section 3.3.4. The resulting Two Pomeron fit to the data has the form

$$\ln \sigma(W_{\gamma p})/\sigma(W_{\gamma p,0}) = P1 + P2 \cdot \ln W_{\gamma p}/W_{\gamma p,0} + P3 \cdot (\ln W_{\gamma p}/W_{\gamma p,0})^2. \tag{7.12}$$

It was first introduced by [85] and fit to H1 data. The essential parameter of this method is $P3$ describing the curvature in the double-logarithmic plane. In [85], it was measured to $P3 = 0.12 \pm 0.05 \pm 0.08$ when fit to H1 data only and yielding $P3 = 0.01 \pm 0.02 \pm 0.03$ when retrieved from H1 and ZEUS data together. The first given error is statistical and the second systematic. The latter is derived by quadratic subtraction of the parameter from the fit to the data with total errors by the value of the fit to the data statistical errors.

Equation 7.12 was applied to a data set including results of this analysis, ZEUS ([34]) and H1 data ([20]). $P3$ was found to $P3 = -0.08 \pm 0.08 \pm 0.02$ for the fit to published H1 data and this analysis. Adding published ZEUS data to the latter gives $P3 = -0.02 \pm 0.03 \pm 0.02$. The corresponding fits are illustrated in fig. 7.10.

Data Sample	Two Pomeron Fit $P3$	χ^2/n_{df}
H1 only	$0.12 \pm 0.05 \pm 0.08$	
H1 + ZEUS	$0.01 \pm 0.02 \pm 0.03$	
H1 + this analysis	$-0.08 \pm 0.08 \pm 0.02$	8.1/17
H1 + ZEUS + this analysis	$-0.03 \pm 0.03 \pm 0.02$	28.8/39

Table 7.3.: Two Pomeron Fit results for data from H1 ([20]), ZEUS ([34]) and this analysis.

The measured curvature, summarized in table 7.3 with χ^2 test results and the number of degrees of freedom n_{df} of the respective fit, includes negative and positive values within a 1σ range. These fits do not strongly support the Two Pomeron approach describing the data.

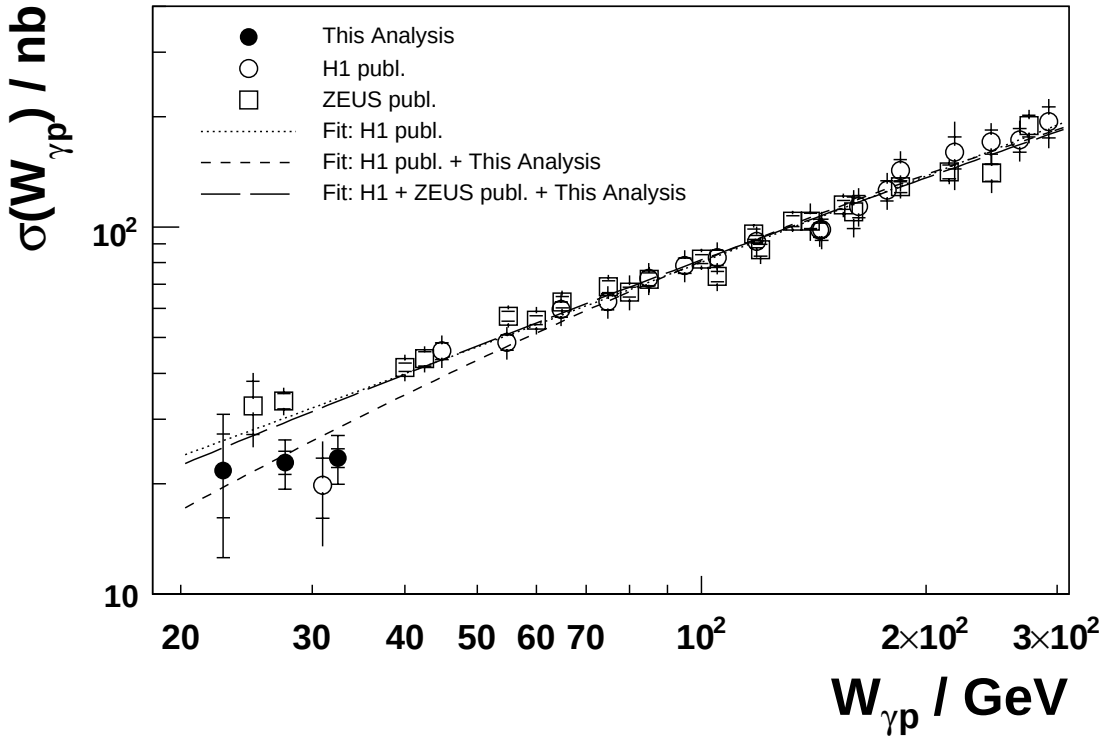

Figure 7.10.: The cross section $\sigma(W_{\gamma p})$ for elastic J/ψ photoproduction as a function of $W_{\gamma p}$. The inner error bars correspond to the statistical error and the outer error bars to the total error. The results of this analysis in forward direction have been joined with published H1 results [20]. A Two Pomeron fit as in [85] with fixed parameter $P3 == -0.07 \pm 0.02 \pm 0.02$ has been applied to the data and is compared to the results from [85].

The cross section $\sigma(W_{\gamma p})$ depends quadratically on the gluon distribution, equ. 3.52. This motivates the present measurement to be a indirect cross check of gluon distribution functions obtained from inclusive DIS analyses. On the other hand, the results of the latter are the input of predictions on the cross section of elastic J/ψ photoproduction processes.

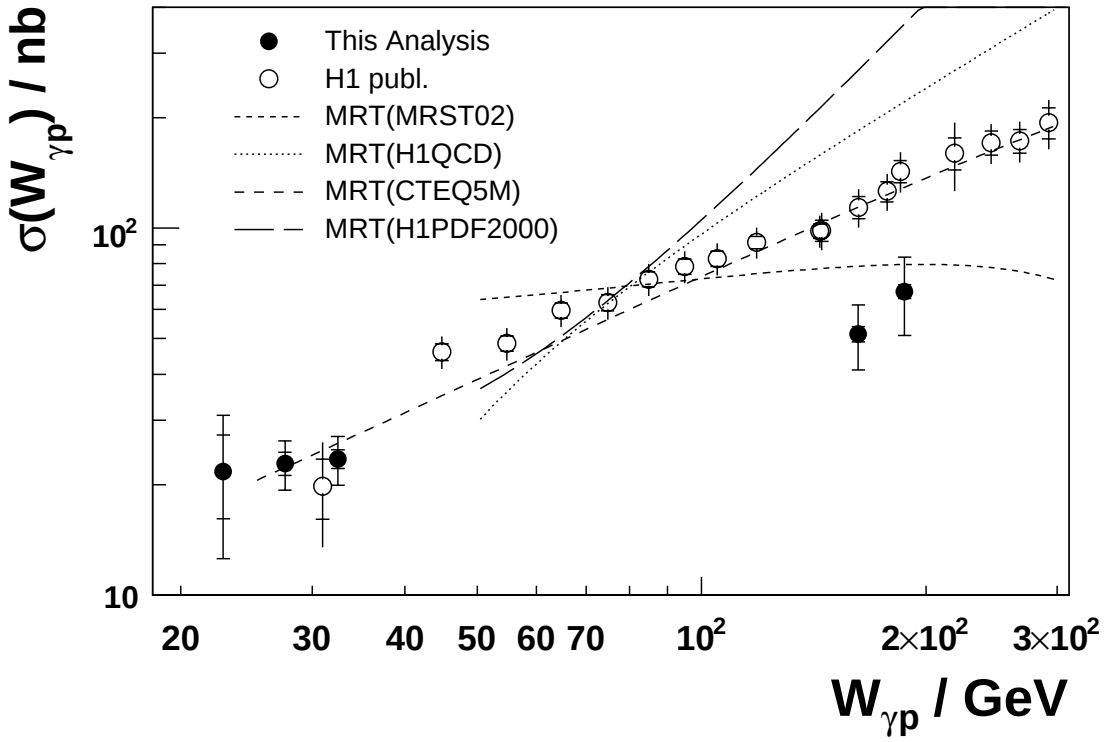

Figure 7.11.: The cross section $\sigma(W_{\gamma p})$ for elastic J/ψ photoproduction as a function of $W_{\gamma p}$ measured by the h1 experiment and in this analysis together with theoretical predictions. The inner error bars correspond to the statistical error and the outer error bars to the total error. The data is compared with a QCD calculations using different parameterizations of the gluon density in the proton. The calculations by Martin, Ryskin and Teubner (MRT, [95]) use gluon distributions from MRST02 [96], H1QCD [97], H1PDF2000 [98] and CTEQ5M [99].

Figure 7.11 illustrates the diverging theoretical predictions towards positive and negative deviations from the data. The reason for this effect is due to high uncertainties upon modeling and measuring the gluon density function $xg(x, Q^2)$. This effect can be observed when comparing the parton distributions used in MRST02[96] and H1PDF2000[98] which mark the extreme outliers of the predictions as illustrated in fig. 7.11.

Figure 7.12 illustrates the large deviations of the theoretical predictions. MRST02 shows a low gluon density for low values of x and Q^2 which tends to unphysical negative values and hence exhibits a very low elastic J/ψ cross section prediction. The gluon density marked H1PDF2000 yields a high value of $xg(x, Q^2)$ in the low x and Q^2 limit giving a high prediction on $\sigma(W_{\gamma p})$.

Recently published Next-to-Next-to-Leading Order (NNLO) QCD calculations by Martin et. al. [100] in fig. 7.13 underline the issue of experimental as well as theoretical uncertainties on the gluon density in the proton.

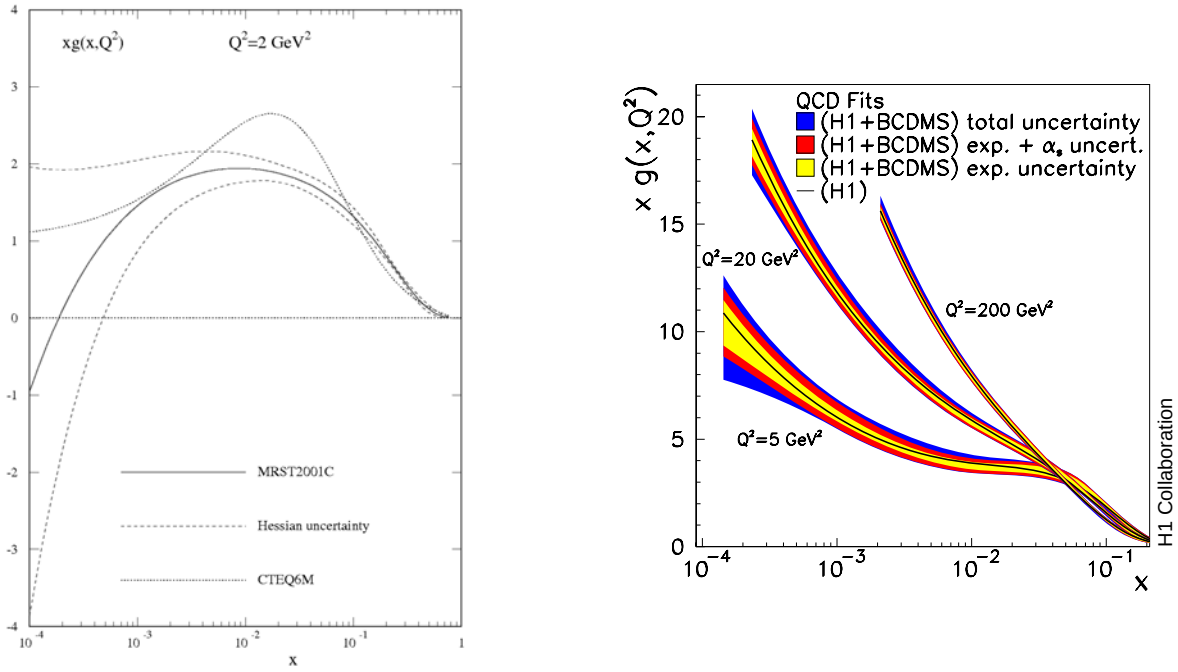

Figure 7.12.: The gluon density functions $xg(x, Q^2)$ used as input for MRT theoretical predictions on the cross section $\sigma(W_{\gamma p})$ for elastic J/ψ photoproduction from MRST02 (left, [96]) and H1PDF2000 (right, [98]).

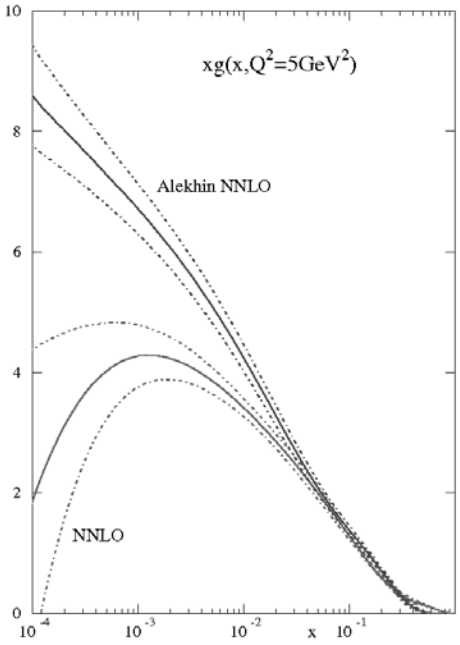

Figure 7.13.: The gluon density functions $xg(x, Q^2)$ predicted by MRST NNLO calculations ([100]) and Alekhin ([101]).

A prediction of $\sigma(W_{\gamma p})$ upon the NNLO or NLO gluon distribution presented in [100] was not available at the time of this study.

The result of the backward analysis in comparison with published data and theoretical predictions is shown in fig. 7.11. The cross section measurement from events with tracks in the BST and CJC deviates by an overall factor of two from published results. The cause of this misbehavior can be attributed to the low understanding of backward trigger efficiencies from *s18* and the effect of background suppressing trigger elements on trigger level one, fig. 6.30, on the measurement of present backward event topologies. In addition, the J/ψ reconstruction efficiency derived from MC studies, fig. 6.23, was found to be overestimated by at least 10 % of the central value ([102, 103]) while studying electrons in DIS. A confirmation of this observation using muons in data was not done at the time of this investigation.

8. Summary

In this thesis, the elastic photoproduction of J/ψ mesons in electron proton collisions recorded by the H1 experiment at the HERA collider was studied for low and high photon-proton center-of-mass energies $W_{\gamma p}$. The J/ψ vector meson was identified through its decay into a $\mu^+\mu^-$ pair. The decay muons enter different regions of the H1 detector depending on $W_{\gamma p}$. In order to extend published elastic J/ψ photoproduction results to low and high values of $W_{\gamma p}$, the Forward and Backward Silicon Tracker were used together with the Central Jet Chambers to reconstruct the decay leptons in the forward and backward regions of the H1 detector.

The forward and backward J/ψ reconstruction corresponds to the kinematic ranges 20 GeV $< W_{\gamma p} <$ 35 GeV and 150 GeV $< W_{\gamma p} <$ 200 GeV, respectively. Both data samples have been collected with the H1 detector at the electron proton collider HERA during the years 2006 and 2007. The data sample of forward events contained an integrated luminosity of 134 pb^{-1} and 131 pb^{-1} for backward events. The data is selected with a transverse J/ψ momentum $|t| < 1.2$ GeV^2.

The measurement demonstrated for the first time that the Forward and Backward Silicon Trackers are able to extend the central track acceptance and widen the kinematical range of the H1 experiment to extract elastic J/ψ photoproduction events.

The main background contributions from proton-dissociative processes and cosmic muons were rejected by correction factors determined from different MC samples and by cuts on the cosmic muon track topology and timing, respectively.

Further, the tracks in forward and central region have been identified as muons by the H1 Forward Muon Detector, the instrumented Iron and the Liquid Argon Calorimeter. In backward direction, the Spaghetti Calorimeter was used for the first time as muon identificator.

After reconstructing the J/ψ signals, the numbers of events were determined within $W_{\gamma p}$ bins selected by MC studies. Taking into account measured MC J/ψ reconstruction efficiencies and trigger efficiencies from data, the cross section of elastic J/ψ photoproduction $\sigma(W_{\gamma p})$ was calculated as a function of $W_{\gamma p}$. The dependence of $\sigma(W_{\gamma p})$ follows a power law $\propto W_{\gamma p}^{\delta}$. When fit to the data provided by recent H1 publications and this analysis, δ yields $0.86 \pm 0.02 \pm 0.04$. This strong rise of the cross section excludes the single soft Pomeron exchange.

Also, a Two Pomeron fit was applied to the data, but the fit results do not strongly support this model.

Finally, predictions from QCD calculations were compared to the cross section $\sigma(W_{\gamma p})$. The $W_{\gamma p}$ dependence of the predictions depend on the square of gluon densities in the proton. This makes the photoproduction cross section an important tool to test gluon densities determined from inclusive measurements. While some of these predictions are consistent with the presented J/ψ measurement, others can be excluded. Thus, the elastic photoproduction of J/ψ vector mesons could be a sensitive tool to access the gluon distribution in the nucleon.

A. Appendix - Mass Distribution Fits

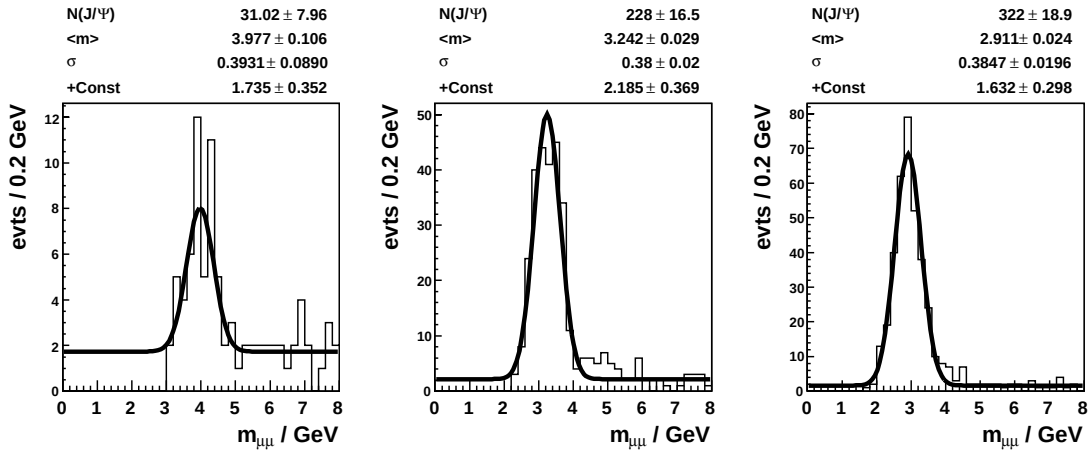

Figure A.1.: Invariant mass distribution for forward kinematic bins $20 < W_{\gamma p} < 25$ GeV (left) and $25 < W_{\gamma p} < 30$ GeV (center) and $30 < W_{\gamma p} < 35$ GeV (right).

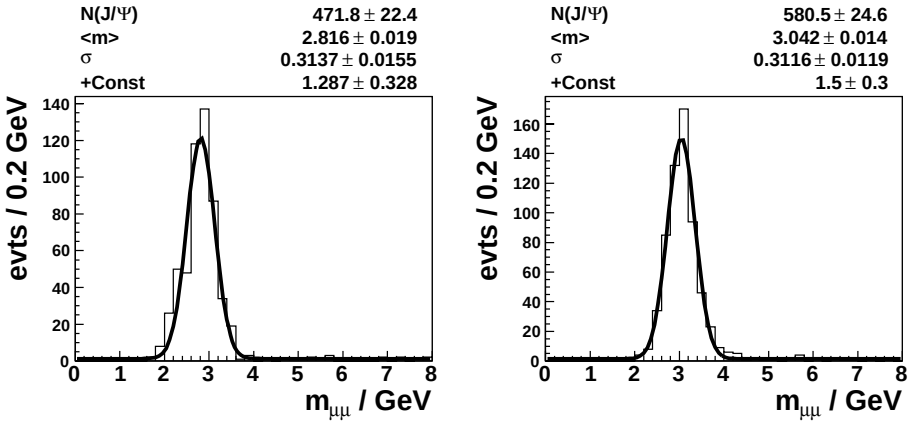

Figure A.2.: Invariant mass distribution for backward $W_{\gamma p}$ bins $150 < W_{\gamma p} < 175$ GeV (left) and $175 < W_{\gamma p} < 200$ GeV (right).

Mass distributions in fig. A.1 and A.2 have been fitted with a Gaussian function plus a constant contribution of background.

$$f(m) = \frac{N(J/\psi)}{\sqrt{2\,\pi}\,\sigma} e^{-\frac{(m-<m>)^2}{2\sigma^2}} \cdot BW + Const. \tag{A.1}$$

Here, $N(J/\psi)$ notes the integral content of the fitted Gaussian, BW the bin width of the x axis, $< m >$ the mean of the Gaussian and σ_m its standard deviation and $Const.$ a constant.

List of Figures

3.1. Feynman diagrams for neutral (γ^*; Z) and charged current ($W^{\pm}$) lepton nucleon scattering. . . . 4
3.2. Diagram of diffractive ep-scattering: elastic scattering (left) and proton dissociative diffraction (right). The production mechanism is illustrated for the Regge ($\mathbb{P}$) and the QCD (g^2) description as a double dashed line producing a vector meson V. . . . 6
3.3. $ab \to cd$ scattering process 8
3.4. $\bar{p}p$ total cross sections as in [6]. . . . 10
3.5. Chew-Frautschi plot: The total angular spin $l = \alpha(t)$ plotted against the particle mass squared $t = m^2$ as in [6]. Each point corresponds to a particle family that interacts when a reggeon trajectory is exchanged. The fit follows $\alpha(t) = 0.44 + 0.93\,t$. . . . 11
3.6. Measurements of the total γp cross section and the cross section for elastic vector meson production as a function of $W_{\gamma p}$ ([16, 17, 18, 19, 20, 21, 22]). . . 16
3.7. Diagram of elastic J/ψ photoproduction in as modeled by Regge theory (left) and by QCD (right). . . . 17

4.1. HERA accelerator and tunnel scheme 21
4.2. The H1 Experiment in 3D View as of 1993. . . . 22
4.3. The H1 Experiment in r-z View as of 2006. . . . 23
4.4. The H1 coordinate system from [53]. . . . 24
4.5. The H1 central tracking detectors in r-ϕ view. . . . 26
4.6. The CJC measuring principle in r-ϕ view. . . . 27
4.7. The LAr system in r-z view. The abbreviations F/C/B stand for the forward, central or backward location of the segment in the detector. E/H denotes the electromagnetic or hadronic component of the calorimeter system. . . . 28
4.8. The LAr system in r-ϕ view. . . . 29
4.9. CMD modules and sectors in r-ϕ view (left) and one barrel segment sliced in r-z view (right) to show the setup of the instrumented 10 layer iron plate structure plus streamer chambers. . . . 30
4.10. The CMD projected into the θ-ϕ plane using an inline Monte Carlo simulation, as in [62] (0-15: forward endcap, 16-47 barrel, 48-63 backward endcap). . . . 31
4.11. FMD in schematic r-z view. The dashed lines correspond to the geometrical equivalent in θ. Below $\theta = 3^\circ$, a scheme of the HERA beam line is drawn. . . 32
4.12. FMD θ (left) and ϕ octants in r-ϕ view. The grey bars indicate drift chambers. The coordinate system depicted is an intrinsic octant one and does not correspond to the general H1 system. . . . 33

4.13. Bethe-Bloch energy loss of protons, pions and muons in various target materials as indicated in the plot, see [5]. 33
4.14. KALEP estimator measurement scheme for the H1 LAr as in [63, 64, 65]. The dashed line corresponds to an extrapolated track helix to the calorimeter. . . 34
4.15. Schematic view of the passage of a particle through a semiconductor detector cell with readout elements. a) DC coupled readout, b) AC coupled readout. . 36
4.16. FST in r-z view. 37
4.17. Left: sensor wheel in r-ϕ view and single sensor segments (right) with strip overlay, [66, 67]. 38
4.18. BST in the r-z view,[66]. 38
4.19. FST and BST in 3D view around the beam pipe, [66]. 39
4.20. The electromagnetic part of the SpaCal (left) and the hadronic one (right) in r-ϕ view. 40
4.21. Overview of the H1 trigger scheme. 41
4.22. Definitions of κ and d_ca. 43

5.1. H1 event display of a forward elastic J/ψ at a low value of $W_{\gamma p}$. The input by FST and the instrumented Iron is important. 46
5.2. H1 event display of a backward elastic J/ψ at a high value of $W_{\gamma p}$. The large polar angle of one track narrow opening angle indicates the importance of the BST track measurement and the SpaCal muon identification, see section 6.4. 46
5.3. Number of MC J/ψ events versus $W_{\gamma p}$ of the forward and backward data sample. The central sample is plotted for comparison. 47
5.4. Reconstruction of the invariant J/ψ mass with both decay muons inside the CJC acceptance. The reduction of background when demanding 0, 1, 2 (from left to right) identified muons is visible. 50
5.5. Invariant mass distribution from forward double muonic decay events with one muon in the FST and one in the CJC acceptance. The reduction of background when demanding 0, 1, 2 (from left to right) identified muons is visible. 50
5.6. Invariant mass distribution from backward double muonic decay events with one muon in the BST and one in the CJC acceptance. From left to right 0, 1, 2 identified muons are required. 50
5.7. Time difference $\Delta t = t_{event} - t_{CJC}$. 51
5.8. Left: Central cosmic ray muons plotted in the ($\Delta\phi$, $\Delta\theta$) plane showing a clear accumulation of cosmic candidates near (180°, 180°) where tracks coming from a common accumulate. Right: The distribution of R in logarithmic scale. The a dashed line marks the $R = 1$ limit. 52
5.9. Diagram of elastic J/ψ photoproduction and involved kinematic variables. . . 53
5.10. SpaCal cluster energy distribution of all events selected by the trigger s18. The dashed line illustrates the event cut $E_{cluster} < 2$ GeV taken to select elastic processes. 54
5.11. $t_{REC} - t_{GEN}$ distributions for the forward sample (left) and the backward one (right). 55
5.12. The distribution of reconstructed J/ψ candidates from the forward sample (left) and the backward sample (right) in DATA (top) and MC (bottom) as a function of t. The dashed line illustrates the cut at $t < 1.2$ GeV^2. 56

6.1. CJC track resolution in MC in p_t, ϕ and θ. 58
6.2. FST track resolution in MC in p_t, ϕ and θ. 58
6.3. BST track resolution in MC in p_t, ϕ and θ. 58
6.4. FMD track reconstruction resolution in MC in p_t, ϕ and θ. 59
6.5. FMD track resolution in MC in p_t, ϕ and θ. 59
6.6. CJC, FST and BST θ track acceptance (left) and reconstruction efficiency (right) in MC. The dashed line indicates the maximum efficiency of 75%. . . 60
6.7. FST and BST θ track acceptance (left) and reconstruction efficiencies (right) in MC. 61
6.8. CJC, FST and BST track p_t distribution for MC and data. For the MC, the proton dissociative background is also shown. 62
6.9. FST(left) and BST(right) track θ control plots. 62
6.10. Muon System track θ control plots. 62
6.11. FST track matching precision with the muon system (FMD,LAr,Iron) in MC in p_t, ϕ and θ. 63
6.12. FST track matching precision with the muon system (FMD,LAr,Iron) in DATA in p_t, ϕ and θ. 63
6.13. FST-Muon System track matching in $\Delta\phi = \phi_{MUSYS} - \phi_{FST}$ versus $\Delta\theta = \theta_{MUSYS} - \theta_{FST}$ scatter plot in data (left) and MC (right). The plot limits represent the chosen matching cut. 64
6.14. Cluster energy (left) and SpaCal-BST radial distance distributions (right) in data and MC of 2006/2007. The difference in R is due to a misalignment of the BST versus the SpaCal in MC, [89] 64
6.15. Track θ acceptance and reconstruction efficiency of all systems used for muon identification (FMD, central muon system, SpaCal). The cracks between the barrel and endcap systems are visible at 30° and 135°. 65
6.16. FMD θ track efficiency for MC (left) and data (right). A polynomial of 4th order was used for fitting: $f(\theta) = p_0 + p_1 \cdot \theta + p_2 \cdot \theta^2 + p_3 \cdot \theta^3 + p_4 \cdot \theta^4$. 66
6.17. Polar angle acceptance of the central muon system tracks used to identify CJC tracks as decay muon tracks in MC (left) and the calculated efficiency of simulated tracks (right). 67
6.18. Acceptance of the forward muon system for tracks used to identify FST tracks in MC (left) and the calculated efficiency from simulated tracks (right) as a function of the polar angle θ. 67
6.19. Efficiency of simulated tracks identified as muons by the eSpaCal in MC. The BST θ track reconstruction efficiency has been overlaid for comparison as a function of the polar angle θ. 67
6.20. Kinematic variable resolutions showing the $x_{REC} - x_{GEN}$ distributions for the kinematic variables $\theta_{J/\psi}, \eta, W_{\gamma p}$ in forward direction. 69
6.21. Kinematic variable resolutions showing the $x_{REC} - x_{GEN}$ distributions for the kinematic variables $\theta_{J/\psi}, \eta, W_{\gamma p}$ in backward direction. 69
6.22. Number of reconstructed J/ψ mesons as a function of the kinematic variables $\theta_{J/\psi}, \eta, W_{\gamma p}$ in forward direction. 70
6.23. Number of reconstructed J/ψ mesons as a function of the kinematic variables $\theta_{J/\psi}, \eta, W_{\gamma p}$ in backward direction. 70
6.24. J/ψ reconstruction efficiency in the three kinematic variables, $\theta_{J/\psi}$, $\eta_{J/\psi}$ and $W_{\gamma p}$ for the forward sample. 71

6.25. J/ψ reconstruction efficiency in the three kinematic variables, $\theta_{J/\psi}$, $\eta_{J/\psi}$ and $W_{\gamma p}$ for the backward sample. 71
6.26. Muon system trigger efficiency in s18, forward (left) and backward (right) . . 73
6.27. CIP trigger efficiency in s18, forward (left) and backward (right). 73
6.28. FTT on L1 and FTT L2 subtrigger 81 efficiency in s18, forward (left) and backward (right). 73
6.29. Background trigger elements efficiency in s18, forward (left) and backward (right). 74
6.30. Total trigger efficiency of s18, forward (left) and backward (right). 74
6.31. Trigger element track reconstruction efficiency, muon barrel (left), endcap (middle) and both for comparison (right). 75

7.1. Photon Flux Φ_γ calculated for the forward (left) and backward sample (right). 78
7.2. Forward invariant mass distribution for data and MC. 79
7.3. Central invariant mass distribution for data and MC. 79
7.4. Backward invariant mass distribution for data and MC. 80
7.5. FMD invariant mass distribution for data and MC. 81
7.6. Ratio of elastic signal events in a mixed elastic and proton-dissociative MC f_{elas}. 81
7.7. The cross section $\sigma(W_{\gamma p})$ for elastic J/ψ photoproduction as a function of $W_{\gamma p}$ for the forward (left) and the backward data sample (right). The inner error bars correspond to the statistical error and the outer error bars to the total error. 84
7.8. The cross section $\sigma(W_{\gamma p})$ for elastic J/ψ photoproduction as a function of $W_{\gamma p}$. The inner error bars correspond to the statistical error and the outer error bars to the total error. The results of this analysis have been overlaid with the published H1 results [20, 17] and the ZEUS measurements [34]. . . . 85
7.9. The cross section $\sigma(W_{\gamma p})$ for elastic J/ψ photoproduction as a function of $W_{\gamma p}$. The inner error bars correspond to the statistical error and the outer error bars to the total error. The results of this analysis in forward direction have been joined with published H1 results [20]. A fit of the $\sigma_{\gamma p} \propto W_{\gamma p}^{\delta}$ is applied to the joint data set and to the published data only. The results by the ZEUS experiment ([34]) are depicted for comparison. 86
7.10. The cross section $\sigma(W_{\gamma p})$ for elastic J/ψ photoproduction as a function of $W_{\gamma p}$. The inner error bars correspond to the statistical error and the outer error bars to the total error. The results of this analysis in forward direction have been joined with published H1 results [20]. A Two Pomeron fit as in [85] with fixed parameter $P3 == -0.07 \pm 0.02 \pm 0.02$ has been applied to the data and is compared to the results from [85]. 88
7.11. The cross section $\sigma(W_{\gamma p})$ for elastic J/ψ photoproduction as a function of $W_{\gamma p}$ measured by the h1 experiment and in this analysis together with theoretical predictions. The inner error bars correspond to the statistical error and the outer error bars to the total error. The data is compared with a QCD calculations using different parameterizations of the gluon density in the proton. The calculations by Martin, Ryskin and Teubner (MRT, [95]) use gluon distributions from MRST02 [96], H1QCD [97], H1PDF2000 [98] and CTEQ5M [99]. 89

7.12. The gluon density functions $xg(x, Q^2)$ used as input for MRT theoretical predictions on the cross section $\sigma(W_{\gamma p})$ for elastic J/ψ photoproduction from MRST02 (left, [96]) and H1PDF2000 (right, [98]). 90
7.13. The gluon density functions $xg(x, Q^2)$ predicted by MRST NNLO calculations ([100]) and Alekhin ([101]). 90

A.1. Invariant mass distribution for forward kinematic bins $20 < W_{\gamma p} < 25$ GeV (left) and $25 < W_{\gamma p} < 30$ GeV (center) and $30 < W_{\gamma p} < 35$ GeV (right). . . . 94
A.2. Invariant mass distribution for backward $W_{\gamma p}$ bins $150 < W_{\gamma p} < 175$ GeV (left) and $175 < W_{\gamma p} < 200$ GeV (right). 94

List of Tables

3.1. Parameters of the J/ψ Vector Meson, as in [5] 7

4.1. Nominal parameters of the HERA facility as listed in [50]. 24
4.2. Key Parameters of the Central Tracking System at H1. 26
4.3. Muon Identification qualities Q_μ at H1. 35

5.1. Summary of integrated luminosities. The errors are dominated by ±4% according to [80]. Given luminosities have been corrected for prescale factors. . 45
5.2. Cuts to reconstruct $J/\psi \to \mu^+\mu^-$ vector mesons. For details on background and lepton identification see sections 5.5 and 5.4. 48
5.3. Muon Matching Grades. 49

6.1. $W_{\gamma p}$ binning, reconstruction efficiency α_{REC} and its error $\delta\alpha_{REC}$. 68

7.1. Sources for statistical and systematic uncertainties and their effect on the cross section $\sigma(W_{\gamma p})$. The total error of the cross section is calculated from the individual errors by quadratic summation. 83
7.2. Input and results of the elastic J/ψ photoproduction cross section $\sigma(W_{\gamma p})$, the statistical $\delta\sigma(W_{\gamma p})_{stat.}$, the systematic $\delta\sigma(W_{\gamma p})_{sys.}$ and the total cross section uncertainty $\delta\sigma(W_{\gamma p})_{tot.}$ are given. 84
7.3. Two Pomeron Fit results for data from H1 ([20]), ZEUS ([34]) and this analysis. 87

Bibliography

[1] F. Halzen and A. D. Martin, *Quarks and Leptons: An Introductory Course in Modern Particle Physics*. John Wiley & Sons, Inc., New York, USA, 1984.

[2] **SLAC-SP-017** Collaboration, J. E. Augustin *et. al.*, *Discovery of a Narrow Resonance in e^+e^- Annihilation*, *Phys. Rev. Lett.* **33** (1974) 1406–1408.

[3] J. J. Aubert *et. al.*, *Discovery of the New Particle J*, *Nucl. Phys.* **B89** (1975) 1.

[4] S. Lundqvist, ed., *Nobel Lectures Physics, 1971 - 1980*. World Scientific Publishing, August, 1992.

[5] W.-M. Yao *et. al.*, *Review of Particle Physics*, *Journal of Physics G* **33** (2006). pdg.lbl.gov.

[6] A. Donnachie, H. G. Dosch, P. V. Landshoff and O. Nachtmann, *Pomeron Physics and QCD*. Cambridge University Press, Cambridge, UK, 1st ed., 2002.

[7] T. Regge, *Bound States, Shadow States and Mandelstam Representation*, *Nuovo Cimento* **18** (1960) 947.

[8] T. Regge, *n. n.*, *Nuovo Cimento* **14** (1959) 951.

[9] T. R. A. Buttino, A.M. Longhoni, *n. n.*, *Nuovo Cimento* **23** (1962) 954.

[10] S. F. G.F. Chew, *Principle of Equivalence for all Strongly Interacting Particles with S-Matrix Framework*, *Phys. Rev. Lett.* (1961), no. 7 394.

[11] A. Donnachie and P. Landshoff, *Total Cross-sections*, *Phys. Lett.* **B296** (1992) 227–232.

[12] A. Donnachie and P. Landshoff, "Soft Interactions." hep-ph/9703366, 1997.

[13] J. Bartels and H. Kowalski, *Diffraction at HERA and the Confinement Problem*, *Eur. Phys. J.* **C19** (2001) 693–708 [hep-ph/0010345].

[14] G. Alberi and G. Goggi, *Diffraction of Subnuclear Waves*, *Phys. Rept.* **74** (1981) 1.

[15] K. Goulianos, *Diffractive Interactions of Hadrons at High Energies*, *Phys. Rept.* **101** (1983) 169.

[16] **H1** Collaboration, C. Adloff *et. al.*, *Diffractive Photoproduction of ψ(2S) Mesons at HERA*, *Phys. Lett.* **B541** (2002) 251. hep-ex/0205107.

[17] **H1** Collaboration, C. Adloff *et. al.*, *Elastic photoproduction of J/ψ and υ Mesons at HERA*, *Phys. Lett.* **B483** (2000) 23–35 [hep-ex/0003020].

[18] **H1** Collaboration, C. Adloff *et. al.*, *Elastic Electroproduction of ρ Mesons at HERA*, *Eur. Phys. J.* **C13** (2000) 371–396 [hep-ex/9902019].

[19] **H1** Collaboration, C. Adloff *et. al.*, *Photo-production of ψ(2S) Mesons at HERA*, *Phys. Lett.* **B421** (1998) 385–394 [hep-ex/9711012].

[20] **H1** Collaboration, A. Aktas *et. al.*, *Elastic J/ψ Production at HERA*, *Eur. Phys. J.* **C46** (2006) 585–603 [hep-ex/0510016].

[21] H. Abramowicz and A. Caldwell, *HERA collider physics*, *Rev. Mod. Phys.* **71** (1999) 1275–1410 [hep-ex/9903037].

[22] **H1** Collaboration, A. Levy, *Measurements of Diffractive Processes at HERA*, hep-ex/0301022.

[23] A. Donnachie and P. Landshoff, *Small x: Two pomerons!*, *Phys. Lett.* **B437** (1998) 408 [hep-ph/9806344].

[24] R. Fiore, L. L. Jenovszky, F. Paccanoni and A. Prokudin, *The Pomeron in Exclusive J/ψ Vector Meson Production*, 2003.

[25] G. A. Schuler and J. Terron, "Elastic and Diffractive Photoproduction of J/ψ Mesons." CERN-TH-6403-92.

[26] P. Newman, *A Study of the Dynamics of Diffractive Photoproduction at HERA*. PhD thesis, University of Birmingham, 1996.

[27] J. C. Collins and A. Freund, *Proof of Factorization for Deeply Virtual Compton Scattering in QCD*, *Phys. Rev.* **D59** (1999) 074009 [hep-ph/9801262].

[28] J. C. Collins, *Factorization in Hard Diffraction*, *J. Phys.* **G28** (2002) 1069–1078 [hep-ph/0107252].

[29] D. Y. Ivanov, G. Krasnikov and L. Szymanowski, *Exclusive Production of Vector Mesons in QCD*, 0900.

[30] F. E. Low, *A Model of the Bare Pomeron*, *Phys. Rev.* **D12** (1975) 163–173.

[31] S. Nussinov, *Colored Quark Version of Some Hadronic Puzzles*, *Phys. Rev. Lett.* **34** (1975) 1286–1289.

[32] M. G. Ryskin, *Diffractive J/ψ Electroproduction in LLA QCD*, *Z. Phys.* **C57** (1993) 89–92.

[33] M. G. Ryskin, R. G. Roberts, A. D. Martin and E. M. Levin, *Diffractive J/ψ Photoproduction as a Probe of the Gluon Density*, *Z. Phys.* **C76** (1997) 231–239 [hep-ph/9511228].

[34] **ZEUS** Collaboration, S. Chekanov *et. al.*, *Exclusive Photoproduction of J/ψ Mesons at HERA*, *Eur. Phys. J.* **C24** (2002) 345–360 [hep-ex/0201043].

[35] A. Hayashigaki and K. Tanaka, *Transverse Quark Motion inside Charmonia in Diffractive Photo- and Electroproductions*, 2004.

[36] A. H. Mueller and B. Patel, *Single and double BFKL Pomeron Exchange and a Dipole Picture of High-Energy Hard Processes*, *Nucl. Phys.* **B425** (1994) 471–488 [hep-ph/9403256].

[37] N. N. Nikolaev and B. G. Zakharov, *The Triple Pomeron Regime and the Structure Function of the Pomeron in the Diffractive Deep Inelastic Scattering at very small x*, *Z. Phys.* **C64** (1994) 631–652 [hep-ph/9306230].

[38] N. Nikolaev and B. G. Zakharov, *Pomeron Structure Function and Diffraction Dissociation of Virtual Photons in Perturbative QCD*, *Z. Phys.* **C53** (1992) 331–346.

[39] M. McDermott, L. Frankfurt, V. Guzey and M. Strikman, *Unitarity and the QCD-improved Dipole Picture*, *Eur. Phys. J.* **C16** (2000) 641–656 [hep-ph/9912547].

[40] L. Frankfurt, M. McDermott and M. Strikman, *A fresh Look at Diffractive J/ψ Photoproduction at HERA, with Predictions for THERA*, *JHEP* **03** (2001) 045 [hep-ph/0009086].

[41] B. List and A. Mastroberardino, *DIFFVM: A Monte Carlo Generator for Diffractive Processes in ep Scattering*, tech. rep., H1 Collaboration, 1999. DESY-PROC-1999-02.

[42] H. Collaboration, *HERA - A Proposal for a Large Electron Proton Colliding Beam Facility at DESY*, . DESY HERA 81-10 (81,REC.AUG.) 292p.

[43] G. A. Voss and B. H. Wiik, *The Electron Proton Collider HERA*, *Ann. Rev. Nucl. Part. Sci.* **44** (1994) 413–452.

[44] F. J. Willeke, *HERA Performance and Prospects*, . Prepared for 12th International Workshop on Deep Inelastic Scattering (DIS 2004), Strbske Pleso, Slovakia, 14-18 Apr 2004.

[45] W. Bartel *et. al.*, *HERA Luminosity Upgrade*, . Prepared for Workshop on Future Physics at HERA (Preceded by meetings 25-26 Sep 1995 and 7-9 Feb 1996 at DESY), Hamburg, Germany, 30-31 May 1996.

[46] **H1** Collaboration, H. Collaboration, *Technical proposal for the H1 detector*, . H1-PROPOSAL.

[47] **ZEUS** Collaboration, G. Wolf *et. al.*, *The zeus detector: Technical proposal*, . DESY-HERA-ZEUS-1.

[48] "Hermes homepage." www-hermes.desy.de.

[49] "Hera-b homepage." www-hera-b.desy.de.

[50] G. H. Hoffstaetter, *Future Possibilities for HERA*, . Prepared for 7th European Particle Accelerator Conference (EPAC 2000), Vienna, Austria, 26-30 Jun 2000.

[51] **H1** Collaboration, I. Abt *et. al.*, *The H1 Detector at HERA*, *Nucl. Instrum. Meth.* **A386** (1997) 310–347. www-h1.desy.de/h1/www/h1det/detpaper/contents.html.

[52] **H1** Collaboration, I. Abt *et. al.*, *The H1 Detector at HERA*, *Nucl. Instrum. Meth.* **A386** (1997) 348–396. www-h1.desy.de/h1/www/h1det/detpaper/contents.html.

[53] T. Kuhr, *Rekonstruktion von V^0s mit dem H1-Silizium-Detektor*, Master's thesis, University of Hamburg, 1998. www-h1.desy.de/psfiles/theses/h1th-134.ps.

[54] J. Burger *et. al.*, *The Central Jet Chamber of the H1 Experiment*, *Nucl. Instrum. Meth.* **A279** (1989) 217–222.

[55] **H1** Collaboration, I. Abt *et. al.*, *The Tracking, Calorimeter and Muon Detectors of the H1 Experiment at HERA*, *Nucl. Instrum. Meth.* **A386** (1997) 348–396.

[56] M. Cuje *et. al.*, *H1 High Luminosity Upgrade 2000 CIP and level 1 vertex trigger*, tech. rep., DESY, 1998.

[57] M. Urban, *The new CIP2k z-Vertex Trigger for the H1 Experiment at HERA*. PhD thesis, University of Zurich, Switzerland, 2004. www-h1.desy.de/psfiles/theses/h1th-366.ps.

[58] D. Pitzl *et. al.*, *The H1 Silicon Vertex Detector*, *Nucl. Instrum. Meth.* **A454** (2000) 334–349 [hep-ex/0002044].

[59] **H1** Collaboration, B. List, *The Silicon Tracker of the H1 Detector*, *Nucl. Instrum. Meth.* **A566** (2006) 110–113.

[60] V. Korbel, *The H1 LAr Calorimeter at HERA, Design, Performance and Status*, *Nucl. Instrum. Meth.* **A327** (1993) 209–211.

[61] **H1** Collaboration, C. Kleinwort and U. Krüger, *Track Reconstruction in the IRON*, tech. rep., 1992. H1 Software Note 35.

[62] H. Wollatz, *Untersuchung von schweren Quarks durch Analyse von Ereignissen mit zwei Myonen am Speicherring HERA*. PhD thesis, University of Hamburg, 1999. www-h1.desy.de/psfiles/theses/h1th-171.ps.

[63] G. Schmidt, *Nachweis von Myonen im H1-Kalorimeter*, Master's thesis, University of Hamburg, 1994.

[64] G. Schmidt, *Untersuchung der diffraktiven Photoproduktion von J/ψ-Mesonen im H1-Detektor bei HERA*. PhD thesis, University of Hamburg, 1997. www-h1.desy.de/psfiles/theses/h1th-077.ps.

[65] S. Schieck, B. Naroska and G. Schmidt, *Lepton Identification in the H1 Detector at low Momenta*, tech. rep., H1 Internal Report, 1997. H1-05 / 97-518.

[66] M. Nozicka, *The Forward and Backward Silicon Trackers of H1*, *Nucl. Instrum. Meth.* **A501** (2003) 54–59.

[67] P. Kostka *et. al.*, *On the Repair of the H1 Forward Silicon Tracker*, tech. rep., H1 Zeuthen, 2004. H1-IN-613(07/2004).

[68] M. Nozicka, *Forward Silicon Tracker of the H1 Experiment: Hardware and Study of D^* Meson Detection*. PhD thesis, Charles University in Prague, 2007.

[69] I. Glushkov, *D^* Meson Production in Deep Inelastic Scattering with the Forward Silicon tracker of the H1 Experiment at HERA*. PhD thesis, Humboldt University Berlin, 2007.

[70] P. Steinbach, "J/ψ Studies with the Forward Silicon Tracker at H1." DESY Summer School Programme 2006, 2006.

[71] **H1** Collaboration, G. Muller, *A Spaghetti calorimeter for the H1-detector*, . Prepared for 5th International Conference on Calorimetry in High-energy Physics, Upton, NY, 25 Sep - 1 Oct 1994.

[72] **H1** Collaboration, J. Hladky, *Spaghetti Calorimeter SPACAL*, . Prepared for International Workshop on Elementary Particle Physics: Present and Future, Valencia, Spain, 5-9 Jun 1995.

[73] C. Arndt, *Kalibration des H1 Spaghetti Kalorimeters mit Halomuonen*, Master's thesis, University of Hamburg, 1996. www-h1.desy.de/psfiles/theses/h1th-031.ps.

[74] C. M. Kiesling *et. al.*, *The H1 Neural Network Trigger Project*, *AIP Conf. Proc.* **583** (2001) 36–44.

[75] D. Hoffman *et. al.*, "The Second Level Topological Trigger of the H1 Experiment at HERA." Submitted to Elsevier Preprints.

[76] D. Hoffman *et. al.*, "L2TT homepage." https://www-h1.desy.de/itrigger/L2Trigger/L2tt/index.html.

[77] **H1** Collaboration, A. Schoning, *The Fast Track Trigger at the H1 Experiment Design Concepts and Algorithms*, *Nucl. Instrum. Meth.* **A566** (2006) 130–132.

[78] V. Andreev *et. al.*, "H1REC Documentation Homepage (2007)." https://www-h1.desy.de/icas/imanuals/h1rec/h1rec9/h1rec.html.

[79] J. Kretzschmar, *BST and FST in H1OO*, tech. rep., H1 Collaboration, 2006. H1 internal document.

[80] D. Pitzl, *The H1 Luminosity Problem 2006/2007*, tech. rep., H1, 2007. H1 internal document.

[81] L. West, *How to Use the Heavy Flavour Working Group Track, Muon and Electron Selection Code*, tech. rep., H1, 1997. H1 internal document.

[82] D. Ozerov *et. al.*, *The H1OO Physics Analysis Project*. The H1oo Group. Internal H1 Analysis Framework Manual.

[83] D. Schmidt, *Diffractive Photoproduction of Charmonium in the H1 Detector at HERA. (In German)*. PhD thesis, University of Hamburg, 2001. DESY-THESIS-2001-029.

[84] P. Fleischmann, *Elastic J/ψ Production at HERA*. PhD thesis, University of Hamburg, 2004. https://www-h1.desy.de/psfiles/theses/h1th-339.ps.

[85] L. Janauschek, *Elastic Photoproduction of J/ψ Vector Mesons at High Photon-Proton Centre-of-Mass Energy at the H1 Experiment at HERA*. PhD thesis, Max-Planck Institute of Munich, 2004. https://www-h1.desy.de/psfiles/theses/h1th-375.ps.

[86] A. Glazov, *Measurement of the Proton Structure Functions $F_2(x, Q^2)$ and $F_L(x, Q^2)$ with H1 Detector at HERA*. PhD thesis, Humboldt University Berlin, 1998. https://www-h1.desy.de/psfiles/theses/h1th-116.ps.

[87] A. Blondel and F. Jaquet, *No title*, in *Proceedings of the Study of an ep Facility for Europe* (U. Amaldi, ed.), p. 391, 1979. DESY 79/48.

[88] S. Schleif, *SpaCal Reconstruction*, tech. rep., H1, 1996. H1 software note 56-03/96.

[89] S. Gorbunov, "BST Misalignment in MC." Private Communication, 2007.

[90] R. Brun *et. al.*, *ROOT - User's Guide 5.14*, December, 2006. root.cern.ch.

[91] J. Wagner, *Charm and beauty production at HERA with D* - muon events*. PhD thesis, University of Hamburg, 2004.

[92] M. Paterno, *Calculating Efficiencies and Their Uncertainties*. home.fnal.gov/ paterno/images/effic.pdf.

[93] A. Rostovtsev and V. Soloshenko, "Corrections to the Weizsäcker-Williams Approximation of Photon Flux in ep Collissions." H1 internal note, August, 1993.

[94] V. M. Budnev, I. F. Ginzburg, G. V. Meledin and V. G. Serbo, *The Two Photon Particle Production Mechanism. Physical Problems. Applications. Equivalent Photon Approximation*, *Phys. Rept.* **15** (1974) 181–281.

[95] A. D. Martin, M. G. Ryskin and T. Teubner, *Q^2 Dependence of Diffractive Vector Meson Electroproduction*, *Phys. Rev.* **D62** (2000) 014022 [hep-ph/9912551].

[96] A. D. Martin, R. G. Roberts, W. J. Stirling and R. S. Thorne, *Uncertainties of Predictions From Parton Distributions. I: Experimental Errors.*, *Eur. Phys. J.* **C28** (2003) 455–473 [hep-ph/0211080].

[97] **H1** Collaboration, C. Adloff *et. al.*, *Measurement and QCD Analysis of Neutral and Charged Current Cross Sections at HERA*, *Eur. Phys. J.* **C30** (2003) 1–32 [hep-ex/0304003].

[98] **H1** Collaboration, C. Adloff *et. al.*, *Deep-inelastic Inclusive ep Scattering at Low x and a Determination of α_s*, *Eur. Phys. J.* **C21** (2001) 33–61 [hep-ex/0012053].

[99] **CTEQ** Collaboration, H. L. Lai *et. al.*, *Global QCD Analysis of Parton Structure of the Nucleon: CTEQ5 Parton Distributions*, *Eur. Phys. J.* **C12** (2000) 375–392 [hep-ph/9903282].

[100] A. D. Martin, W. J. Stirling, R. S. Thorne and G. Watt, *Update of Parton Distributions at NNLO*, *Phys. Lett.* **B652** (2007) 292–299 [arXiv:0706.0459 [hep-ph]].

[101] S. Alekhin, *Parton Distributions from Deep-inelastic Scattering Data*, *Phys. Rev.* **D68** (2003) 014002 [hep-ph/0211096].

[102] C. Diez-Pardos, *Studies of the Direct Measurement of the Protonlongitudinal Structure Function f_l with the H1 detector at HERA*, Master's thesis, Humboldt University Berlin, 2007.

[103] **H1** Collaboration, C. Diez-Pardos, *MC and BST efficiencies*, tech. rep., April, 2007. H1 internal document.

Acknowledgements

First and foremost, my appreciation goes to the University of Leipzig and Prof. Tilman Butz as well as the H1 Collaboration at DESY for their administrative and scientific support to make this analysis possible and to carry it out until the final result of a cross section. Further, my deepest gratitude goes to Prof. Thomas Naumann for his sheer unbreakable confidence in my work, for his scientific advice and for his patience with my mostly uncoordinated willingness to investigate. I would also like to thank Dr. Peter Kostka as head of the H1 Group at DESY in Zeuthen for his help and contributions to make my work possible and public in the H1 community. Then, I would like to express my big appreciation for the friendship and cooperation of many of my colleagues, i.e. Ivan Glushkov, Jan Kretzschmar, Michael Steder, Carmen Diez and many others affiliated with H1 Zeuthen. Finally, my friends and family receive my love and warm appreciation for their support and motivation along this thesis blindly upon the topic and its outcome. Last, I express my everlasting love and gratitude towards my wife Katherina for not only sustaining my absence physically and mentally when this investigation reached its crucial moments over and over again. I hope to be able to repay all of the just noted individuals some day with the same favors as they allowed me to ask of them.

Statement of authorship

I hereby certify that this diploma thesis has been composed by myself, and describes my own work, unless otherwise acknowledged in the text. All references and verbatim extracts have been quoted, and all sources of information have been specifically acknowledged. It has not been accepted in any previous application for a degree.

_____
Peter Steinbach

After positive appraisal of this thesis, I agree that one copy of my presented thesis may remain at the disposal of the library of Leipzig University.

_____
Peter Steinbach

Selbständigkeitserklärung

Hiermit erkläre ich, dass ich die Diplomarbeit selbständig verfasst habe und keine anderen als die angegebenen Quellen und Hilfsmittel benutzt habe. Alle Stellen der Arbeit, die wörtlich oder sinngemäß aus Veröffentlichungen oder aus anderweitigen fremden Äußerungen entnommen wurden, sind als solche kenntlich gemacht. Ferner erkläre ich, dass die Arbeit noch nicht in einem anderen Studiengang als Prüfungsleistung verwendet wurde.

_____
Peter Steinbach

Ich bin einverstanden, dass die Arbeit nach positiver Begutachtung in der Universitätsbibliothek zur Verfügung steht.

_____
Peter Steinbach